On the characterization of solar cells using advanced imaging techniques

Ross Michael Dix-Peek

Submitted in fulfilment of the requirements for the degree of

Magister Scientiae

In the Faculty of Science at the Nelson Mandela University

April 2018

Supervisor: Prof E.E. van Dyk

Co-Supervisor: Dr F.J. Vorster

Co-Supervisor: Mr C.J. Pretorius

Declaration

Full Names: Ross Michael Dix-Peek

Student Number: 212286552

Qualification: Magister Scientiae

Title of Project: On the characterization of solar cells using advanced imaging techniques.

Declaration:

In accordance with Rule G5.6.3, I hereby declare that the above-mentioned treatise / dissertation / thesis is my own work and that it has not previously been submitted for assessment to another University or for another qualification.

Ross Michael Dix-Peek

Dated: February 2018

This is dedicated to the giants whose shoulders we stand upon and those that will stand on ours

Acknowledgements

My sincere gratitude to:

- My supervisor, **Prof E.E. van Dyk**, for his guidance support and encouragement throughout this project
- My co-supervisor, **Dr F.J. Vorster**, for his assistance and support.
- My co-supervisor, **Mr C.J. Pretorius**, for his assistance and support.
- **Carmen Stindt** for her love, support, keeping me fed and sane during this project.
- **Ross Schultz** for his advice and assistance throughout this project
- **The Andre's** for their many discussions and their technical support.
- My colleagues and friends at the university for their input and support.
- My close friends and family for their support.
- **Mr Johan Wessels** for his technical assistance.
- **Ms Chanie Neveling** and **Miss Mariska Müller** for their administrative help.
- **Ms Jualine Ferreira**
- **Centre for Renewable and Sustainable Energy Studies (CRSES)** for their financial support.
- **PVinsight** for their financial support
- **Nelson Mandela University** for their financial support.

The financial assistance of the **National Research Foundation (NRF)** towards this research is hereby acknowledged. Opinions expressed, and conclusions arrived at, are those of the author and are not necessarily to be attributed to the NRF.

Abstract

Photovoltaic (PV) cells are devices capable of producing electricity - in particular, from the abundant resource of sunlight. Solar energy (from PV cells) provides a sustainable alternative to fossil fuel energy sources such as coal and oil. PV cells are typically strung in series in PV modules to generate the current and voltage required for commercial use. However, PV cell performance can be limited by defects and degradation. Under operational conditions due to mismatch and shading, individual cells within a PV module can be forced to operate in their reverse bias regime. Depending on the severity of the reverse bias and the defects present in the cell, the longevity of the cell and/or the module can be affected. Reverse bias (assuming bypass diodes are absent) can result in localised heating that can affect the encapsulant polymer's longevity as well as degrade the cell's performance over time. However, under more severe reverse bias, the cell could fail, drastically affecting the performance of the module.

PV cells can be characterised using various opto-electronic non-destructive techniques, this provides a set of powerful tools which allow the application of multiple such techniques to the same sample. Furthermore, this allows for an in-depth study of the device. Dark Current-Voltage (I-V) measurements, Electroluminescence (EL), Infrared (IR) thermography, Light Beam Induced Current (LBIC) measurements, and the associated techniques are all examples of such tools and are used within this study.

An experimental setup was developed to perform dark I-V measurements, EL imaging, IR thermography and LBIC measurements. Part of the development of the experimental setup was the design of an enclosure in which to perform all the measurements. The enclosure minimised internal reflection, and isolated the experiment from electromagnetic radiation.

Due to the complex mathematical model applied to the I-V curve, an Evolutionary Algorithm was used to determine optimal parameter values for the equation. More specifically, a Genetic Algorithm was used in the Parameter Optimisation (or Extraction) of the dark I-V parameters based upon the two-diode model for PV cells. The resulting parameters give an indication of the material and device quality. However, to determine the spatial distribution of the defects that effect the I-V response of the device, various imaging techniques were utilised.

LBIC is a technique that uses a focussed light beam to raster scan across the surface of a PV cell. The local photo-induced current/voltage can then be measured and compiled into a response map. LBIC was used to determine the local current response across the device.

The intensity distribution of EL signal is related to the local junction voltage and the local quantum efficiency. EL intensity imaging with a Si CCD camera was used to determine the spatial distribution of features visible both in the forward bias and in the reverse bias. The experimental setup utilised had a micron scale resolution. A voltage dependent approach was utilised to further characterise features observed. In forward bias, the local junction varies across the device due to parasitic resistances such as series and shunt resistance. At higher forward bias conditions (in the vicinity of and higher than maximum power voltage), series resistance becomes a limiting factor. Therefore, utilising a voltage dependent approach allows for the determination of a series resistance map from voltage dependent EL images. In reverse bias, localised radiative processes can be imaged. These radiative processes are related to defects in the device, such as Al stains, $FeSi_2$ needles and avalanche breakdown. The processes are related to highly localised current flow; this causes localised heating which degrades the device. The voltage dependent Reverse Bias EL (ReBEL) imaging was also used to determine the local breakdown voltage of radiative reverse features.

Dark IR thermography is a technique used in the identification of high current sites that leads to localised Joule heating, particularly in reverse bias. In this study, thermography was used to identify breakdown sites and shunts.

The results of this study allow for an in-depth analysis of defects found in multi-crystalline Si PV cells using the opto-electronic techniques mentioned above. The multi-pronged approach allowed from a comparison of the various opto-electronic techniques, as well as a more in-depth characterisation of the defects than if only one technique was used.

Keywords: Photovoltaic, LBIC, electroluminescence, IR thermography, parameter optimisation/extraction, junction breakdown

Table of Contents

List of Acronyms

PV	:	Photovoltaic
m-c	:	Multi-crystalline
Si	:	Silicon
I-V	:	Current-Voltage
EL	:	Electroluminescence
VDEL	:	Voltage Dependent Electroluminescence
ReBEL	:	Reverse Bias Electroluminescence
LBIC	:	Light Beam Induced Current
IR	:	Infrared
GA	:	Genetic Algorithm
GAPO	:	Genetic Algorithm for Parameter Optimisation
IFE	:	Internal Field Emission
AB	:	Avalanche Breakdown
I_{SC}	:	Short circuit current
V_{OC}	:	Open circuit voltage

List of Tables

List of Figures

1. Introduction

1.1. Photovoltaic device history

Photovoltaic (PV) cells are devices capable of producing electricity from light – in particular, from the abundant resource of sunlight. In 1839, Becquerel observed, for the first time, the photovoltaic effect. He observed a light-dependant voltage that was measured from an electrolyte solution [1]. This concept was further developed into a solid-state device by Adams and Day in 1877 in *The Action of Light on Selenium* [2]. Fritts, in 1883, demonstrated the first thin-film selenium photocell [1]. The first p-n junction solar cell was demonstrated by Chapin et al in 1954 [1].

1.2. Photovoltaic system usage

Figure 1-1 shows the Direct Normal Irradiation of the world. It is apparent that South Africa is a country in which an above average solar resource is present [3] and it is therefore sensible to utilise this energy source. Solar irradiance is relatively easy to predict and forecast; therefore, the power generation by specific systems can be predicted and forecasted with adequate accuracy. PV power has already been used very effectively in rural areas as part of off-grid systems, and urban areas as part of grid-assisted systems. Large-scale PV plants are already present in South Africa, with a total installed capacity of 1.47 GW [4]. The large areas of well suited, uninhabited land such as areas within the Northern Cape allow for further expansion of the installed capacity of PV plants.

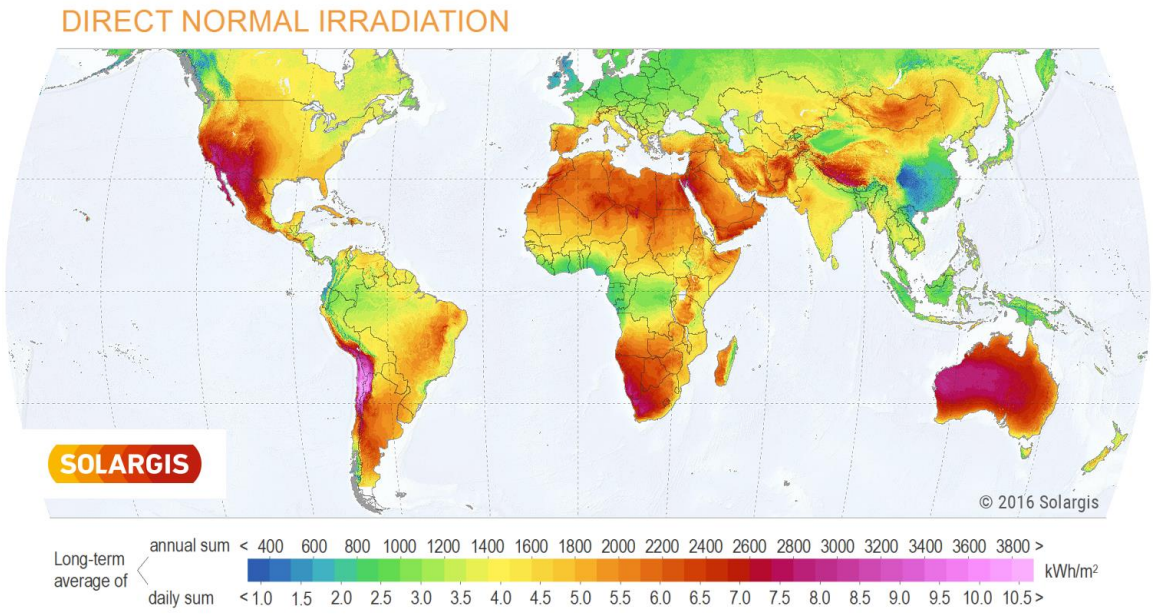

Figure 1-1: Direct Normal Irradiation across the world [3].

Figure 1-2 highlights the exponential growth in cumulative PV installations in selected countries according to the International Energy Agency (IEA) Photovoltaic Power Systems Programme (PVPS) between 2000 and 2015 [5]. This highlights the need for, and the importance of the characterisation of defects associated with cells and the relation of these defects to PV device performance and longevity.

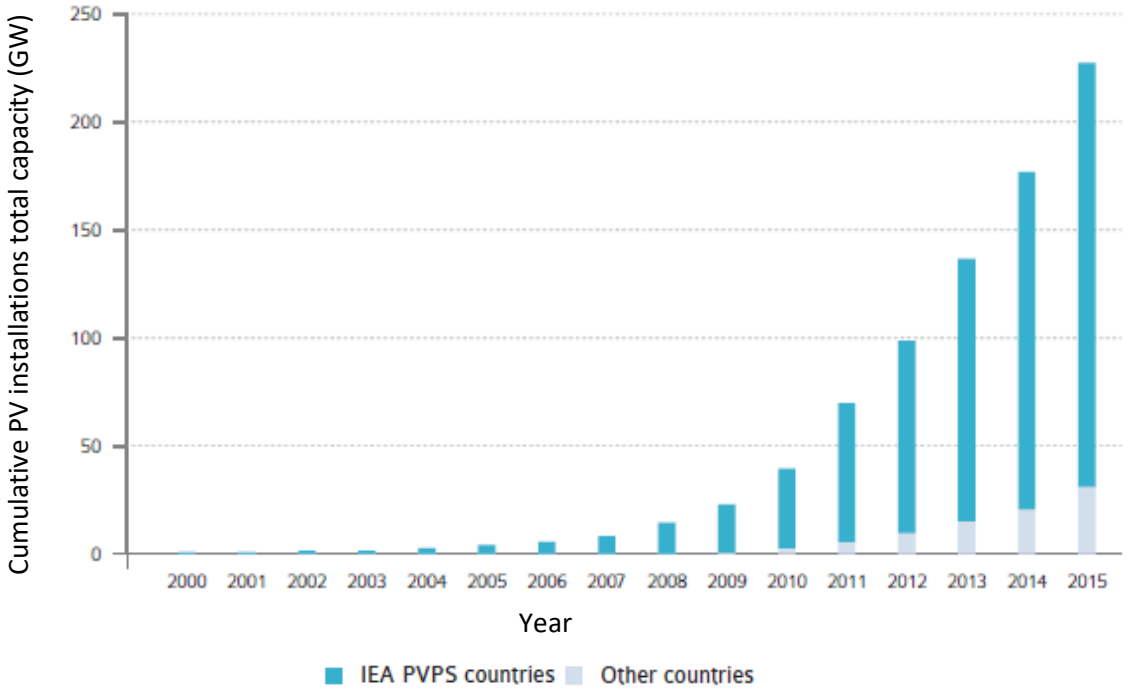

Figure 1-2: Cumulative PV installations in terms of total capacity [5].

Figure 1-3 shows the trend observed in PV module and small-scale PV system cost (in USD) per Watt in selected countries with respect to both high and low range from 2006 to 2015. The cost for both PV systems and modules per Watt appear to be in a decreasing trend. The price for modules has dropped almost linearly from 2006, being between 3.5 USD/W and 4.0 USD/W, to 2015, being between 0.5 USD/W and 1.25 USD/W. The price for complete systems has dropped from 2006, being between 5.5 USD/W and 6.5 USD/W, to 2015, being between 1.5 USD/W and 3.0 USD/W. According to the International Renewable Energy Agency (IRENA), *Solar PV in Africa: Costs and Markets* [5], the lowest local prices (in South Africa) at the moment of the publishing of that article was 1.4 USD/W. Current cost of PV modules (October 2017) in South Africa is on average 0.77 USD/W with a minimum of 0.58 USD/W and a maximum of 1.21 USD/W [7].

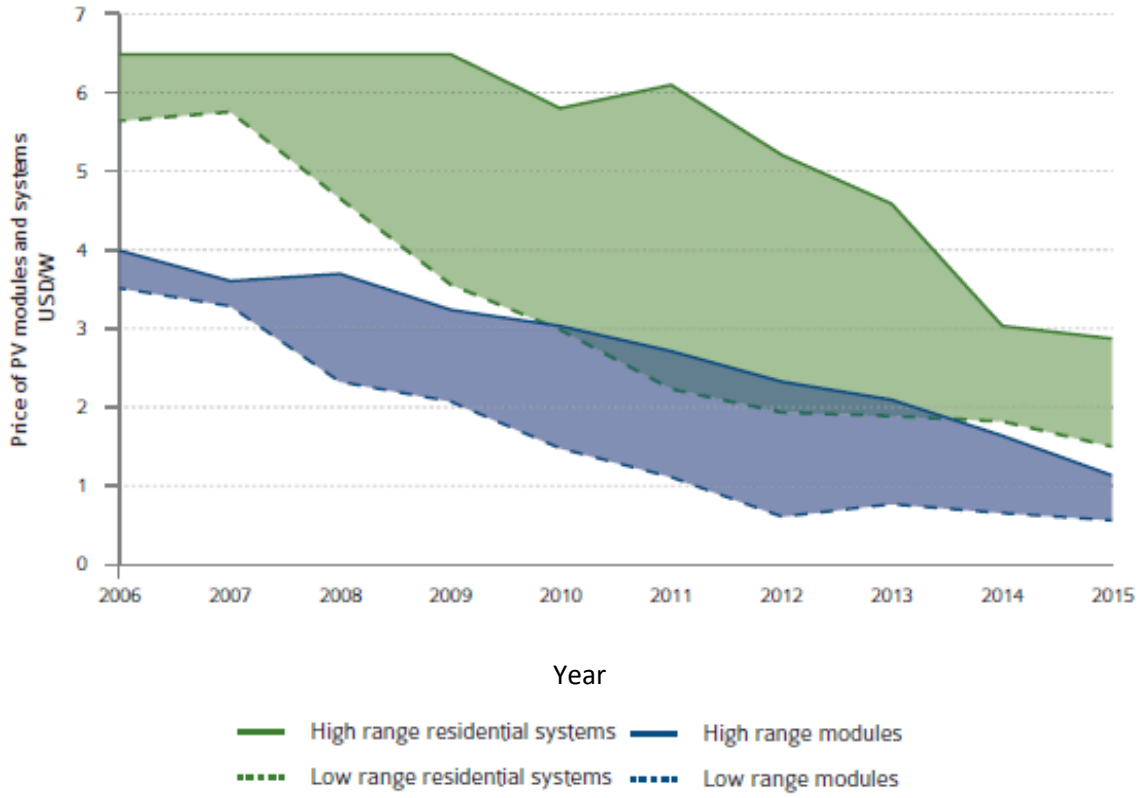

Figure 1-3: Trend of PV modules and small-scale systems price in selected countries from 2006 to 2015 in terms of USD per Watt [5].

1.3. PV device characterisation

Non-destructive characterisation techniques provide a set of powerful tools which allow the application of multiple such techniques to the same sample. Furthermore, this allows for an in depth understanding of the device being studied. Electroluminescence (EL), Infrared (IR) thermography, Light Beam Induced Current (LBIC) measurements, and the associated techniques are all examples of such tools and will be employed in this study.

EL is the reverse of the photovoltaic effect; a PV device, under forward bias, luminesces in the active areas of the device [8]. This allows for feature observation, with different features reacting differently to varying bias levels. The EL emitted under reverse bias is related to various breakdown mechanisms [9]. Dark IR thermography (electrically stimulated) is used in the identification and electrical characterisation of alternative current paths (shunt paths) [10], and that of breakdown sites [11] in multi-crystalline (m-c) Si PV cells. The LBIC measurement technique is used to perform localised cell characterization of PV cells using a focussed light beam as a probe. The technique allows for the determination of local photo-induced potential, photo-induced current and current-voltage (I-V) characteristics of a cell, the extraction of device parameters and identification of features present in a PV cell [12].

These non-destructive characterisation tools with the associated techniques, when used in isolation, often provide limited information about the defects present in the PV device. However, the comparison of the results obtained through the combination of the techniques improves the characterisation of identified defects.

1.4. Objectives of dissertation

The following objectives will be completed as part of this study:

- The first objective of this study was to design and construct a system that could be used for the advanced characterisation and identification of defects and their location within photovoltaic (PV) cells. This system was designed to include LBIC measurements, voltage dependent EL intensity imaging and voltage dependent IR thermography.

- The second objective of this study was the implementation of these techniques to identify and characterise performance, and/or device longevity limiting defects.

- The third objective of this study was the development and application of a Genetic Algorithm for Parameter Optimisation (GAPO) on modelling of the dark I-V data of multi-crystalline Si solar cells that was scripted in MATLAB.

1.5. Outline of Dissertation

Chapter 2 is an introduction to the main concepts needed in the understanding of the results obtained within this study. It introduces basic semiconductor theory and the formation of the p-n junction. It also discusses the mathematical models applied to the PV cells and how these models are used in the application of the techniques used in this study.

Chapter 3 contains the overall design of the characterisation system and its construction. This chapter also contains the procedures used within each subsystem. The purpose of each component and step of the procedures is also discussed.

Chapter 4 discusses the results presented in this study. The chapter is broken up into sections for the different PV cells under test. Each section contains the results from the full battery of techniques used. The identified defects are then characterised according to their properties.

Chapter 5 is the overall conclusion of the study, discussing the successes, and possible improvements of the study. The outlook of the study and the future work related to the study are also outlined.

2. Theory

2.1. Photovoltaic Device

2.1.1. Introduction

PV devices are fabricated from semiconductor materials that convert the energy from absorbed incident light into an electrical current through the photovoltaic effect. The physics associated with PV cells will be discussed within this section, and the models applied to the concept of the PV cell. The defects associated with the material of the PV cell will also be discussed.

2.1.2. Semiconductors

2.1.2.1. Properties

Electrons of an atom are arranged into specific discrete energy levels [13]. Upon formation of a crystal lattice, the energy states of the electrons form into specific energy bands. The region between the two bands hold forbidden energy states, also known as the band gap (E_g) [13]. Semiconductors such as Si have a low band gap (Si at 300K in particular: 1.12eV); therefore, at operational conditions thermal vibrations have enough energy to allow for electrons within the valence band to be excited into the conduction band [13]. Excitation of an electron in the valence band to the conduction band generates an electron-hole pair.

Intrinsic semiconductors are semiconductors with a small number of impurities relative to the number of thermally excited electrons and holes [13]. The lowest energy state of the conduction band is defined to be E_c while the highest energy state of the valence band is defined to be E_v. At room temperature, the Fermi level of an intrinsic semiconductor is approximately in the middle of the bandgap.

Extrinsic semiconductors are doped with specific impurities so as to give the material specific electrical characteristics. Standard Si PV cells' n-type region is formed using phosphor as a donor; while the p-type region is formed using boron as an acceptor.

Boron and phosphor have low ionization energies. That implies that they act as shallow acceptors and donors respectively. For shallow donors and acceptors, such as these, at 300K most if not all impurity atoms will ionize [13]. At a condition called complete ionization, for both donors and acceptors, the concentration of "donated" electrons to the conduction band is equal to the concentration of donor impurities and the number of holes in the valence band is equal to the concentration of acceptor impurities.

An in-depth discussion on the theory of the semiconductor physics of solar cells is described by Sze in the book "Physics of Semiconductor Devices" [13]. The main areas of interest include: semiconductor materials, crystal structure, density of states, carrier concentration profiles, and dopants.

2.1.2.2. Charge carrier transport

Under equilibrium conditions, the motion of an individual electron may be visualized as consecutive random scattering events from collisions with lattice atoms, impurity atoms and other scattering centres [1]. The average time between collisions is called the mean free time. The two main carrier transport mechanisms that cause the movement of charge carriers in semiconducting materials is carrier drift and carrier diffusion.

Carrier drift occurs when carriers move under the influence of an electric field [13]. However, collisions with the atoms within the semiconductor material results in scattering events which limits the drift velocity. The mobility of charge carriers is related to the magnitude of the electric field applied, the level of extrinsic doping in the material, the quality of the semiconductor material and the temperature of the material [13].

Diffusion current occurs as a result of a difference in concentration of charge carriers between two regions. Diffusion current is a net movement of carriers due to the random carrier motion which drives the system to an equilibrium state [13].

2.1.2.3. Photon Absorption

The two primary photon absorption mechanisms that occur in semiconducting materials are fundamental absorption and free carrier absorption [14]. Fundamental absorption occurs due to the absorption of an incident photon that has energy equal to or greater than the band gap of the material generating an electron-hole pair; the energy greater than the band gap is lost thermally. Free carrier absorption occurs due to the absorption of the photon energy by a free carrier, increasing the carrier's kinetic energy, resulting in no further energy band transitions. The energy of a given photon (E_{ph}) is given by [13]:

$$\mathrm{E_{ph}} = \mathrm{hf} = \frac{\mathrm{h}}{\lambda} \text{ ----------} (2\text{-}1)$$

where h is Planck's constant, f is the frequency of the photon and λ is the wavelength of the photon.

Energy and momentum must be conserved in absorption processes. Photons are particles with both momentum and energy. Figure 2-1 (a) shows the process of direct band transitions. That is, for direct photon absorption the electron is excited to the conduction band. Figure 2-1 (b) shows the

process of indirect band transitions. In indirect transitions, the conservation of energy and momentum in the process of exciting an electron can only be achieved in conjunction with phonon absorption or generation [15]. However, the phonon also contributes energy to the transition; therefore, the energy will be less than that of the band gap. The energy contributed is typically in the hundredths of an electron volt and therefore in most cases is negligible [14]. To maintain the conservation of momentum (k) in indirect transitions, in transitions from E_v maximum to E_c minimum, the phonon contributes its momentum ($\bar{q}$) to the transition. In indirect photon absorption, the incident light is absorbed by the electron; however, the phonon must contribute its momentum to excite the electron to the conduction band. Assuming the transition is from the E_v maximum to some point within the conduction band above the E_c minimum, the energy of the incident photon needs to be at least equivalent to the energy difference between the two states. The electron in the higher energy state will then thermalize down to the lowest available energy state in the conduction band.

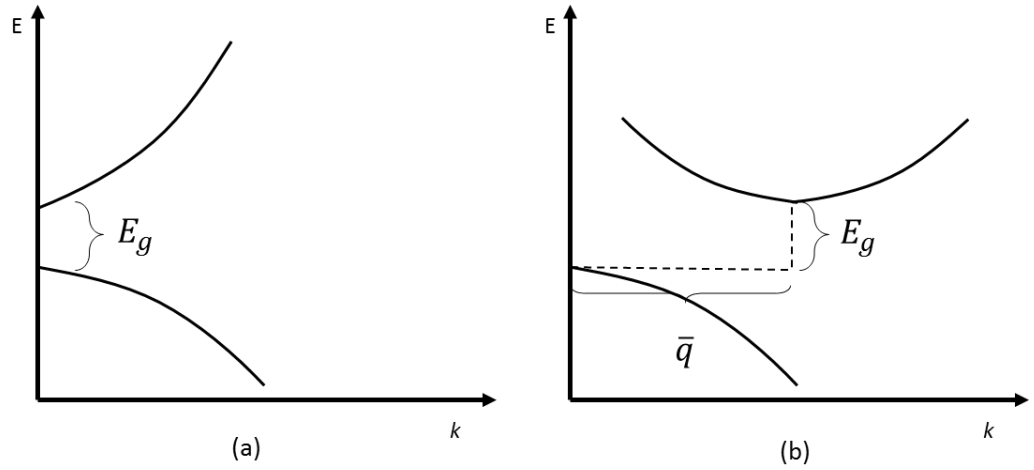

Figure 2-1 Energy-Crystal momentum diagram of Valence-Conduction band transitions of: (a) Direct band gap material (b) Indirect band gap material

2.1.2.4. Recombination

Recombination is the relaxation of an electron-hole pair to the equilibrium states; this can occur via different mechanisms. The main category of mechanisms of recombination are: radiative recombination, Auger recombination, Shockley Read Hall (SRH) recombination and surface recombination.

Radiative recombination

Radiative recombination behaves similarly to the photon absorption process, excepting in the reverse. For direct radiative recombination, the electron drops directly from the higher energy state to a lower state, generating a photon with the energy difference between the levels [13]. For indirect radiative recombination, the electron drops to the lower energy state from the higher

energy state only with the absorption/generation of a phonon to conserve both energy and momentum [13]. Due to the requirement of phonons, the radiative recombination is not the primary recombination mechanism in Si PV cells as Si is an indirect band gap material.

Auger recombination

Auger recombination is the recombination of an electron-hole pair in which the energy and momentum are absorbed by a third free carrier. This third carrier then thermalizes and relaxes back to the band edge [4]. Auger recombination is dependent on the dopants and their concentration, the band gap and the temperature of the material [8].

Shockley Read Hall recombination

As discussed before, dopants result in additional energy levels within the forbidden region. These levels act as possible centres for electron-hole recombination. The additional energy levels provide centres for electronic transitions within the forbidden region. That is, in the case of indirect band gap materials, they provide more probable transitions than the conduction-valence band transitions [13].

Surface recombination

Due to the discontinuity of the crystal structure of semiconducting devices at the surface, a large number of localised energy states (or generation recombination centres) are present [13]. In indirect semiconductors such as Si, this can play an important role in the enhancement of recombination rate near the surface.

2.1.3. P-N Junction

The formation of a diode requires the combination of p-type and n-type materials. Figure 2-2 (a) describes the band diagrams of the p-type and n-type before the formation of the p-n junction; Fig. Figure 2-2 (b) shows the change after the formation – the p-n junction is in thermal equilibrium. In the formation of the p-n junction, the Fermi level of the device is the same across the junction; therefore, the valence band and the conduction band of each region adjusts to accommodate this. The large carrier concentration gradients across the cell cause charge carrier diffusion. Free electrons are in high concentration in the n-region and low concentration in the p-region; therefore, they diffuse from the n-region to the p-region. Free holes are in high concentration in the p-region and low concentration in the n-region; therefore, they diffuse from the p-region to the n-region. The positive donor ions form an electric field (with electrostatic potential V_{bi}) with the negative acceptor ions. This built electric field opposes the diffusion current, causing drift current. The electron drift current flows from the p-region to the n-region, while the hole drift current flows from the n-region to the p-region.

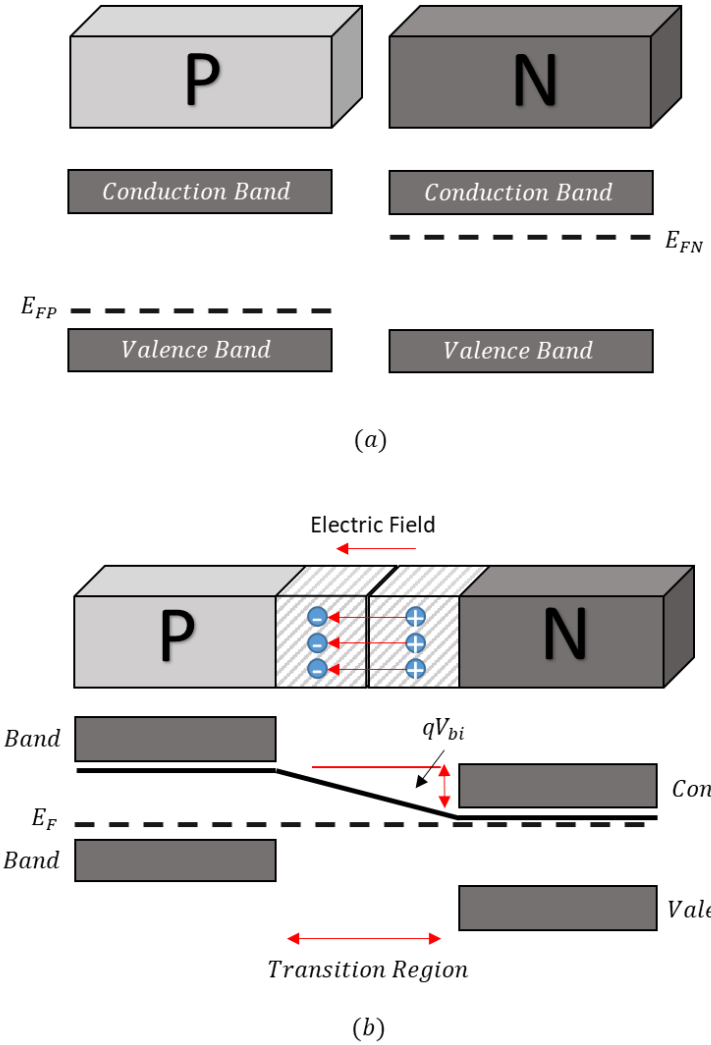

Figure 2-2 (a) Isolated n-semiconductor and p-semiconductor with associated band diagrams. (b) Formation of p-n junction and associated band diagram.

Figure 2-3 describes the p-n junction under forward bias. That is, the application of a positive potential (V_F) to the p-region with respect to the n-region. The electrostatic potential across the junction is decreased by the forward bias resulting in a potential of $V_{bi} - V_F$.

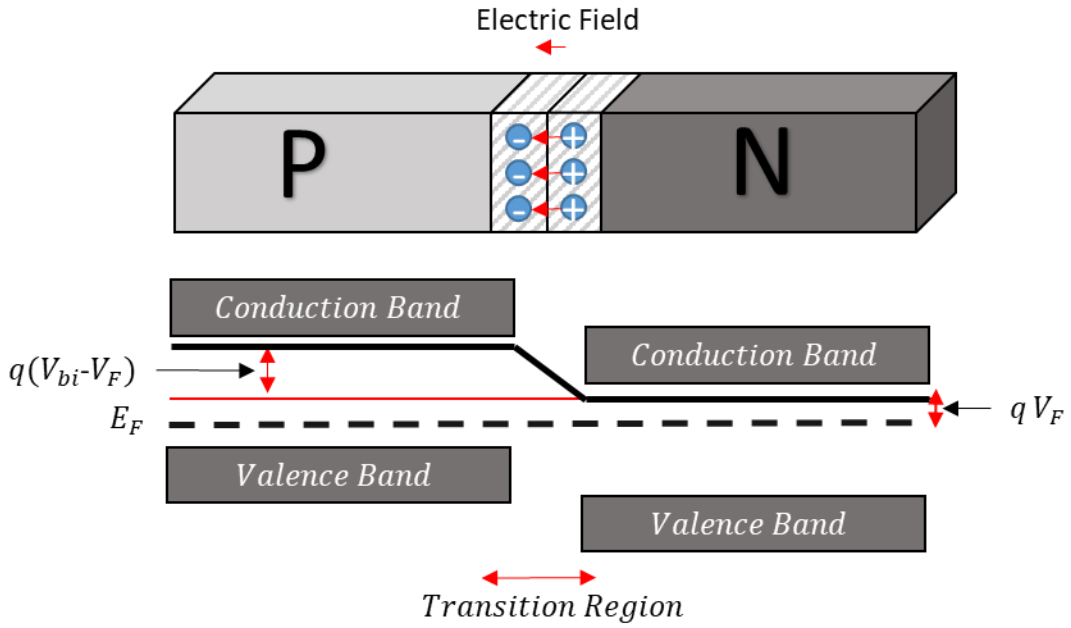

Figure 2-3 P-N junction and associated band diagram under forward bias

Figure 2-4 describes the P-N Junction under reverse bias. That is, the application of a negative potential (V_R) to the p-region with respect to the n-region. The electrostatic potential across the junction is increased by the reverse bias resulting in a potential of $V_{bi} + V_R$.

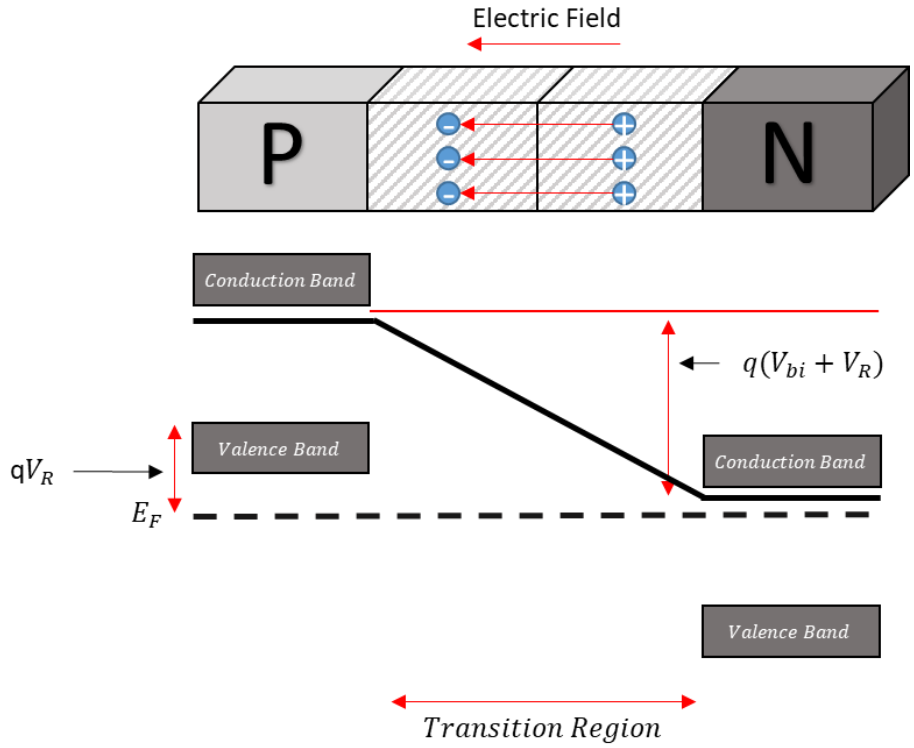

Figure 2-4 P-N junction and associated band diagram under reverse bias

2.1.4. Defects

2.1.4.1. Shunt currents

In most manufactured PV cells, there exist alternate current paths through the p-n junction. These pathways act as shunt paths, shorting the emitter and the back contact. For the remainder of this dissertation, the term shunt will be defined as shunt path. As shunts affect the current-voltage (I-V) response of a PV device, a shunt is included as part of the models applied to PV cells- see Section 2.1.5. There exist different types of shunts, according to Breitenstein, Rakotoniaina, Al Rifai and Werner [17]. These are:

1. Edge shunts:
    a. ohmic edge shunts are typically due to an incompletely opened emitter at the edge
    b. Non-ohmic edge shunts which can be interpreted as recombination sites
2. Extended Defects
    a. Figure 2-5 describes the model proposed by Breitenstein, Altermatt, Ramspeck, Green, Zhao and Schenk [18] which describes the process of ohmic conductivity across the continuum of states in extended defects in the band structure.

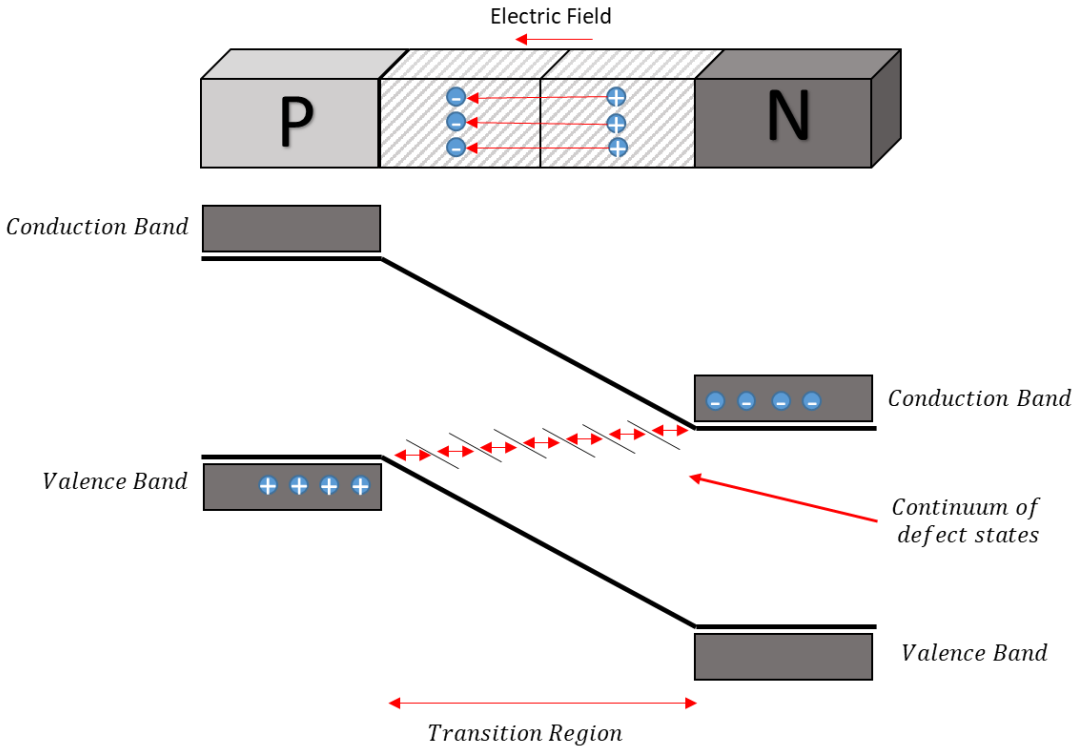

Figure 2-5 Proposed band diagram of ohmic conductivity across a continuum of states in an extended defect position.

3. Cracks
    a. Weak non-linear edge recombination [17].
    b. Ohmic crack shunt
        i. If the crack was present in the material before contact metallization, there is a possibility that an ohmic shunt can be formed. If the crack was present in the raw Si wafer, it is possible for an emitter layer to form across the crack, this layer shorts the emitter to the base contact - acting as an alternate current path [17].

4. Sintering process formed shunt
    a. To ensure a good response to shorter wavelengths (blue), the emitter thickness is generally in the order of 0.3 μm. The sintering process consumes part of the Si material. Non-optimized sintering can cause the metallization of the emitter to penetrate into the bottom p-region. This can lead to the formation of a Schottky-like shunt [17].

5. Scratch related shunt
    a. Scratches on the surface of the PV cell can bring the p-n junction to the surface (exposing a region of high density of recombination centres) [17]. If scratches do not penetrate the p-n junction or are present before the diffusion of the emitter layer, they generate local recombination centres.

6. Al contaminant shunt
    a. Al contamination on the surface of the cell before firing process can cause the formation of shunts. The firing process alloys the Al into the material, which can compensate the emitter which will lead to p-doped regions on the surface [17].

7. Crystallographic defect related shunts:
    a. Crystallographic defects can be related to recombination currents and if the recombination current is strong enough, it can act as a non-linear shunt [18][19]. Examples of such defects are small-angle grain boundaries, and dislocation tangles – most likely related to gettered impurities.

8. Si_3N_4 inclusions shunt paths

    a. Si_3N_4 inclusions appear in some cast multi-crystalline Si ingots, and it is proposed that the recombination activity of interface states between Si and Si_3N_4 is responsible for these shunts [17]. Breitenstein states that the most likely origin of the Si_3N_4 inclusions is contamination from the walls of the crucible used in the crystallization process [17].

9. Inversion layers

    a. The presence of fixed positive charges within specific grain boundaries cause a local transformation of the p-type to n-type; that is, a formation of carrier collecting inversion channels [17]. These channels can be connected both with the emitter and the back contact causing a short.

    b. Breitenstein et al [17] proposed that one of the defects responsible for material-induced shunts in cast silicon solar cells are cubic SiC filaments crossing through the bulk of the cell [17] [19]. They are n-conducting [17] and form a secondary junction with the p-type silicon base, which is parallel to the emitter and possibly collect minority carriers [6].

2.1.4.2. Reverse bias breakdown

An ideal diode limits current flow under reverse bias conditions; which is related to the increase in electric field, and is described mathematically by the diode model in Section 2.1.5. However, after the threshold reverse bias (breakdown voltage), the reverse current increases exponentially. Breakdown is characterised as large current flow in the reverse direction. In ideal conditions, the cells within a PV module do not experience reverse bias conditions. However, under partial module shading, individual cells may be reverse biased [20]. The application of a significant reverse bias across a PV cell may result in junction breakdown [21]. The reverse current does not flow uniformly through the device. There exists preferential current flow through localised shunts (as discussed above) and through breakdown sites. The different types of breakdown are as follows [21]:

1. Type I: Pre-breakdown
2. Type II: Defect-induced breakdown
3. Type III: Avalanche breakdown (AB)

Sites of junction breakdown at lower voltages (0V to 10V), are known as pre-breakdown sites. That is, these sites of breakdown occur well below the potential required for the two other types of breakdown. These breakdown sites are usually associated with recombination active defects such

as the Al precipitates. Lausch, Petter, Bakowskie, Czekalla, Lenzner, von Wenckstern, and Grundmann [22] propose that if an Al stain is present before the anti-reflective coating and contact firing, the process will form a metal/SiO_x/Si hetero junction, as shown in Figure 2-6. In that study, the proposed model was the formation of a metal/SiO_x/n^+-Si junction rather than a metal/SiO_x/p-Si junction due to the fact that light emission is observed for reverse bias only. It is proposed that the emitted light is due to radiative recombination of electron-hole pairs via intra-band levels in the SiO_x layer between the metal and the emitter. During the stacking of the cells, cross contamination occurs, leaving Al precipitates (Al stains) to be left on the surface [17]. During the firing process, the Al alloys, leading to the formation of the metal-insulator-semiconductor (MIS) junction described by Lausch et al [22]. Another explanation is that the Al doping may produce a Zener diode or an ohmic contact to the emitter layer, this is dependent on the doping concentration [23].

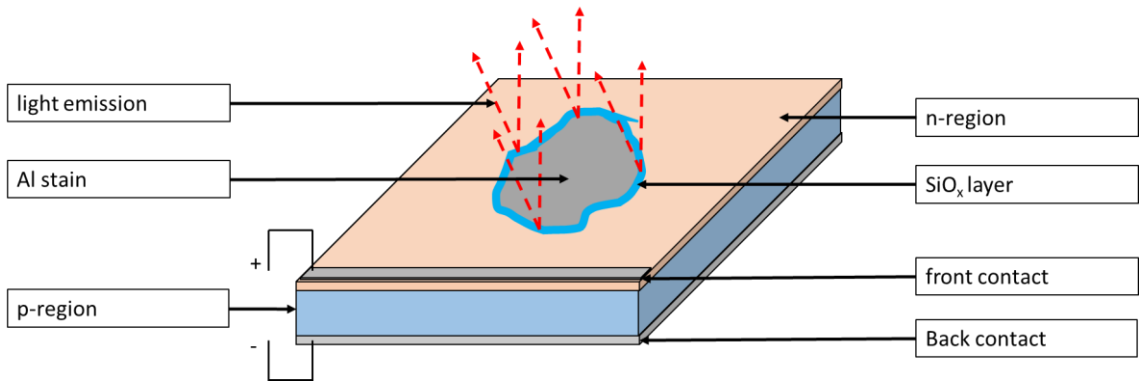

Figure 2-6 Diagram of the model proposed by Lausch et al [22].

There is another mechanism that is related to pre-breakdown light emission. Figure 2-5 illustrates the continuum of states that can cause ohmic shunting; however, in reverse bias the continuum of states (hopping via extended defects) can lead to light emission through radiative intra-band thermalisation of hot carriers [23][25].

Type II breakdown usually occurs within the range of 10V to 14V reverse bias and is associated with crystallographic defects [24]. It is proposed by Bothe, Ramspeck, Hinken, Schinke, Schmidt, Herlufsen, Brendel, Bauer, Wagner, Zakharov and Breitenstein [26] that internal field emission (IFE) via defect sites is a plausible explanation for breakdown events below 14V reverse bias. Figure 2-7 (a) illustrates the process of trap assisted tunnelling mechanisms for IFE breakdown; while, (b) shows the soft reverse breakdown I-V response. This type of breakdown is associated with recombination active defects such as Fe precipitates. Breitenstein, Bauer, Bothe, Kwapil, Lausch, Rau, Schmidt, Schneemann, Schubert, Wagner and Warta propose that Fe precipitates can be correlated with Type II breakdown sites [21]. It was found that the density of these breakdown sites significantly increased when the material has been facing the Si casting crucible [25].

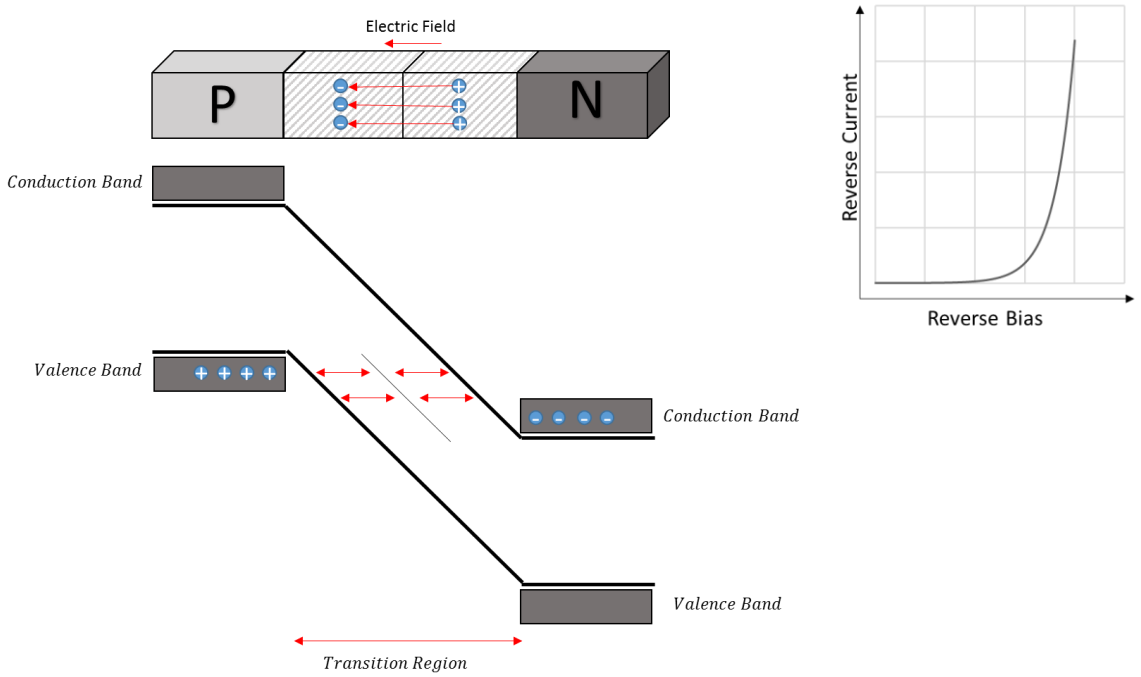

(a) (b)

Figure 2-7 (a) Band diagram of IFE breakdown. (b) I-V characteristics of IFE breakdown.

An alternative mechanism has been proposed that predicts the light emission for Type II breakdown. Figure 2-8 illustrates the model described by Breitenstein [25] that accounts for Type II breakdown. This model states that α – $FeSi_2$ needles are formed in the casting process in a grain boundary. The needles form an ohmic junction in the emitter which crosses through the p-n junction and forms a Schottky diode with the p-base [25]. The process of breakdown is then related to thermionic emission in the Schottky diode. It is also highly dependent on the geometry of the precipitate [25].

Type III breakdown sites usually occur with a reverse bias of above 14V, and is associated with avalanche breakdown (AB). In the ideal case, this type of breakdown occurs in the region of 60V, but during manufacturing, non-optimized etching may form etch pits at crystallographic defects. In the process of forming the emitter, the etch pits result in p-n junction bending [21][28]. Avalanche breakdown may also be caused by the bending of the p-n junction through the preferential diffusion of phosphorous at extended defects [21][28]. The electric-field-accelerated electrons interact with the crystal lattice. Under normal situations, the collision events decrease the kinetic energy of the electrons - preventing the electrons from ionizing the atom. However, if the potential is great enough (sufficient electric field), the kinetic energy of the electrons will ionize the atoms in the collision events (that is, excite electrons from the valence band to the conduction band) [28]. Figure 2-9 (a) describes the process of AB; while, (b) shows the hard-reverse breakdown I-V response.

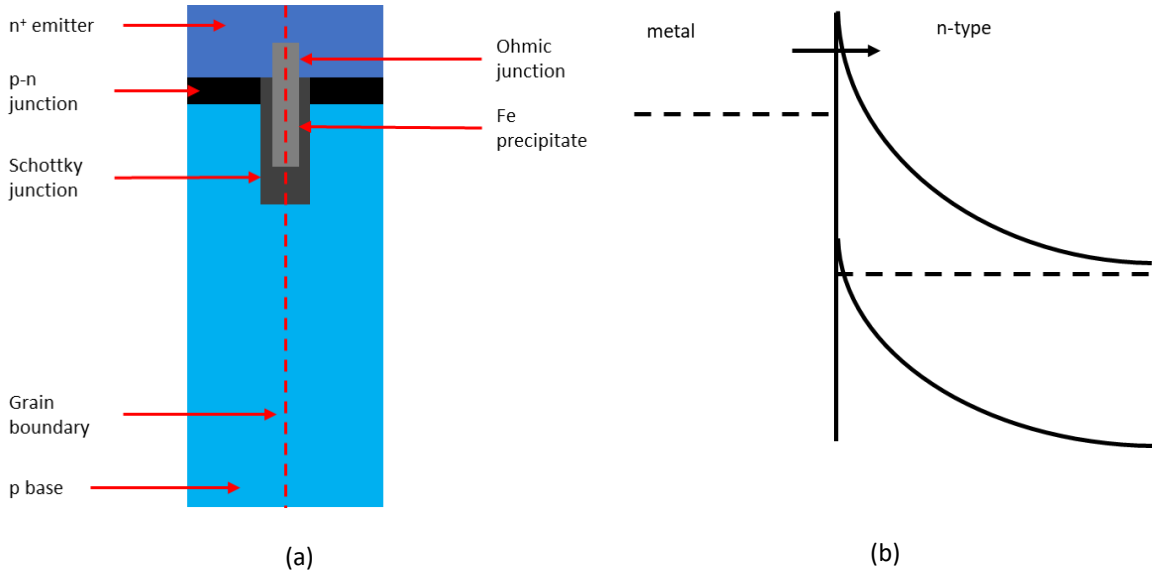

Figure 2-8 (a) Geometry of proposed Schottky breakdown mechanism. (b) thermionic field emission breakdown mechanism.

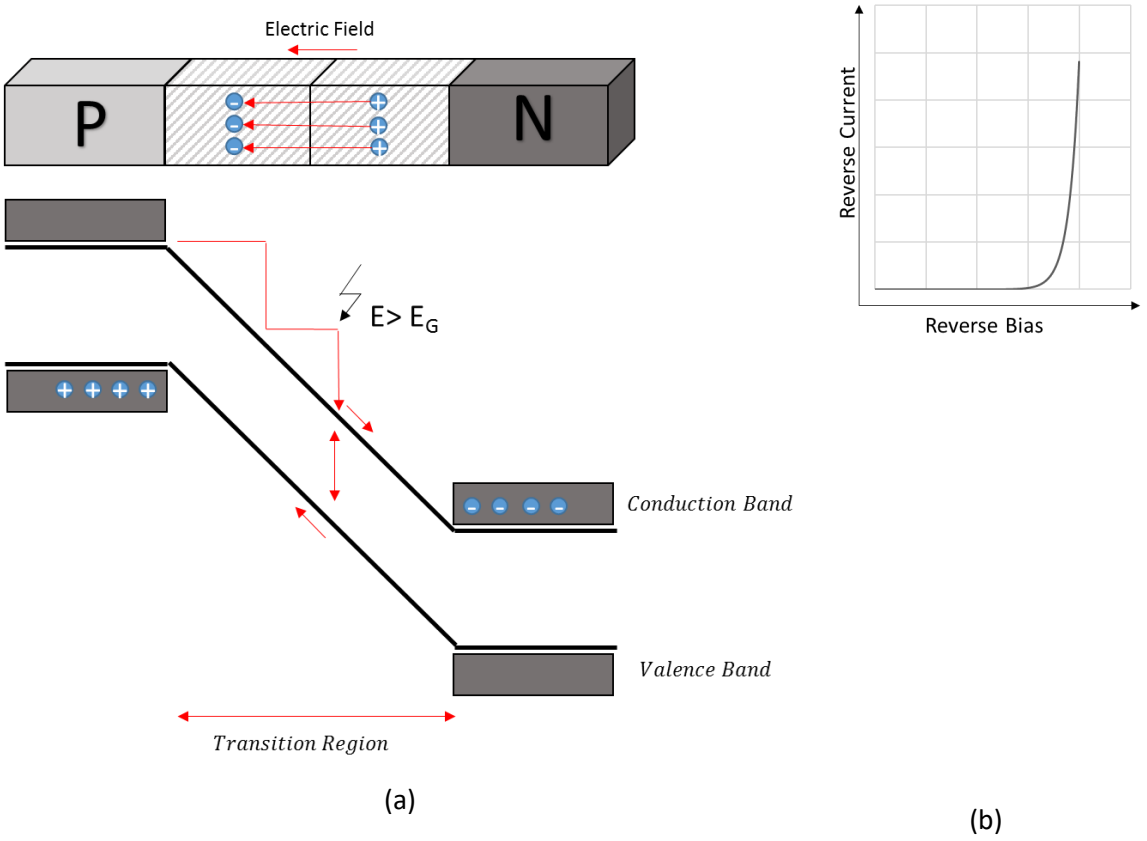

Figure 2-9 (a) Band diagram of AB. (b) I-V characteristics of AB breakdown.

2.1.5. Applied Models

There exist multiple models applied to PV cells relating to the I-V characteristics. Each model mentioned in this chapter has its own set of assumptions. There exists a set of models that describe the I-V relationship of PV cells and they vary in complexity from relatively simple to highly complex. The simpler models are often more practical and the parameters are easier to extract. The model used in the parameter optimisation in this dissertation is the non-ideal two-diode model. It provides an adequate description of the forward current-voltage relationship, while still maintaining the ease of two-diode parameter optimisation. For the sake of completeness, the one-diode model is presented, which is then extended to the two-diode model.

Ideal one-diode model

The ideal one-diode model assumes that the dark I-V characteristics of a PV cell can be modelled using a single diode, where the influences of parasitic resistances are assumed to be negligible. That is, there is no alternate current paths and the diode voltage (V_D) and the applied/measured/total voltage (V) are the same

Dark I-V relation:

$$I = I_0 \left[\exp\left(\frac{qV}{k_B T}\right) - 1\right] \quad \text{----------} (2\text{-}2)$$

where I_0 is the dark saturation current, q is the charge of the charge carrier, T is the absolute temperature of the device, k_B is the Boltzmann constant, I is the current through the cell and V is the measured voltage across the device.

Quantum efficiency varies with applied voltage of the device; however, in the case of the models used in this study, the photo-induced current is assumed to be a constant current source.

Light I-V relation:

$$I = I_0 \left[\exp\left(\frac{qV}{k_B T}\right) - 1\right] - I_L \quad \text{----------} (2\text{-}3)$$

where I_L is the photo-induced current.

Figure 2-10 shows simulated I-V characteristic curves of a PV cell in both the light and the dark. These curves were simulated for illustration and it was assumed that the device parameters remain constant regardless of the incident light. However, this is not always the case. Also note that the current and voltage units are arbitrary.

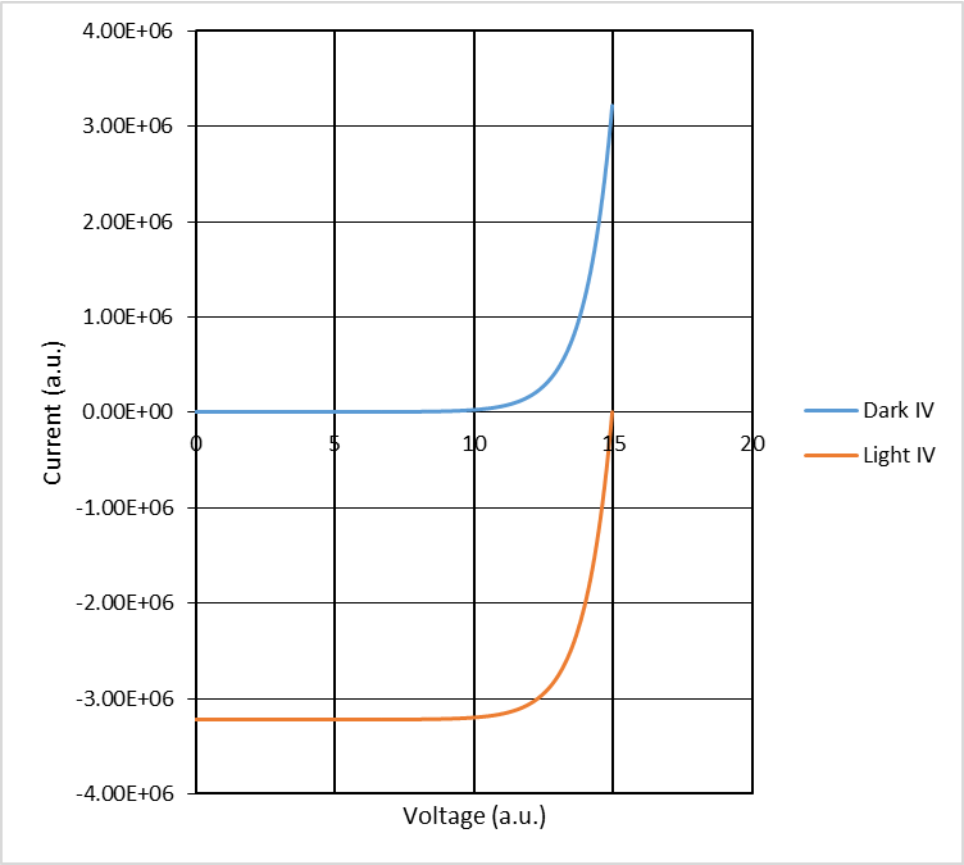

Figure 2-10 Simulated Light and Dark I-V curves of a diode

Non-ideal one diode model

Unfortunately, due to material quality, resistances due to the contacts, and internal shunts (as discussed in Section 2.1.4.1) the model applied to PV cells must contain parameters to describe such features. Figure 2-11 describes the assumed model in this case. The diode is not perfect; therefore, an ideality factor (n) is included so as a measure of how close the diode is to the ideal case. The ideality factor affects the voltage dependence of the model, the Schockley-Reed-Hall model for recombination in diodes allows for a value for the factor between 1 and 2. The shunt (R_{SH}) is assumed to be ohmic in nature as to simplify the model; however, as discussed in Section 2.1.4.1, it is not always the case. The shunt is an alternate current path parallel to the diode, ideally its resistance must be very large. Similarly, series resistance (R_{SE}) is assumed to be ohmic in response; this term is used as the collective resistance of the material resistance, finger and busbar resistance, contact resistance and any further resistance to the power source, load or measurement device.

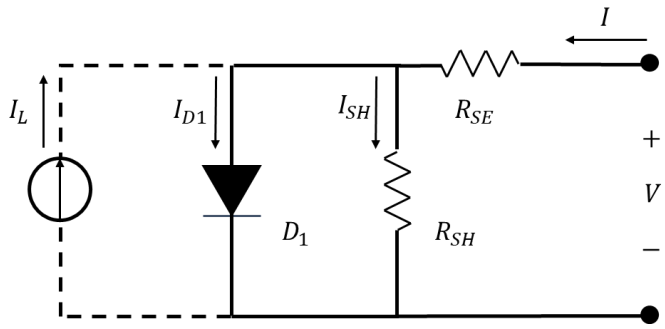

Figure 2-11 One-diode model circuit diagram

Using Kirchhoff's Current Law, the sum of the currents in a network of conductors' nodal point is zero.

This leads to:

$$I = I_{SH} + I_{D1} - I_L \quad \text{---------- (2-4)}$$

In dark conditions the photo-induced current reduces to zero.

Using Kirchhoff's Voltage Law, the sum of electrical potential differences around any closed network is zero.

This leads to:

$$V_D = V_{SH} \quad \text{---------- (2-5)}$$

where V_{SH} is the potential across the shunt resistor and I_{SH} is the current through the shunt resistor.

In the case of the dark conditions (PV cell being powered):

$$V = V_D + V_{RSE} \quad \text{---------- (2-6)}$$

where V_{RSE} is the potential drop across the series resistance.

Therefore, equation 2-7 accounts for the series resistance in the modelling procedure. As the voltage drop across the shunt resistance is related to the current through the system, and that the shunt is assumed to be ohmic in nature it is possible to calculate the voltage drop. This causes the I-V relation to become implicit. That is, an iterative process is required (such as the Newton-Raphson method) in the modelling of the relation.

$$V_D = V - IR_{SE} \quad \text{---------- (2-7)}$$

In the case of the light conditions:

$$V_D = V + V_{RSE} \quad \text{---------- (2-8)}$$

Similarly, in the light conditions, it is possible to calculate the potential drop due to the series resistance.

$$V_D = V + IR_{SE} \text{ ---------- (2-9)}$$

Dark I-V relation:

$$I = I_0 \left[\exp\left(\frac{q(V-IR_{SE})}{nk_BT}\right) - 1\right] + \frac{(V-IR_{SE})}{R_{SH}} \text{ ----------(2-10)}$$

Light I-V relation:

$$I = I_0 \left[\exp\left(\frac{q(V+IR_{SE})}{nk_BT}\right) - 1\right] + \frac{(V+IR_{SE})}{R_{SH}} - I_L \text{ ----------(2-11)}$$

Non-ideal two diode-model

Ideally, a PV cell would not have recombination during power generation. However, due to the nature of the device and its materials, different recombination mechanisms occur. To account for other recombination mechanisms (sometimes seen as non-linear shunts), a second diode is included parallel to the first, it has its own parameters such as saturation current, ideality, etc. Figure 2-12 is the equivalent circuit for the two-diode model.

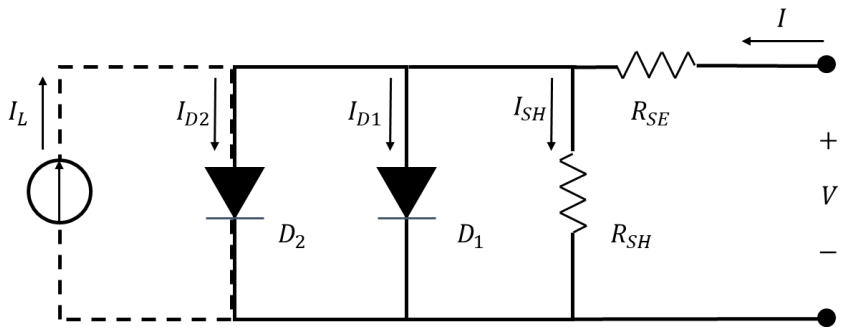

Figure 2-12 Two-diode model circuit diagram

Similar to the one-diode model, using Kirchhoff's Circuit Laws allows for the determination of a mathematical description of the two-diode model.

Using Kirchhoff's Current Law:

$$I = I_{SH} + I_{D1} + I_{D2} - I_L \text{ ---------- (2-12)}$$

where a subscripted number is an indication of each diode and in dark conditions the photo-induced current reduces to zero.

Using Kirchhoff's Voltage Law:

$$V_{D1} = V_{D2} = V_{SH}$$ ----------(2-13)

The potential drop due to the series resistance affects both the diodes as well as the shunt equally. The effect of the series resistance in the two-diode model is the same as the one-diode model.

Dark I-V relation:

$$I = I_{01}\left[\exp\left(\frac{q(V-IR_{SE})}{n_1 k_B T}\right)-1\right] + I_{02}\left[\exp\left(\frac{q(V-IR_{SE})}{n_2 k_B T}\right)-1\right] + \frac{(V-IR_{SE})}{R_{SH}}$$ -----(2-14)

Light I-V relation:

$$I = I_{01}\left[\exp\left(\frac{q(V+IR_{SE})}{n_1 k_B T}\right)-1\right] + I_{02}\left[\exp\left(\frac{q(V+IR_{SE})}{n_2 k_B T}\right)-1\right] + \frac{(V+IR_{SE})}{R_{SH}} - I_L$$ -(2-15)

The models described do not take into account various breakdown mechanisms present in PV cells. The spatially distributed diode nature of solar cells and the fact that the mechanisms can be localised can limit the development of a parsimonious model for cell breakdown I-V characterisation.

2.1.6. Summary

Semiconductor materials have band structures that describe the allowed electron states. The photovoltaic effect describes the generation of electron-hole pairs due to photo-stimulation. Due to dopants within a base material, additional energy levels are introduced into the band structure. The p-n junction is formed through the merging of an n-doped semiconductor and a p-doped semiconductor. Material and manufacturing defects effect the performance and longevity of PV cells. The electrical characteristics of a PV cell can be modelled using multiple applicable models that vary in complexity.

2.2. Electroluminescence (EL)

2.2.1. Introduction

Electroluminescence (EL) is a well-established technique and is used as a standard in PV cell and module testing. It has associated techniques that can be used to give spatial information about material properties such as minority carrier lifetime, diffusion length and series resistance [8] [29] [30].

The application of EL in the reverse bias is a technique that has gained popularity recently; this is due to the fact that in specific reverse bias ranges specific defects become apparent. Reverse bias EL (ReBEL) is used for spatially resolving junction breakdown sites across the PV cell and using a bias dependent approach can be used to characterise these junction breakdown sites [9].

2.2.2. Principles of EL

The principle of EL is the injection of charge carriers into the junction from the application of an electrical bias. For standard feature detection, the cell is under forward bias, the injected carriers move through the material until recombination. The intensity of the EL signal is related to the factors such as recombination mechanisms, material properties, optical properties and junction voltage [8]. The intensity of the EL signal (Ø) is proportional to the number of minority carriers [8].

Figure 2-13 shows the quantum efficiency of a Si-CCD camera (a common type of EL camera) at room temperature as well as the EL signal generated by a Si PV cell. The overlap peak between the sensitivity of the camera and the EL signal occurs at 1150 nm [31]. The small overlap between EL signal and Si CCD sensitivity is then measured by employing the appropriate filters.

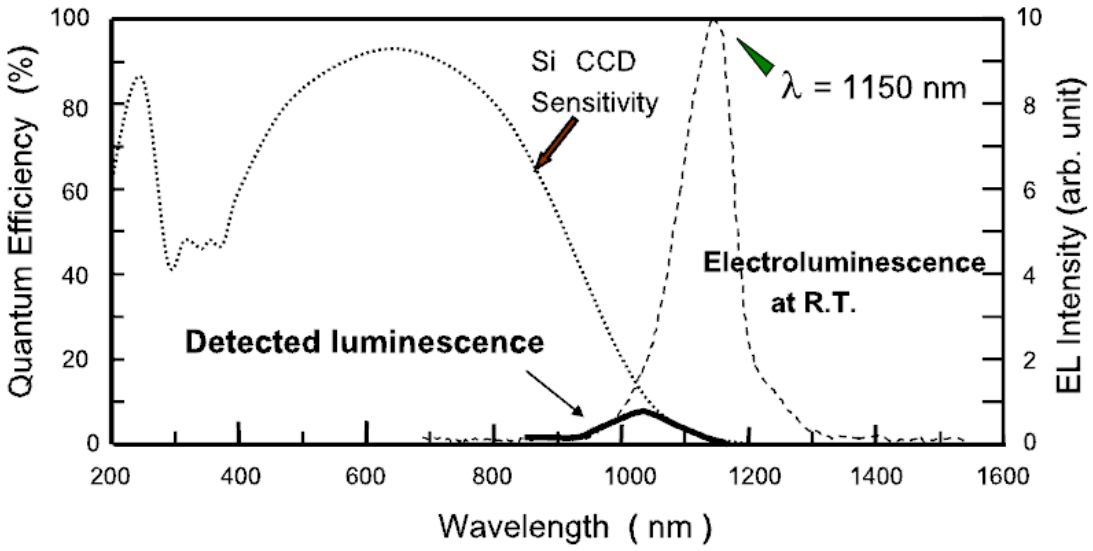

Figure 2-13 Quantum efficiency of Si-CCD camera and its relation to EL signal of Si PV cell [8].

2.2.3. Material Defect Characterisation

2.2.3.1. Intrinsic Defects

EL is the result of radiative recombination of charge carriers; therefore, the EL signal intensity is related to material properties that affect recombination [8]. The density of excess minority carriers and the diffusion length are such material properties [8]. The rate of recombination is related to the minority carrier lifetime and diffusion length of the material. EL signal is dependent on the device's material properties that effect the minority carrier density distribution. For example, the number of free electrons (n) in the p-region of the device can be modelled by equation 2-16, that is, can be expressed in terms of distance (x) from the edge of the p-n junction [32]. This equation takes into account the density distribution of minority carriers in the p-region and thus the dependence of the EL signal on the device's material properties.

$$n = n_0 \exp(-\frac{x}{L_e}) \text{---------- (2-16)}$$

Where L_e is the effective diffusion length and n_0 is the number of excess minority carriers at the junction edge.

Assuming that localised effective diffusion length varies across the surface of the device but is constant along its thickness (W) as done by Fuyuki et al [18]. The total number of electrons (N) in the p-region can be determined through the integration of equation 2-16 across the thickness of the cell (W).

$$N = n_0 \int_0^W \exp\left(-\frac{x}{L_e}\right).dx = n_0 L_e[1 - \exp\left(-\frac{W}{L_e}\right)] \text{ ----------(2-17)}$$

Using both equations 2-16 and 2-17 the effect of both temperature and diffusion length on the EL intensity can be noted through the proportionality between EL intensity and minority carrier density.

2.2.3.2. Micro-cracks

Si PV cells are manufactured of thin, fragile wafers; due to this fragility, micro-cracking appears readily in Si PV cells. The opto-electrical effect of these micro-cracks depends on the size, orientation and position on the cell. If a crack in the cell material prevents electrical contact to the area, either fewer carriers are generated or none at all - that is, there is a decreased EL signal. The decrease in radiative recombination in these areas renders these features visible in the EL image.

The classification of micro-cracks is discussed by Kőntges et al [33] and divided into 3 classes:

i. Class A: Micro-cracks are visible in the EL, but do not cause inactive areas of the cell.

ii. Class B: Micro-cracks result in an area of the cell that is darker in the EL image, but varies with applied current density.

iii. Class C: Micro-cracks completely remove areas of the cell from electrical contact which appear completely dark in the EL image.

2.2.4. Reverse Bias EL (ReBEL)

ReBEL is used to determine regions of reverse bias junction breakdown. Radiative recombination within a PV cell occurring under reverse bias is related to junction breakdown or pre-breakdown sites. The types of breakdown (I, II and III) were discussed in Section 2.1.4.2. The application of a voltage dependent ReBEL can be used to characterise the emission-voltage response of the breakdown sites. This process can be used to identify the type of breakdown occurring at the site rather than simply the location of the breakdown.

2.2.5. Voltage Dependent EL

Results obtained in a previous study at NMMU (Crozier et al) confirmed the bias dependence of EL in PV modules [29]. The method applied in a study by Hinken et al [30], describes the process which to map series resistance (R_{SE}) through the application of an algorithm to EL images obtained at different bias levels.

2.2.6. Series Resistance Mapping

Assuming the cell is made up of a network of parallel circuits consisting of individual series resistance (R_i^{SE}), shunt resistance (R_i^{SH}) and diode with a dark saturation current density (J_{0i}). Each pixel of the cell imaged is assumed to act as an independent parallel circuit, the EL emission of the ith circuit's diode ($\emptyset_i$) is described by [30]:

$$\emptyset_i = C_i e^{V_i/V_T} \text{ ---------- (2-18)}$$

where C_i is the calibration constant which contains the material and optical properties of the sample and the setup, V_i is the ith diode's voltage and V_T is the thermal voltage.

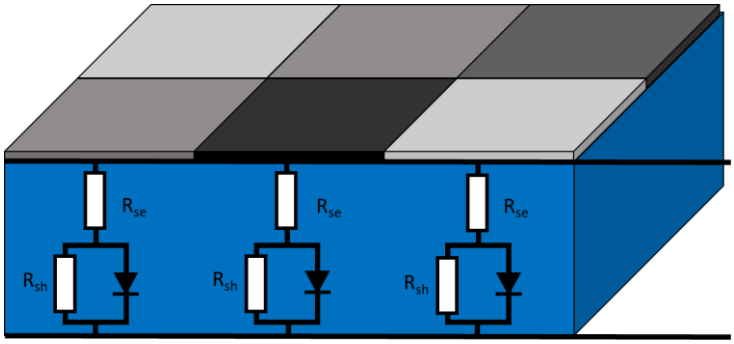

Figure 2-14 3-Dimensional model of a solar cell, network of parallel connected circuits

The derivation of the series resistance formula has been described elsewhere (Hinken et al) [30]. It makes the assumption that for each circuit represented by a pixel a voltage drop occurs due to the presence of series and shunt resistance. That is, the diode potential is equal to the difference between the applied voltage (V) and the voltage drop. These parasitic resistances are assumed to have an ohmic response. For each diode, it is assumed that the ideality factor is equal to one and the dark saturation current (J_{0i}) is injection independent.

This results in the following equation [16]:

$$J_i = J_{0i}\left(\frac{\emptyset_i}{C_i}\right) \text{ ---------- (2-19)}$$

$$\frac{V_T \emptyset_i'}{\emptyset_i} = a - b\emptyset_i' \text{ ---------- (2-20)}$$

where:

$$\emptyset_i' = \frac{d\emptyset_i}{dV} \text{ ---------- (2-21)}$$

$$a = \left(1 + \frac{R_i^{SE}}{R_i^{SH}}\right)^{-1} \text{ ---------- (2-22)}$$

$$b = -\frac{J_{0i}R_i^{SE}}{\left(1+\frac{R_i^{SE}}{R_i^{SH}}\right)C_i} \text{ ----------(2-23)}$$

This implies that after applying linear regression to $\frac{V_T\emptyset_i'}{\emptyset_i}$ vs $\emptyset_i'$, the series resistance can be calculated for each point using the constants a and b:

$$R_i^{SE} = -\frac{C_i}{J_{0i}} * \frac{b}{a} \text{ ---------- (2-24)}$$

Using the fact that the sum of all the i[th] current densities is equivalent to the external current (*I*) over the area imaged by each pixel (*A*), summation of equation 2-19 over all the i[th] circuits yields:

$$\frac{I}{A} = \sum J_i = \sum J_{0i}\left(\frac{\emptyset_i}{C_i}\right) \text{ ---------- (2-25)}$$

$\frac{J_{0i}}{C_i}$ is assumed to be laterally homogeneous and is therefore not dependent on the point on the cell.

Therefore, equation 2-24 can be written as:

$$R_i^{SE} = -\frac{A\sum\emptyset_i}{I}\frac{b}{a} \text{ ---------- (2-26)}$$

Applying this algorithm to the data obtained would facilitate the series resistance mapping of the cell. Series resistance for each circuit represents the total resistance from the source to the diode, including emitter, contact, bus-bar and finger resistances.

Due to the nature of acquired data a two-point numerical differentiation technique was applied based upon Taylor's Polynomial [34]:

$$\emptyset_i'(V) = \frac{\emptyset_i(V + \Delta V) - \emptyset_i(V - \Delta V)}{2\Delta V} + \frac{\emptyset_i'''(\xi)}{6}(\Delta V)^2 \text{ ---------- (2-27)}$$

where $\xi\ \epsilon[V - \Delta V, V + \Delta V]$

The final term in equation 2-27 is the error term associated with two-point numerical differentiation, this term is proportional to the third power of the difference in the applied voltage.

2.2.6.1. Breakdown Voltage Mapping

Voltage dependent ReBEL contains emission-voltage data of each point of a cell sample. Based upon the assumption that when the emission (in reverse bias) is greater than the background, the point has undergone some sort of breakdown, it is possible to use the emission-voltage data to map the breakdown voltage of a cell. The minimum reverse bias at which emission occurs is then defined as the breakdown voltage of the point in the case of this study. The three-dimensional data set contains emission-voltage data for each pixel on the surface of the cell. Each pixel is treated as an individual diode in the parallel network of diodes assumed as the model for the cell. Breakdown is highly localised, adding credence to this assumption.

An algorithm is required to search through the emission-voltage data within the matrix. The algorithm searches for the minimum value, for each "pixel" diode, at which light emission is greater than the background signal.

2.2.7. Summary

EL can be used as a spatially resolved indicator for the quality of a PV cell. The application of varying bias (both forward and reverse) can be used to determine more information than conventional EL. EL can be used to characterise spatially resolved features.

2.3. Dark Infrared Thermography

2.3.1. Introduction

IR radiation emitted from a surface is proportional to the fourth power of its absolute temperature [35]. IR thermal cameras are used to capture thermal images, and in the case of PV cell testing, to spatially resolve the temperature differences across the cell.

IR Thermography is achieved through the use of an IR imaging camera. The imaging is possible due to the emission of electromagnetic (EM) radiation due to the temperature of an object. This is described by Stefan's law [35]. Through the use of appropriate optics to focus the emitted IR radiation onto the camera's IR detector and Stefan's law, it is possible to spatially resolve temperature variation across an object.

$$P = \sigma A \epsilon T^4 \text{ ---------- (2-28)}$$

where P is the power output of the EM radiation of an object, A is the surface area of the object, ϵ is the emissivity constant of the surface and T is the absolute temperature, and σ is the Stefan-Boltzmann's constant, $\sigma = 5.6696 \times 10^{-8} Wm^{-2}K^{-4}$.

2.3.2. Device Defect Characterisation

IR thermography can be used in the identification of different types of defects in PV cells, namely shunts and junction breakdown sites [9][10][17][19][21]. At lower voltages near the maximum power point of a single Si PV cell (approximately 0.5V) the identification of shunts becomes possible [10]. Through the voltage dependent IR thermography and comparison to voltage dependent ReBEL it is possible to differentiate between large shunts and junction breakdown. If a shunt is large enough to be detected both in the forward and reverse bias with the same approximate temperature at the same level of bias, the shunt is of ohmic type. For example, if there exists a feature in a thermograph at a specific reverse bias and it is not visible in the ReBEL image, the feature is a shunt or non-radiative recombination site.

Lock-in Thermography is a form of IR Thermography in which the device is periodically stimulated (electrically, optically, or thermally); this minimises the effect of thermal blurring - that is, the spreading of heat due to thermal conduction throughout the device. Dark Lock-in Thermography (DLIT) is associated with pulsed electrical stimulus to the device. This technique can be used in the identification and characterisation of shunts and junction breakdown sites [9][10][17][19][21]. However, DLIT is beyond the scope of this study.

2.4. Light Beam Induced Current Measurements

2.4.1. Introduction

Light Beam Induced Current (LBIC) measurements form part of the non-destructive spatially resolved characterisation techniques used on PV cells. A focussed light beam probe is scanned across the surface of the cell; this induces a current (or potential). This induced current can then be measured as a function of position on the cell surface [12]. Variation in induced current can give an indication of current collection limiting features across the cell [12].

2.4.2. Principles of LBIC

LBIC measurements make use of different light sources so as to characterise PV cells. A focussed light beam probe is raster scanned across the device causing a local opto-electrical response. Relating the response to the position of the probe on the device gives an indication of local cell performance. Features affecting opto-electrical response can then be identified. Figure 2-15 illustrates how an LBIC response map is obtained through the scanning of a laser beam probe across the surface of a PV cell.

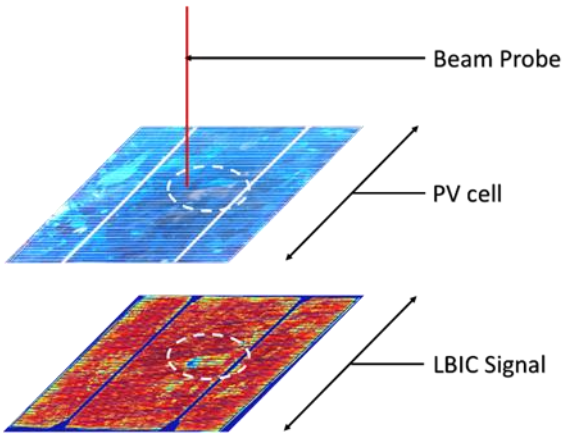

Figure 2-15 Laser beam probe scanned across the surface of a Si PV cell and its resultant LBIC map.

2.4.3. Device Defect Characterisation

LBIC provides spatial photo-induced current data, the contrast of which gives indication of various current collection limiting features. The main contrast is from the shading effect due to the front contacts of Si PV cells [12]. The light is reflected off the busbar and fingers. Defects such as microcracks, grain boundaries, dislocations and other such defects can also be noted in the contrast of the LBIC image [12][35]. In Figure 2-15, the feature highlighted in both the optical and LBIC image is an example of a region of cell lacking the antireflective coating. The decrease in photo-generated current is related to the loss through reflection or related to SiN_3 inclusion [17].

The application of a varying potential can be used in conjunction with the local illumination for the acquisition of local light I-V response [12]. Applying a parameter optimization technique on the data obtained in that process can then be used to map the various operational parameters of the cell.

2.5. Genetic Algorithm Parameter Optimisation (GAPO)

2.5.1. Introduction

The models relating current and voltage for a diode and other related systems contain many parameters (equations 2-10, 2-11, 2-14 and 2-15). The relations often contain multiple terms hindering explicit formulae for specific parameters. Optimisation procedures can be used to fit the model to the data. In a study by J.A. Jervase [36], a Genetic Algorithm (GA) was successfully tested against simulated I-V data sets of various parameters. In the current study, a GA is proposed as the solution to the Parameter Optimisation (PO) of the solar cell I-V models.

GAs are based upon biological processes such as genetic crossover during sexual reproduction; in other words, GAs model genetic evolution [37]. A set of proposed parameters, a single solution, is referred to as an individual. As a GA makes use of multiple parallel solutions, the set containing all individuals of an iteration (generation) is referred to as the population. Due to the parallel set of

solutions which cover the search space, GAs are in some cases more likely to acquire a global minimum error for the parameters obtained for the model applied to the data than classical techniques [38]. Alternate more classical approaches such as the Gradient Descent [38] approach are prone to acquiring only local minima.

2.5.2. Principles of Genetic Algorithm Parameter Optimisation

Figure 2-16 describes the basic structure of GAs. GAs require an initialisation step, where the first generation of the population is randomly created. The closer the initial guesses are to a global minimum, the faster the GA will acquire it. The next step is the fitness evaluation of the population and is case specific. The fitness evaluation allows for optimal individuals to be selected. This leads into the next step, the selection process. In this step, individuals are selected either by random or specific criteria based on their fitness. The selected population is referred to as the breeding population. The individuals selected in the previous step are then used in the crossover process, where the genes of a pair are combined (similar to the recombination of genes in biological processes). The GA that is used in this study makes use of a chromosome representation, that is the parameter values are directly encoded into each individual. The set of individuals that are formed in the crossover process are referred to as the offspring population. The following step is the mutation step, one of the key operations of GAs. The mutation step is a random perturbation that is applied to random genes within the population. This entire process, except the initialisation step, is repeated until the stopping conditions are met.

The validation of the parameters obtained is important in parameter optimisation. Therefore, the data is partitioned into two mutually exclusive data sets, the training set and the validation set [37]. In this study the data is split into 80% training data and 20% validation data. The training set is used in the optimisation of the parameters for the data. The validation set is used post-optimisation to validate the set of parameters obtained from the training set by checking the generalisation of the proposed parameters against unseen data [37]. Sections 2.5.3 to 2.5.8 describe each step in further detail.

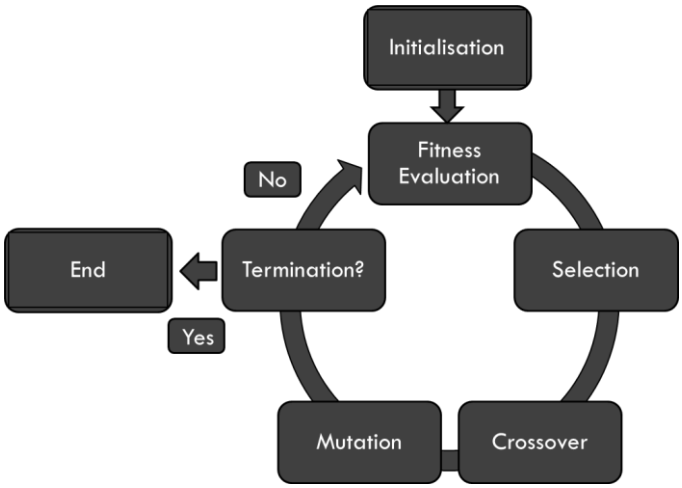

Figure 2-16 Genetic Algorithm Process Diagram

2.5.3. Initialisation

In terms of the GA used in this dissertation, the initialisation step is guided by specific bounds that allow the parameters to have physically realisable values. That is, parameter values are randomly generated within the specific bounds for each parameter. Figure 2-17 illustrates how the initial population can be distributed across the solution space with regards to a single parameter. Each number represents an individual in the population. As shown, depending on the values for the parameter (x-axis) the error function (y-axis) can have local minima (crosses) and a global minimum (circle).

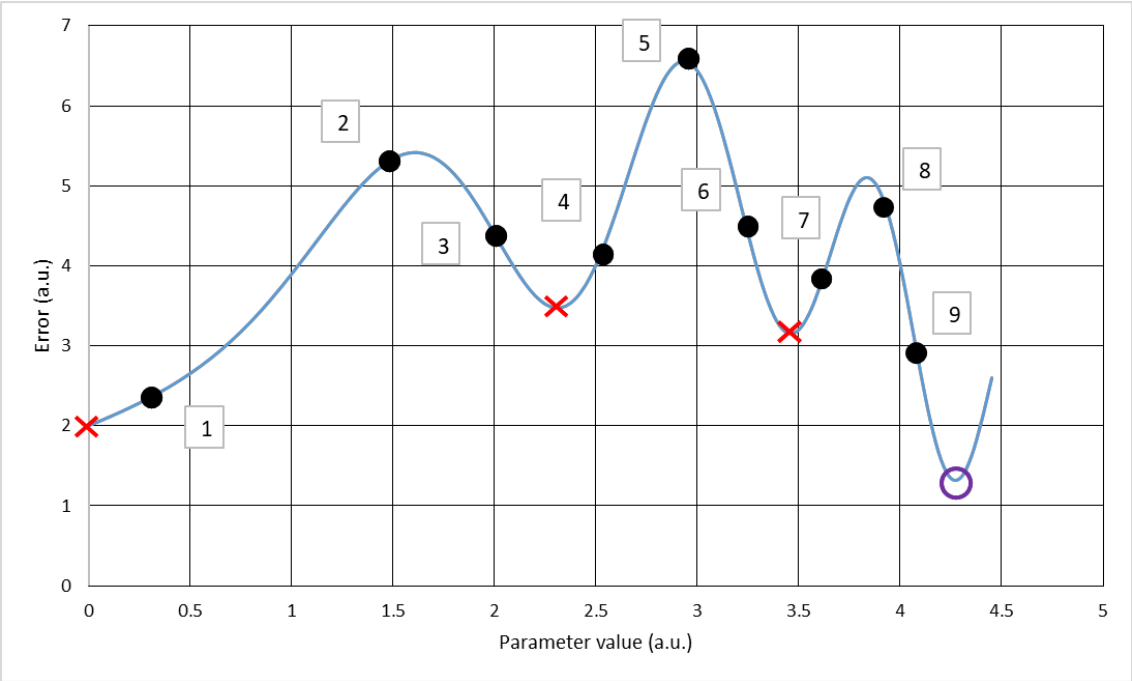

Figure 2-17 Idealised case for error of a given parameter value, arbitrary units (a.u.)

2.5.4. Fitness Evaluation

One of the other important steps of GAs is the method in which the fitness of each individual is evaluated. In this dissertation, a unique choice for fitness evaluation was selected. As shown by the example in Figure 2-18, the training set is broken into 10 separated regions dependent on the voltage. The relative root mean square error (RRMSE) (equation 2-29) is then calculated for an individual against the training set, for each region. The total error (TE) of the individual is then calculated as a weighted sum of the regional fitness values. The weighting is used to punish regions that show poor fitness. The weighting is described by equation 2-30. In the case of the example in Figure 2-18, regions 1 and 2 have small error values while regions 9 and 10 have large error values. Therefore, it is important to focus on improving those regions in particular. It must be noted that a standard approach to the fitness evaluation, that calculation of simply the root mean square error of all of the training data was used. However, due to the exponential relationship, the error values obtained for the higher voltage ranges skewed the result. Therefore, RRMSE was used instead as it normalises the error for all the data. The region-specific approach was used because parameters in the I-V model applied to PV cells (equation 2-14) affect the curve in very particular regions. In development of the GA used in this study, a standard approach to fitness evaluation was used at first. The RRMSE was calculated over the entire voltage range. However, it was outperformed by the region-specific approach, leading to the use of the region-specific approach in this study.

$$RRMSE = \frac{\sum_{i=1}^{n}\sqrt{\left(\frac{Y_i - \check{Y}_i}{Y_i}\right)^2}}{n-1} \text{ ---------- (2-29)}$$

where n is the number of observation, Y_i is the i[th] observation and $\check{Y}_i$ is the predicted value for the i[th] observation by the proposed solution.

$$TE = \sum_{j=1}^{10} \propto_j RRMSE_j \text{ ---------- (2-30)}$$

where:

$$\propto_j = \begin{cases} 2, if\ RRMSE_j is\ greater\ than\ all\ other\ subfitness\ values \\ 1, otherwise \end{cases}$$

where *j* is the *j[th]* region

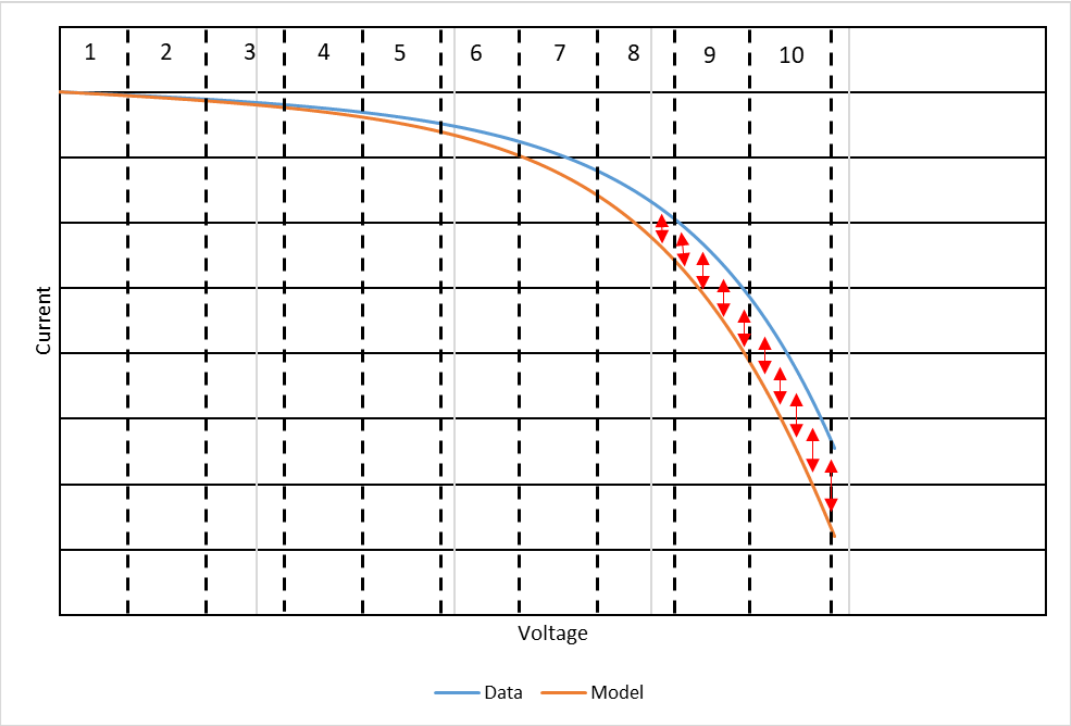

Figure 2-18 Region specific fitness evaluation example.

2.5.5. Selection Process

The selection process of the breeding population can affect the performance and convergence of the GA to the global minimum of error. Random selection of the breeding population does not consider the fitness of the individuals [37]. This allows for greater diversity in the population set. However, when using this method there exists the possibility of the fittest individuals not breeding as this selection method does not consider the fitness evaluation of the population. Another method is to favour the selection of the individuals with the greatest fitness [38]. However, there exists the possibility of non-convergence to the global minimum due to limited genetic diversity.

In the GA used in this dissertation, a combination of the two methods mentioned above was used for selection. That is, a fraction (13%) of the fittest individuals for each fitness region are selected for the breeding population; and the remaining portion of the breeding population are randomly selected individuals from the population.

Using the example in Figure 2-17 shows the importance of the inclusion of a randomised approach to selection. Without the random selection process and only using a process based upon fitness, the likelihood of 8 to be selected for crossover would be minimal. However, a minor change in its parameter value would lead to a much lower error than individual 1. The importance of this becomes apparent in the following section. There are many other types of selection procedures in GAs such as roulette wheel selection [37]; however, the approaches used were deemed adequate.

2.5.6. Crossover

The crossover portion of the GA is where the selected individuals have their genetic material combined. There are many factors involved with this process that can affect the outcome of each generation. For example, “elitism”, where a portion of the fittest individuals pass unchanged into the next generation [39]. This allows the GA to never regress in its progress towards a global minimum. Another factor to consider is the breeding of elite individuals in descending order of fitness. This allows the fittest individuals to crossover, with the possibility of a fitter offspring. However, this can decrease the diversity in the population, which can cause the GA to not converge to a global minimum.

For the first portion of the offspring generation (50%), breeding pairs are selected in descending order of fitness. The selected breeding pairs had three crossovers each, that is:

Offspring 1 = 75% of first parent + 25% of second parent

Offspring 2 = 50% of first parent + 50% of second parent

Offspring 3 = 25% of first parent + 75% of second parent

The remaining portion of the offspring is generated from 50:50 crossover of randomly chosen pairs from the breeding population. Returning to the example, assuming a mixture of the methods discussed above, with averaging of the parameter value was used for simplicity. Figure 2-19 is therefore a plausible result of crossover. Summarising the results:

1+3: Small improvement relative to 3 but less fit than 1

1+9: Less fit than both 1 and 9, near local minimum

3+7: Drastic deterioration from both 3 and 7

7+9: Slight deterioration from both 7 and 9

8+9: Small improvement relative to 8 but less fit than 9, closest to global minimum

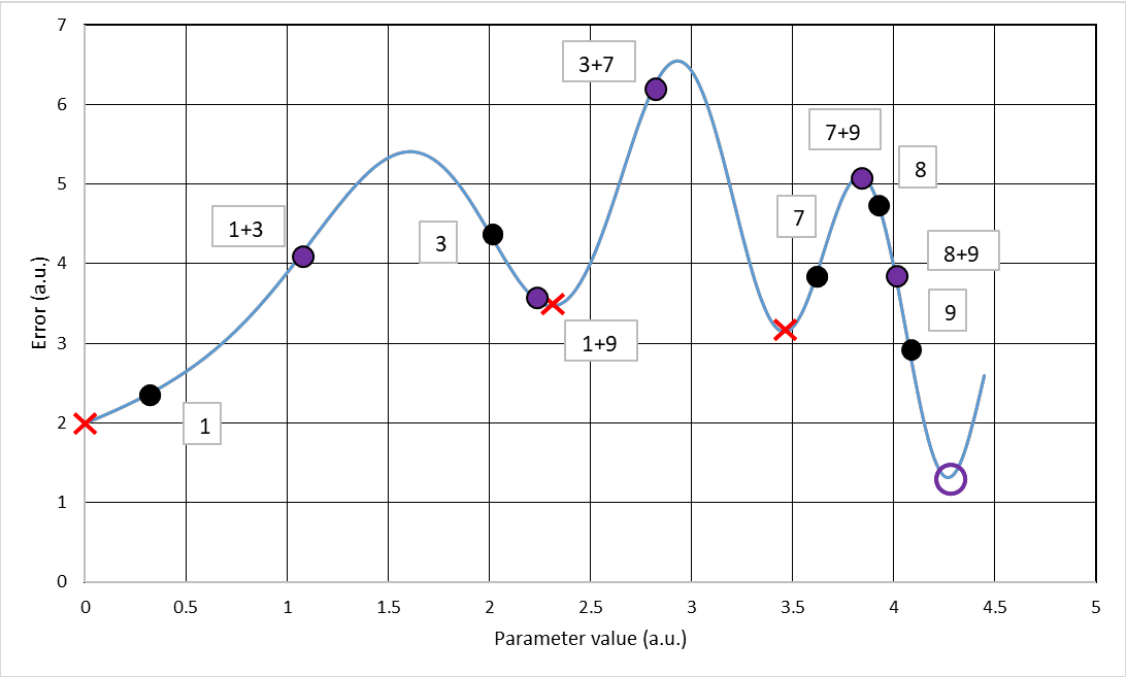

Figure 2-19 Result of crossover process in terms of error of offspring parameter value

2.5.7. Mutation

Mutation, in terms of GAs, is a random change in the genes of the individuals of the population. Similar to biological mutation, this can have a positive or negative effect on the individual in which the mutation occurs. Mutations allow for the exploration of the solution space [40]. The rate of mutation is the likelihood of the mutation of a particular gene of a particular individual in the offspring population. The specific rate of mutation in the population is an important factor to take into account.

If the rate is too low, the population might converge prematurely, not acquiring the global minimum. However, if the rate is too high it could cause the population to not converge effectively. Another possibility is an adaptive mutation rate [41]. In this study, as the number of generations increases the ratio between types of mutation changes. This is done so that for the earlier generations, the mutation allows for greater exploration of the solution space and later for exploitation of fit individuals. The type of mutation is another important factor for the algorithm. One type of mutation is the change of the gene to some random value within the gene's initialisation bounds – causing a possible massive change in the individual's fitness ("non-proportional mutation"). Another type is mutating a specific gene proportionally to its value – causing a possible minor change in the individual's performance ("proportional mutation"). Equation 2 - describes the change in a parameter value due to "proportional mutation".

$$\aleph' = (1 \pm \gamma)\,\aleph \quad \text{---------- (2-31)}$$

where $\aleph'$ is the mutated parameter value, $\aleph$ is the original parameter value and γ is a random value within the range of (0, 0.05)

In the GA used in this dissertation, a large mutation rate (50%) was chosen with an adaptive rate. The individuals in the population were randomly selected to be mutated, then within the randomly selected individuals, the genes were randomly selected to be mutated. At the start of the GA process, the type of mutation is split 50:50 between the mutation types discussed above. However, as the number of iterations increases, the ratio between the total number of "proportional mutations" and the total number of "non-proportional mutations" increases. This allows for the exploration of the solution space at the start of the GA, while as the GA continues the minor perturbations to the population offer small improvements (or deterioration) to the fitness of the individuals – that is, the mutation then allows for exploitation of the already fit population.

Based upon the example from above, Figure 2-20 shows the effects of mutation (indicated by the apostrophe; for example: for individual k, k' is the mutated variant) on the result of the GA. Individual 1' shows the effect of a "non-proportional mutation"; while individual 9' shows the effect of a "proportional mutation". Individual 1' shows an improvement in terms of being nearer to the global minimum while its fitness is decreased. Individual 9' shows both an improvement in terms of being nearer to the global minimum and its fitness is improved.

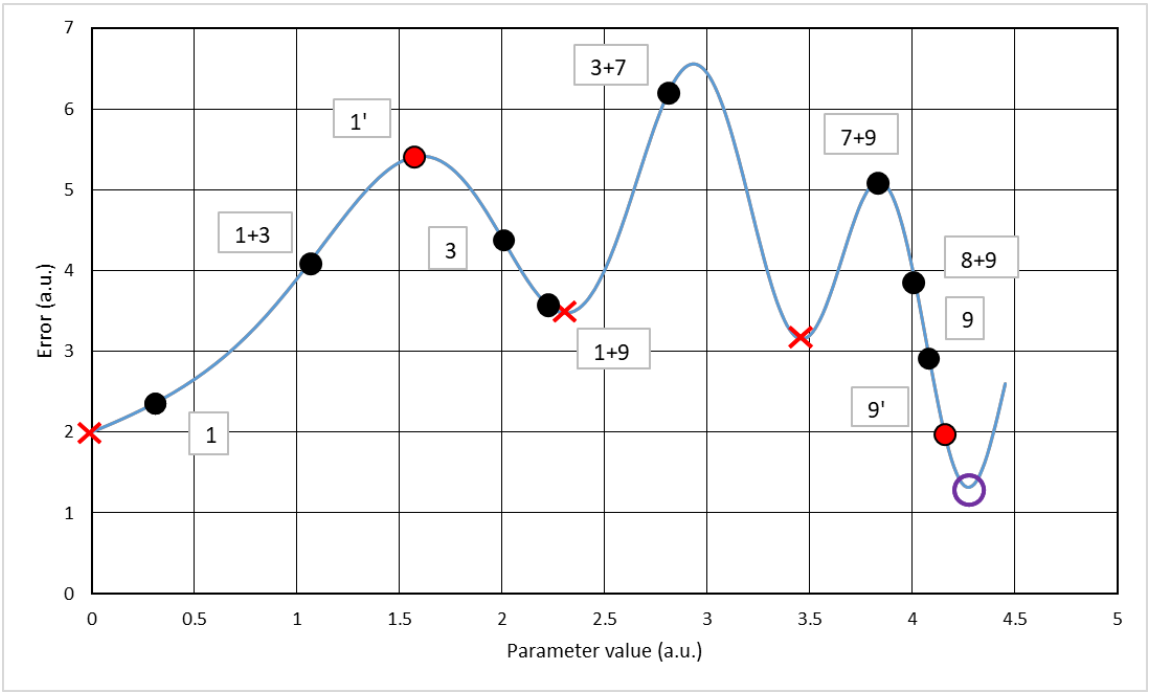

Figure 2-20 Result of the mutation process applied to the previous example

2.5.8. Termination

The termination of the GAPO process is important as the computing time versus the accuracy of the final result needs to be optimised as much as possible. Therefore, problem specific stopping conditions are required. In the case of the GA in this dissertation, two conditions were used. The first condition was the total number of iterations. Once a specific number of iterations (100) were completed, the process is terminated. The second condition is that a minimum RRMSE (0.00001%) for the training set was achieved. After the second condition is met (regardless of whether the maximum number of iterations has been completed) the process is terminated, otherwise the process is terminated after the first condition is met.

2.5.9. Summary

In summary, GAs are applicable to parameter optimisation for I-V curves for PV cells due to the complexity of the two-diode model of which the second diode term can be associated with defects current mechanisms. GAs are customisable on every level of the process; from a specific method for initialisation, problem specific fitness function, and unique selection, crossover and mutation processes. GAs have rarely been used on solar cell I-V curve parameter optimisation; therefore, it is also relatively novel in this application.

3. Experimental Design and Procedures

3.1. Introduction

One of the objectives of this dissertation is the design and construction of a system capable of performing Electroluminescence (EL), Infrared (IR) thermography, Light Beam Induced Current (LBIC) measurements and their associated techniques. This chapter details the overall system design and experimental procedures used in this dissertation. The system was designed with flexibility in mind so as to accommodate different sized samples, with varying spatial resolution capabilities. The components are listed for each subsystem in their corresponding sections.

3.2. Overall system design

3.2.1. Enclosure

The enclosure was designed to allow for the LBIC, EL and IR thermography systems to be contained in one unit. The entire structure was matte-black powder coated to minimize reflections. The side and door panels are made from sheets of high-density polyethylene (HDPE) with Al covers. The enclosure's frame is constructed out of Al extrusion, in which the shelving can be set at specific heights. The shelves consist of Al extrusion frames in which optical bread boards are mounted - all of which is powder coated black in order to minimise reflections.

Figure 3-1 shows the CAD drawing of the enclosure with the sub-systems contained therein.

Figure 3-2 is a photograph taken of the initial version of the enclosure. The positioning of the EL camera, IR camera and the LBIC system remains the same. However, for the results obtained for this study: the EL setup included an 850nm long pass filter; the LBIC system included an F-scan-theta lens.

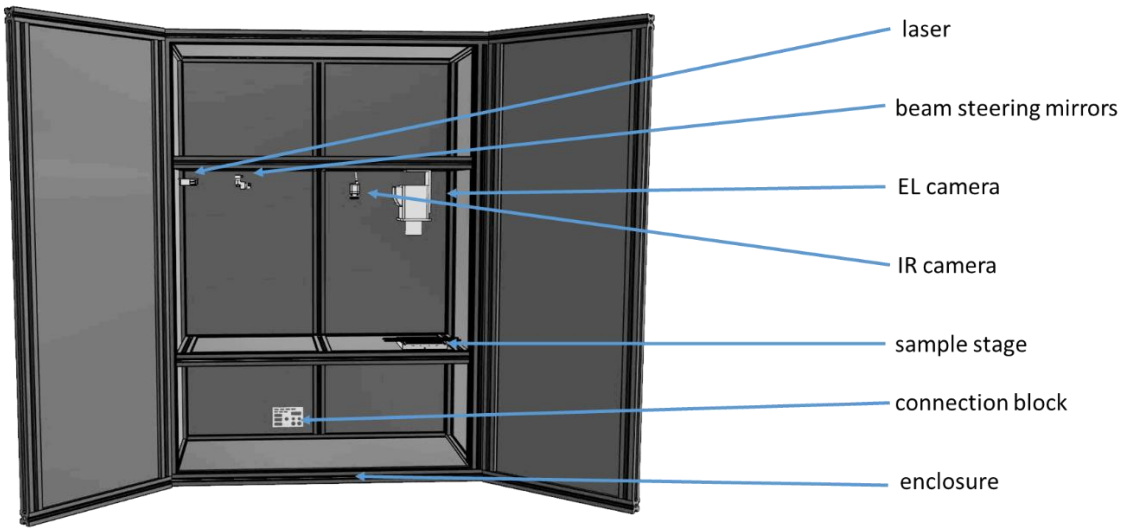

Figure 3-1: CAD drawing of the enclosure, with approximate positioning of the instrumentation.

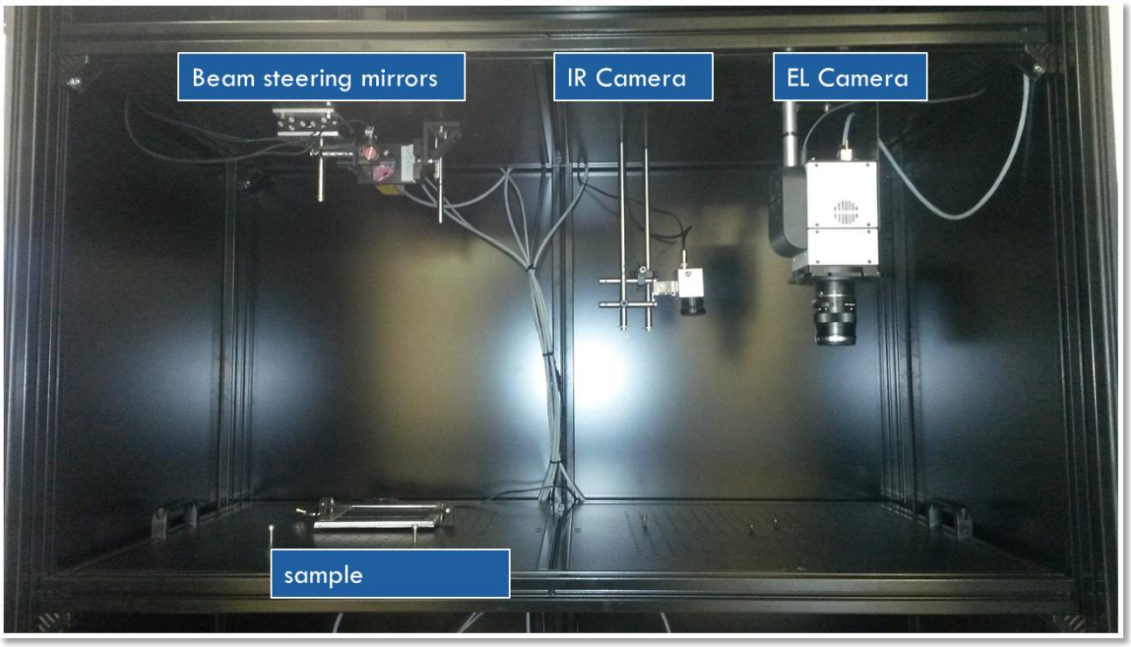

Figure 3-2: Photograph of complete setup.

3.2.2. PV cell holder

Figure 3-3 shows CAD drawings of the cell sample holder. The cell is placed on top of a 5mm Al sheet which acts as the back contact for the cell and in later works it will form part of the temperature control unit. Front contact onto the busbars are done through gold contact at the tip of the arms shown in the figures. The arms have a secondary purpose of pressing the cell onto the back contact. This cell sample holder is designed to handle varying sized cells and is used for the measurements done using the various techniques. The contact arms and the structure was designed and then 3D printed out of PLA (poly lactic acetate). This allowed for design flexibility.

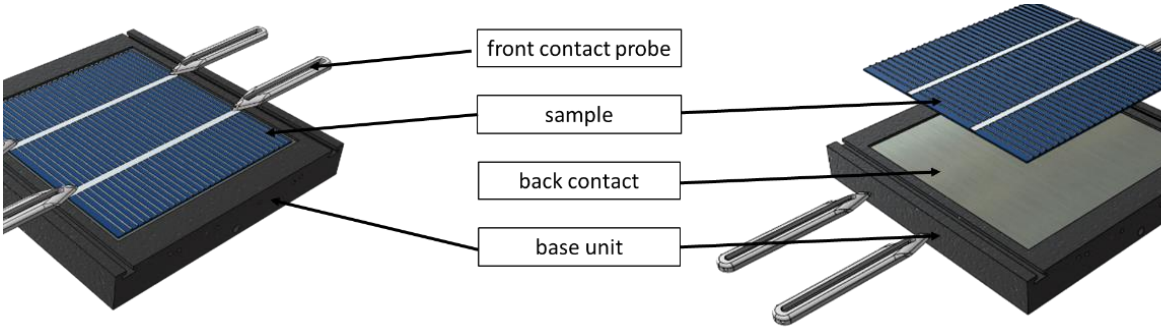

Figure 3-3: PV cell sample holder.

3.3. Equipment details

Figure 3-4 (a) is a photograph of the Sensovation CoolSamba HR-830, the Si CCD camera used for EL in this study. Figure 3-4 (b) is a photograph of the Zeiss Distagon T* 2.8/25 lens, the lens used in conjunction with the EL camera for the EL imaging. Table 3-1 lists the technical specifications of the

EL camera used in all of the EL experiments. The wavelength sensitivity of Si photodetectors is shown in Figure 2-13. Any other information for the camera can be found in reference [42]. Any other information for the lens can be found in reference [43].

(a)

(b)

Figure 3-4: (a) Sensovation CoolSamba HR-830 [42], (b) Zeiss Distagon T* 2.8/25 [43].

Table 3-1: Technical specifications of the Sensovation CoolSamba HR- 830.

Image Sensor Type	Full Frame CCD with on chip micro lenses, ITO transparent gate, low dark current.
Number of Pixels	3326 x 2504
Pixel Size	5.4 µm x 5.4 µm
Wavelength Range	300 – 1150 nm

The filter used within this study was the Edmund Optics 850 nm long pass filter. Figure 3-5 shows the transmission response of the filter used in the EL imaging. The cut-on wavelength is 850nm. The filter cuts out more than 99% of the spectrum with wavelength shorter than 850nm. This minimizes the effect of the stray visible light. The corresponding detected emission from the Si solar cells is within the wavelength range of (900 nm, 1150nm).

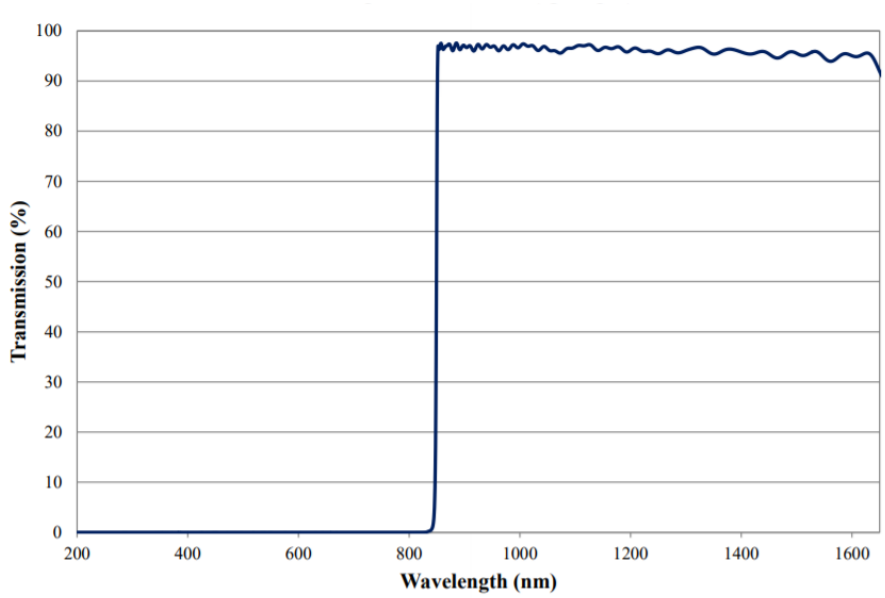

Figure 3-5: Edmund Optics 850 nm long pass filter transmission curve [44].

Figure 3-6 is a photograph of the Optris PI 640, the IR thermal imaging camera used for IR thermography in this study. Table 3-2 lists the technical specifications of the IR thermal camera. Any other information for the camera can be found in reference [45].

Figure 3-6: Optris PI 640 [45].

Table 3-2: Technical specifications of the Optris PI 640 [45].

Image Sensor Type	FPA, uncooled
Number of Pixels	640x480
Pixel Size	5.4 µm x 5.4 µm
Frame Rate	32 Hz, 120Hz (windowing)
Spectral Range	7.5 - 13 µm
Thermal sensitivity	75 mK

Figure 3-7 is a photograph of the Keithley 2450, the source meter unit in this study. The full technical specifications of the unit can be found in reference [46].

Figure 3-7: Photograph of the Keithley 2450 [46].

Figure 3-8 is a photograph of the Coherent Cube Laser 660 nm, the laser probe used in the LBIC measurements in this study.

Table 3-3 lists some of the technical specifications of the laser. Any other information can be found in reference [47].

Figure 3-8: Coherent Cube laser 660 nm [47].

Table 3-3: Technical specifications of the Coherent Cube laser 660 nm [47].

Wavelength	660 nm
Max output power	60 mW
Beam Divergence typical	1.4 mrad
Laser Drive Modes	Digital, Analog and PC Control

Figure 3-9 is a photograph of the small beam diameter scanning galvo mirror system with silver mirrors, the rotational mirrors used in the LBIC measurements in this study. Table 3-4 lists some of the technical specifications of the mirror system. Any other information can be found in reference [48].

Figure 3-9: ThorLabs 2-axis silver coated mirror system [48].

Table 3-4: Technical specifications of the ThorLabs 2-axis silver coated mirror system [48].

Wavelength	500—2000 nm
Maximum scan angle	± 436 mrad
Minimum scan step	15 µrad

Figure 3-10 is a photograph of the scanning lens used in conjunction with the mirror system. Table 3-5 lists some of the technical specifications of the scanning lens. Any other information can be found in reference [49].

Figure 3-10: F-theta scanning lens FTH254-1064 [49].

Table 3-5: Technical specifications of the F-theta scanning lens FTH254-1064 [49].

Effective focal length	254 mm
Scan angle (max)	± 436 mrad
Scan field (max)	156.7 mm x 156.7 mm

Table 3-6 lists some of the technical specifications of the photodiode power meter used in the LBIC measurements in the study to determine the beam intensity. Any other information can be found in reference [50].

Table 3-6: Technical specifications of the Si diode power meter [50].

Detector type	Si photodiode
Maximum power	50 mw
Sensitivity	<1nW
Wavelength range	400-1100 nm

Table 3-7 lists some of the technical specifications of the data acquisition unit used in the LBIC measurements in this project. Any other information can be found in reference [51].

Table 3-7: Technical specifications of the National Instruments ™ DAQ USB 6356 [51].

Maximum single input sample rate	1.25 million samples per second
Input time resolution	10 ns
Input ranges	±1 V, ±2 V, ±5 V, ±10 V
Output time resolution	10 ns
Output ranges	±5 V, ±10 V

Figure 3-11 is a photograph of the pre-amplifier used in the current measurements of the second sample used in the LBIC measurements in this study. Table 3-8 lists some of the technical specifications of the pre-amplifier. Further information can be found in reference [52].

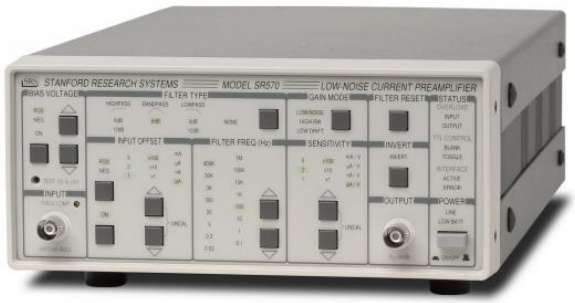

Figure 3-11: SR570 Current Preamplifier [52].

Table 3-8: Technical specifications of the SR570 Current Preamplifier [52].

Maximum input	5 mA
Sensitivity	1 pA/V to 1mA/V in 1-2-5 sequence (Vernier adjustment in 0.5% steps)

3.4. Electroluminescence

3.4.1. Introduction

The theory behind EL imaging and the associated techniques was discussed in Chapter 2. EL imaging was used to identify and characterise various defects within the samples. As shown in Figure 2-13 it is clear that the sensitivity of a Si CCD to the emitted signal from a Si solar cell is minimal; therefore, any stray light in the visible spectrum, would be detrimental to the experimental results. This highlights the importance of the design to ensure the isolation from any stray light. The parameters of the EL setup varied with the size of the sample and the resolution required. That is in the case of this study, the setup was optimized to maximize the resolution of the EL image.

3.4.2. Procedure

The basic procedure for acquiring an EL image is described in Figure 3-12. An unbiased (dark/background) image is acquired and subtracted from the biased image of the cell. This procedure is followed to reduce the effect of background reflections.

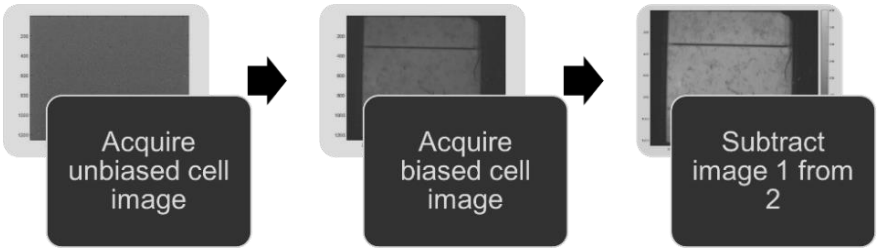

Figure 3-12: EL imaging procedure.

The following procedure was followed to obtain the required EL data for the voltage dependent EL and the voltage dependent reverse bias EL data. The Si CCD camera described above was used to capture EL images. The CCD was cooled to approximately 250K. For both samples, the resulting spatial resolution of each EL image was approximately 4 µm. The Keithley SMU discussed above was used to bias the cell in voltage steps in both the forward and reverse bias while measuring the applied voltage and current. Table 3-9 contains the parameters used for each sample's EL results.

Table 3-9: EL imaging parameters.

EL Parameters:	Sample 1	Sample2
Exposure time (s)	120	30
ReBEL bias range (V)	(-20, 0)	(-14, 0)
ReBEL bias step size (V)	1	0.25
Forward bias range (V)	(0, 1.1)	(0, 0.8)
Forward bias step size (V)	0.1	0.05

The list of the components of the EL imaging system includes:

1. EL camera - Si CCD
2. Camera lens
3. 850 nm long pass filter
4. Keithley 2450 SMU

3.5. IR Thermography

3.5.1. Introduction

IR thermography was used in the identification of shunts and breakdown sites of the samples. The theory behind each IR thermography associated technique is discussed in Chapter 2. The IR thermography setup is optimised for each individual test; depending on resolution required, size of the sample, etc.

3.5.2. Procedure

The basic procedure is described in Figure 3-13. An unbiased (dark/background) image was acquired and subtracted from the biased image of the cell. This procedure was followed to reduce the effect of background reflections and to determine the temperature difference rather than absolute temperature.

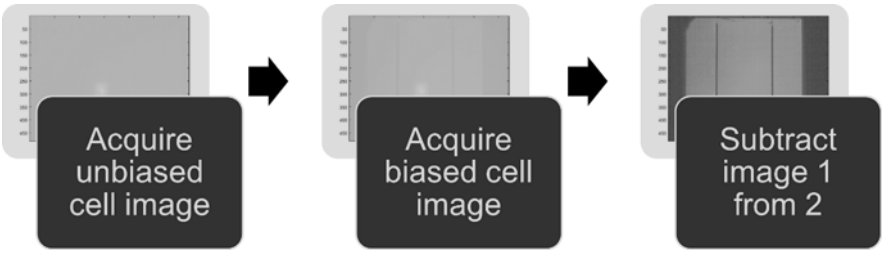

Figure 3-13: IR thermography procedure.

The following procedure was followed in the voltage dependent IR thermal image acquisition. The thermal camera described above was used to capture the thermal images. The Keithley SMU discussed above was used to bias the cell in voltage steps in both the forward and reverse bias while measuring the applied voltage and current. Table 3-10 contains the parameters used for each sample's IR thermography results.

Table 3-10: IR thermography parameters.

EL Parameters:	Sample 1	Sample2
Bias range (V)	(-1, 1)	(-14, 1)
Bias step size (V)	0.25	0.25

The list of the components of the IR thermal imaging system includes:

1. Optris PI 640 thermal camera
2. Keithley 2450 SMU

3.6. Light Beam Induced Current (LBIC) Measurements

3.6.1. Introduction

LBIC was used in the identification of photo-induced current/potential limiting defects within each of the samples. The theory behind the technique is discussed in Chapter 2. The LBIC setup is optimised for each individual test; depending on resolution required, size of the sample, etc.

3.6.2. Setup

Figure 3-14 is an unscaled diagram of the LBIC sub-system. The laser beam's position is controlled via the beam-steering mirrors as shown in the diagram. A custom built LabView™ program is then used to determine the boundaries of the map required and the number of steps of the run to determine the voltages applied to the mirror's controls for the experiment.

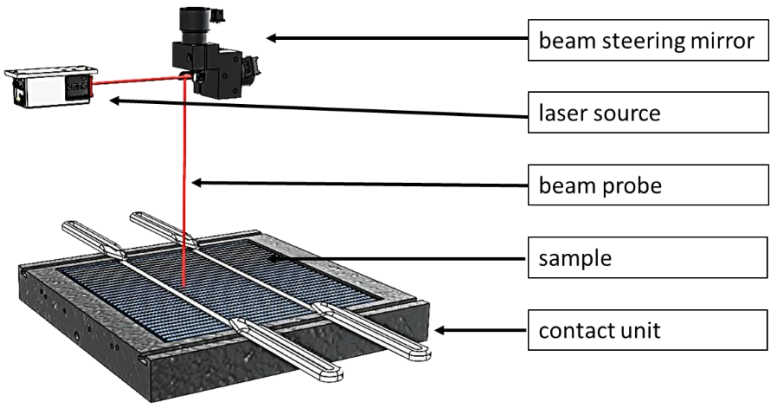

Figure 3-14: LBIC Setup (not to scale).

3.6.3. Procedure

For Sample 1, the following procedure was applied in the LBIC maps. The sample boundaries were of approximately 50 mm x 50 mm with 200 steps in both X and Y dimensions. The calculated step size is 275.0 ± 1.4 µm. A power source unit was used to acquire both the photo-induced current and the photo-induced potential. The size of the laser spot was 550 ± 2.8 µm in diameter with intensity of 1100 ± 22 W/m^2.

For Sample 2, the following procedure was applied in the LBIC maps. The sample boundaries were of approximately 80 mm x 25 mm with 800 and 250 steps in the corresponding directions respectively. This gives an approximate step size of 105.0 ± 1.3 µm. A National Instruments ™ DAQ USBX 6008 was used to acquire the photo-induced potential signal. A Stanford S570 pre-amplifier was used in conjunction with the National Instruments™ DAQ USB 6356 to acquire the photo-induced current. The approximate size of the laser spot was 314.9 ± 3.9 µm in diameter with intensity of 1300 ± 26 W/m^2.

The list of the components of the LBIC measurement system includes:

1. Coherent Cube Laser 660nm
2. ThorLabs 2D small beam galvo system with silver-coated mirrors
3. ThorLabs F-Theta Scan Lenses
4. ThorLabs compact USB Power Meter
5. Keithley 2450 SMU
6. National Instruments™ DAQ USB 6356
7. A Stanford S570 pre-amplifier

3.7. Dark Current-Voltage (I-V) data and Parameter Optimization

The Dark I-V system was included as part of the setup and used to determine the dark I-V characteristics of each sample. Application of the GAPO to voltage dependent EL and LBIC data for local I-V characterisation was out of the scope of the study. A source meter unit was used to measure the I-V response of each sample. The Genetic Algorithm for Parameter Optimisation (GAPO) was then applied to the data acquired to extract the various parameters associated with the model used to describe the I-V relation.

The GAPO was applied to the corresponding dark I-V data, with population size of 100, maximum iteration number of 100 and mutation rate of 50%. The iteration number and population size were kept to a minimum to limit computational time. The minimum error was set to 0.001%. The GA went through 100 independent runs itself, to apply statistical analysis to the parameters extracted from the data. The parameters extracted in each independent result is the fittest individual from each final iteration.

3.8. Summary

A PV cell can be characterised by a set of non-destructive tests. The I-V characteristic curve is obtained experimentally using a SMU. The Genetic Algorithm for Parameter Optimisation (extraction) can be used to extract the parameters of the applied model from the I-V curves. LBIC

measurements are utilised to locally measure the photo-induced current and potential of a PV cell. This allows for the identification of performance limiting defects. EL imaging and its associated techniques are used in the identification of recombination limiting defects, micro-cracking, as well as the imaging of electrical breakdown of the device. IR thermography is used for the identification of hot-spots that are caused by shunts and breakdown sites. By comparing the results of all of the techniques used in this study, the defects can be more accurately identified.

4. Results and Discussion

4.1. Introduction

The experimental system and techniques discussed in Chapter 3 were used to investigate the device and material properties of Si solar cells. Although several samples were used to both test and develop the experimental setup, this chapter presents detailed results and analysis on two samples. The samples that are presented here were selected based upon the presence and extent of various material and device related defects. The samples illustrate the value of each technique employed.

For each sample, the results of the applied techniques will first be introduced individually. The results are discussed in greater detail when the results are compared, so as to draw the appropriate conclusions.

i) Sample 1: Mechanically scribed 55 mm x 55 mm multi-crystalline silicon (m-c Si) PV cell.Sample 1 is a partial sample of a m-c Si PV cell It was cleaved into 55 mm x 55 mm. Figure 4-1 shows a photograph of sample 1 and indicates the manufactured edges as well as the cleaved edges.

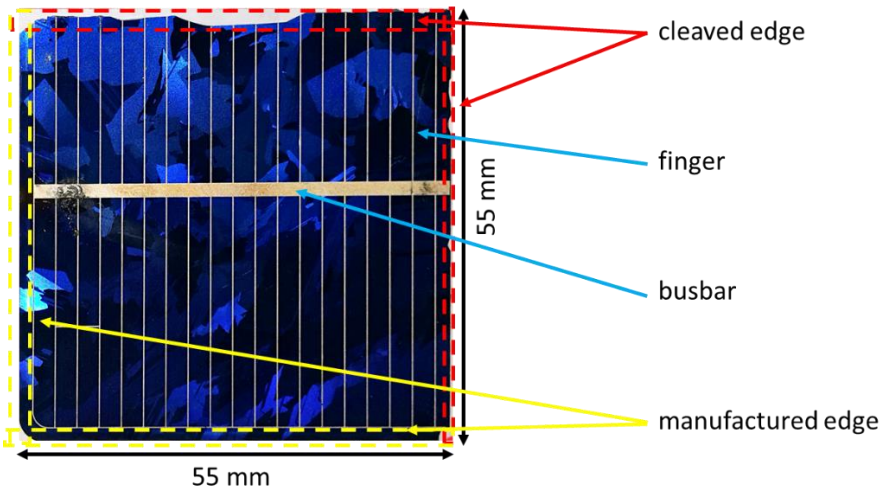

Figure 4-1: Photograph of sample 1.

ii) Sample 2: Laser cut 80 mm x 25 mm m-c Si PV cell. Sample 2 is a partial sample of a m-c Si PV cell It was laser cut into an 80mm x 25 mm sample. Figure 4-2 shows a photograph of sample 2 and indicates the manufactured edges as well as the laser cut edges.

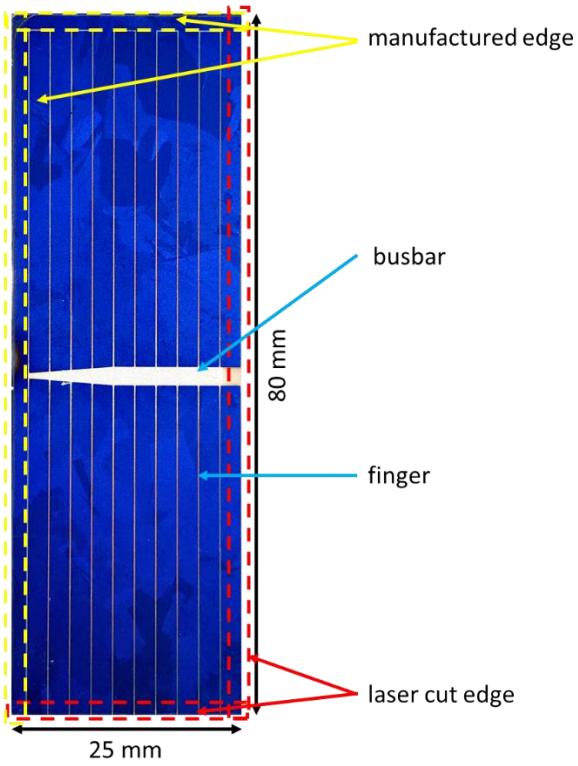

Figure 4-2: Photograph of sample 2.

As discussed in Chapter 3, the techniques, in various modes, applied to the samples are: dark I-V characteristic curve measurements, LBIC, EL and IR thermography.

4.2. Results of Sample 1

4.2.1. Dark I-V curve

Figure 4-3 shows the dark I-V curve of Sample 1 in forward bias together with the modelled data using the GAPO. The modelled data was calculated using the mean value of the parameters shown in Table 4-1. The dark I-V data used in the plot is that of the validation set. The overall fit is depicted by the red curve and labelled Model in the graph. The current contribution of two different terms of the model are also shown and labelled Diode 1 and 2. The third contribution is shown and labelled Shunt. These refer to the terms in equation 2-14, viz. the current through D_1, D_2 and R_{SH} as depicted in Figure 2-12. The equation is repeated here for clarity. The line indicating the current of Diode 1 is difficult to distinguish from the line indicating the overall model. This is due to the fact the Diode 1 is the main current contributor. Both the Shunt line and the Diode 2 line are also difficult to differentiate, both provide minimal current to the overall model.

$$I = I_{01}\left[\exp\left(\frac{q(V-IR_{SE})}{n_1 k_B T}\right)-1\right] + I_{02}\left[\exp\left(\frac{q(V-IR_{SE})}{n_2 k_B T}\right)-1\right] + \frac{(V-IR_{SE})}{R_{SH}} \quad \text{----(4-1)}$$

where the symbols are as previously defined.

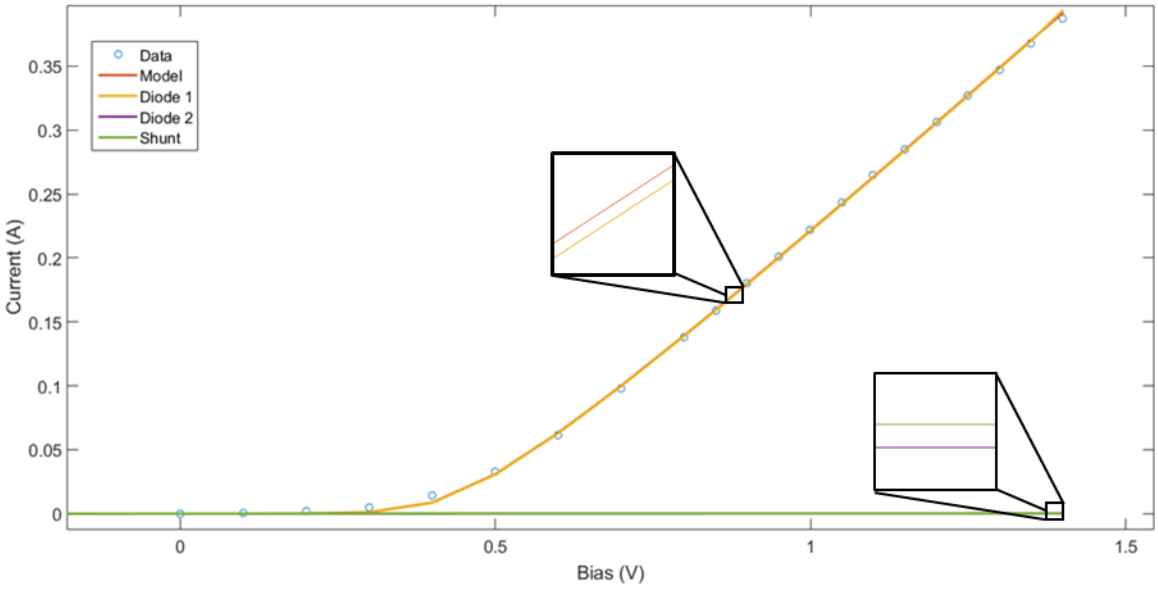

Figure 4-3: I-V characteristic curve of Sample 1. The fit of the optimised model compared to the measured I-V data is shown as well as the contributions made by Diode 1, Diode 2 and the Shunt resistance term.

Table 4-1 shows a summarized list of the various parameters of the applied model obtained in the optimisation process. The GAPO was run 100 times, the mean and standard deviation were determined from the set of results obtained. The variation in the parameters of the second diode has a greater relative standard deviation when compared to the other diode, implying that Diode 2 is the less significant diode. The current of Diode 2 is related to edge defects and induced defects associated with the diamond scribing process [18]. The standard deviation of the shunt resistance term is greater than 1000X of the mean value for the shunt resistance. This implies that the shunt current is too small to have an impact on the model as illustrated by the green line. Furthermore, in the case of this sample the shunt term appears to be irrelevant, implying that, at least in terms of current losses through shunting, this sample is of high quality. Relative standard deviation is calculated as the ratio between the standard deviation of the parameter and its mean value. The significance of each term can be inferred from the relative standard deviation of the parameters that govern it as the greater the deviation implies that the model is less sensitive to the parameter value. This is possible due to the fact that each independent run of the GA is a good fit.

Figure 4-4 shows the result of the application of the GAPO on the extended dark I-V data of Sample 1. The figure, again, compares the data to the overall fit of the model applied, as well as the current contribution of the various terms of the model. The line indicating the current of Diode 1 is difficult to distinguish from the line indicating the overall model, this is due to the fact Diode 1 is the main current contributor to the applied model. However, in reverse bias it is possible to distinguish the current contribution of the shunt line and the second diode.

Table 4-1: Statistical analysis of optimised parameters of the mechanically scribed sample.

Parameter	Mean	Standard Deviation	Relative Standard Deviation
I_{01} (A)	5.213×10^{-7}	2.980×10^{-14}	5.716×10^{-8}
I_{02} (A)	5.041×10^{-7}	4.082×10^{-14}	8.098×10^{-8}
n_1	1.553	3.902×10^{-3}	2.513×10^{-3}
n_2	3.484	0.964	0.2760
R_{SE} (Ω)	1.820	0.166×10^{-3}	9.121×10^{-5}
R_{SH} (Ω)	1.835×10^{3}	4.294×10^{6}	2340

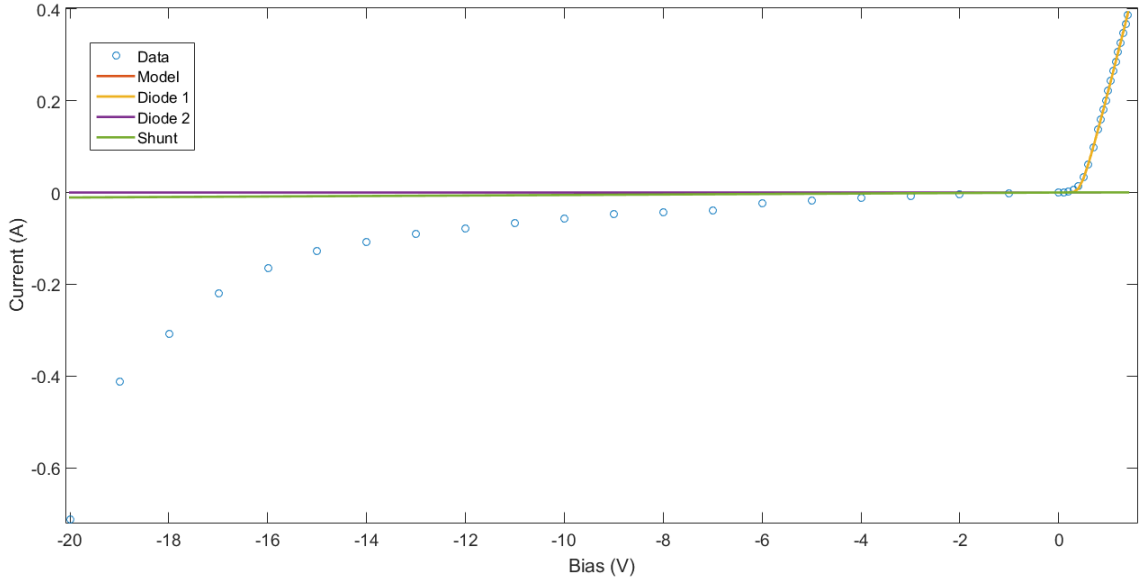

Figure 4-4: The extended I-V curve of Sample 1, with the corresponding contributions of the terms in the applied model.

Figure 4-4 highlights the inadequacy of the application of the optimised values from the forward bias to reverse bias. The shunt current makes a minimal contribution to the reverse current. This implies that the applied model needs further refinement. The applied model will need to consider the various mechanisms that occur in the reverse bias. Some of these mechanisms have been noted previously (Section 2.1.4.2). The reverse breakdown related results presented below give an indication of the spatial distribution of the current flow as well as the magnitude of the current within this sample. The modelling of the reverse I-V curve was not studied further.

4.2.2. LBIC map

Figure 4-5 (a) shows the map of the photo-induced potential (or open circuit voltage, V_{OC}) of Sample 1 and (b) the photo-induced current (or short circuit current, I_{SC}). In both maps, it is possible to

distinguish (1) the busbar, (2) the “fingers”, (3) a micro-crack and various other crystal structure defects such as grain boundaries.

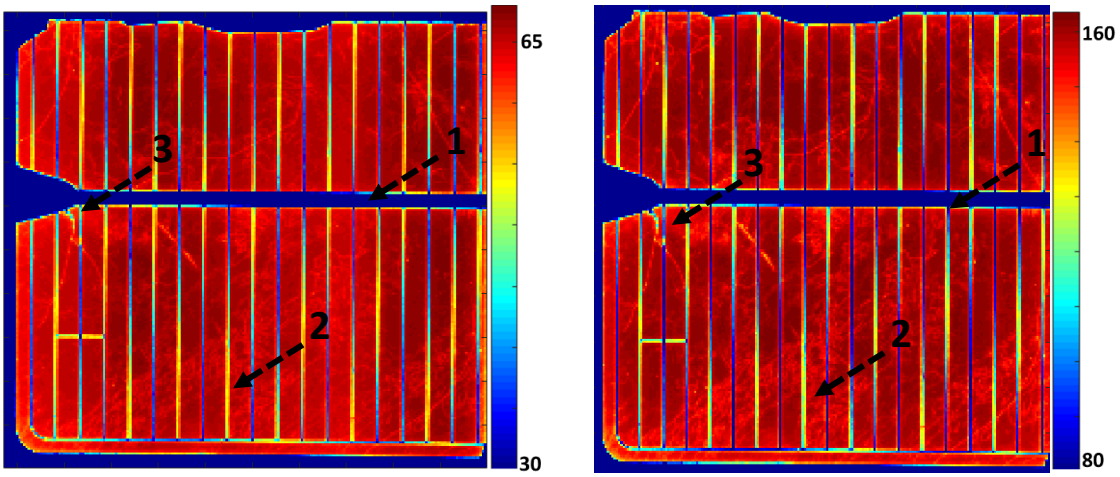

(a) (b)

Figure 4-5: (a) V_{OC} map (mV), (b) I_{SC} map (μA).

4.2.3. Forward EL image

Figure 4-6 shows the forward bias (0.8 V) EL intensity image of the first sample. In the image, it is possible to distinguish (1) the busbar, (2) the “fingers”, (3) micro-cracks, (4) effect of the back-contact, and various other crystal structure features.

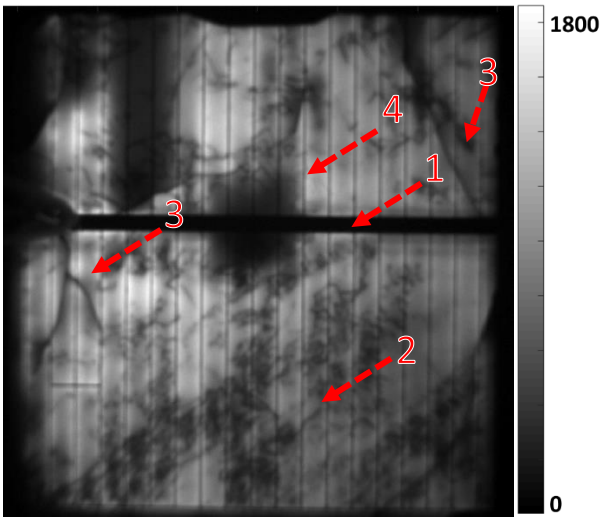

Figure 4-6: Forward bias EL intensity image at 0.8 V (counts).

4.2.4. ReBEL EL image

Figure 4-7 shows the intensity images of the first sample at (a) -5 V, (b) -14 V and (c) -20 V. Various breakdown sites are visible in the images; (1) and (2) are pre-breakdown sites as they are visible at

-5 V, (3) and (4) are breakdown sites visible at -20 V implying that they are either related to tunnelling or avalanche breakdown (AB). Emission-voltage curve analysis is required to determine the type of breakdown, as discussed below.

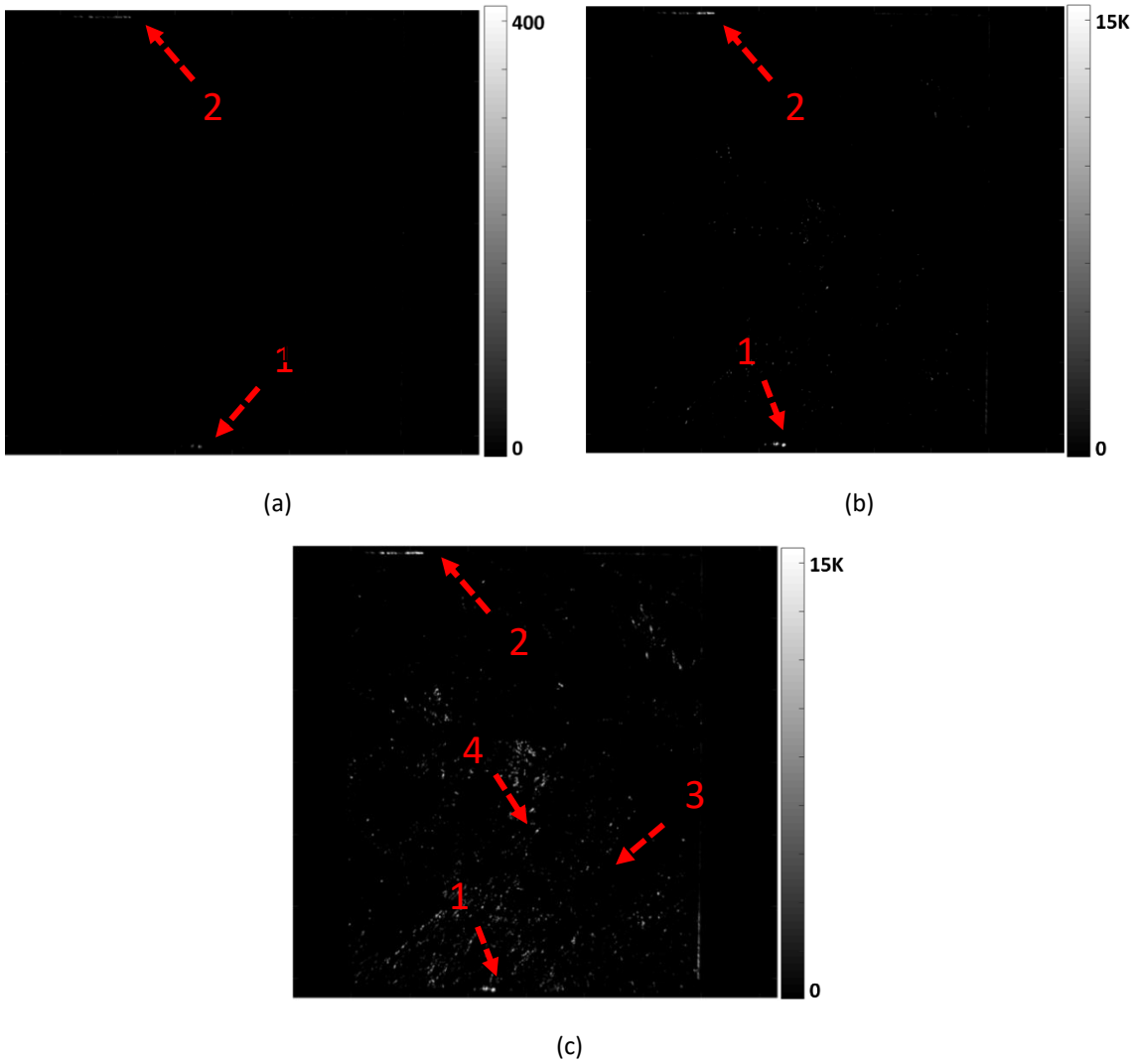

Figure 4-7: ReBEL intensity image (counts) at (a) -5 V, (b) -14 V, (c) -20 V.

4.2.5. Emission-voltage curves of specific interesting points

The numbering of the positions in this section is the same as above. The breakdown is highly localised; the emission-voltage curves of 'pixel' diodes numbered above is shown below. It is assumed that the emission response is a direct indication of the localised current through the breakdown site. Therefore, the emission-voltage curve is indicative of the current-voltage response. The quantum efficiency of the optics and sensor are not considered; however, as it is only used as an indicative measure. Therefore, the assumption is sensible.

Figure 4-8 (a) shows the emission-voltage curve of position 1. The emission of this "pixel" diode is detectable at -5 V which is typical of a pre-breakdown site. The emission-voltage response is

exponential in nature; assuming the I-V response is similar, this breakdown is related to the Zener effect due to a highly doped p-n junction due to the presence of an Al stain [21]. However, it is still possible that a weak ohmic shunt (ohmic tunnel junction) can emit light through the formation of high electric fields [25]. At -12 V the emission-voltage curve begins to flatten off. Figure 4.8 (b) shows the corresponding ReBEL image at -5 V, this indicates the shape and position of the breakdown site. A plausible explanation of the flattening curve is the saturation of the mechanisms that cause light emission. Figure 4-8 (c) shows the corresponding EL image at 0.8 V. The EL image contains no visible features.

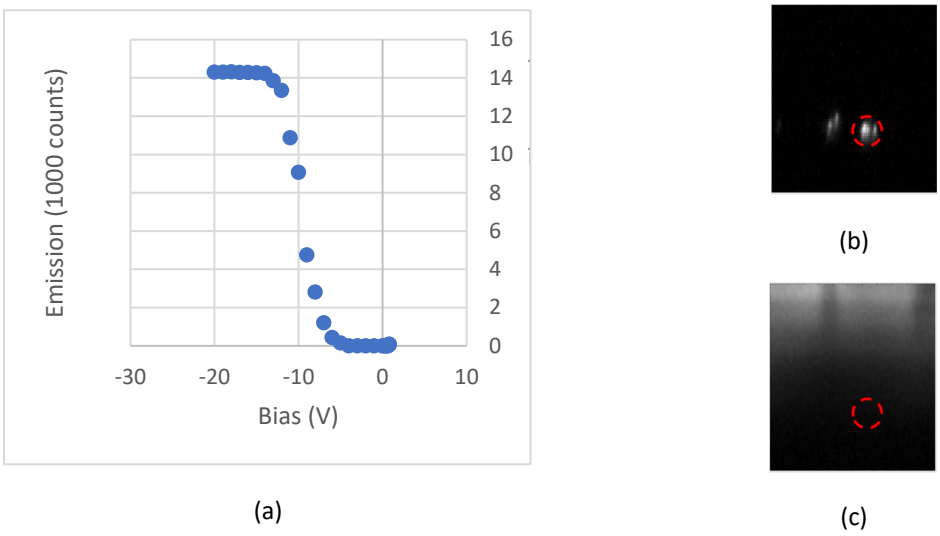

Figure 4-8: Position 1 (a) emission-voltage curve, (b) ReBEL image at -5 V, (c) EL image at 0.8 V.

Figure 4-9 (a) shows the emission-voltage curve of position 2. The emission from this “pixel” diode is detectable at -5 V which is typical of a pre-breakdown site. The emission-voltage response is exponential in nature; assuming the I-V response is similar, this breakdown is related to the Zener effect due to a highly doped p-n junction due to the presence of an Al stain [25]. However, it is still possible that a weak ohmic shunt (ohmic tunnel junction) can emit light through the formation of high electric fields [25]. The site is present at the diamond scribed edge, it is possible that the scribing process converted the crystalline Si to amorphous Si, this would have introduced a number of gap states at the local junction [25]. At -15 V the emission-voltage curve’s gradient decreases. This deviation from the exponential relation was not investigated. Figure 4-9 (b) shows the corresponding ReBEL image at -5 V showing the shape and position of the breakdown site. Figure 4-9 (c) shows the corresponding EL image at 0.8 V. The EL image contains no visible feature.

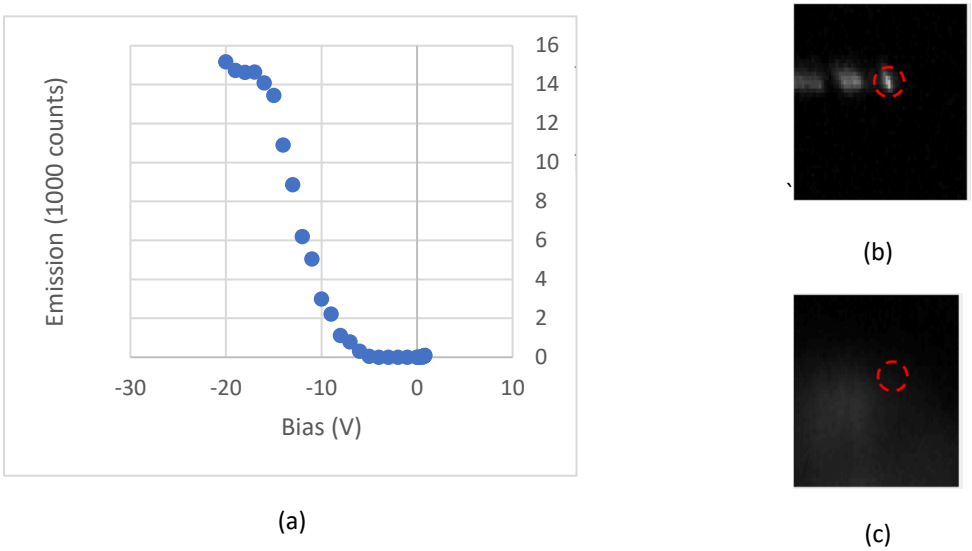

Figure 4-9: Position 2 (a) emission-voltage curve, (b) ReBEL image at -5 V, (c) EL image at 0.8 V.

Figure 4-10 (a) shows the emission-voltage curve of position 3. The emission of this "pixel" diode is detectable at -12 V which is typical of a type II or type III breakdown site [21]. However, the hard response of the emission-voltage curve and linear response after breakdown indicates that it is more likely AB [21]. At biases more negative than -15 V the gradient of the curve decreases, a plausible explanation is the increase in effective series resistance due to the distributed nature of the material resistance. Another plausible explanation of this feature is that the non-radiative mechanisms are becoming more dominant. Figure 4-10 (b) shows the corresponding ReBEL image at -14 V, this indicates the shape and position of the breakdown site. Figure 4-10 (c) shows the corresponding EL image at 0.8 V. It is apparent that the breakdown site is part of some visible feature in the EL image.

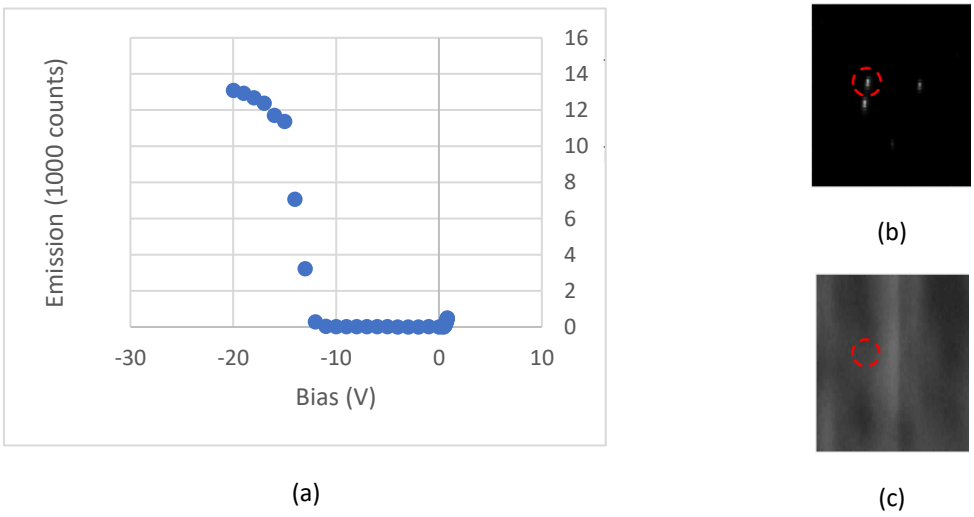

Figure 4-10 Position 3 (a) emission-voltage curve, (b) ReBEL image at -14 V, (c) EL image at 0.8 V

Figure 4-11 (a) shows the emission-voltage curve of position 4. This "pixel" diode emits at -20 V, this voltage is indicative of a type III breakdown site, that is AB [21]. Figure 4-11 (b) shows the

corresponding ReBEL image at -20 V, this indicates the shape and position of the breakdown site. Figure 4-11 (c) shows the corresponding EL image at 0.8 V.

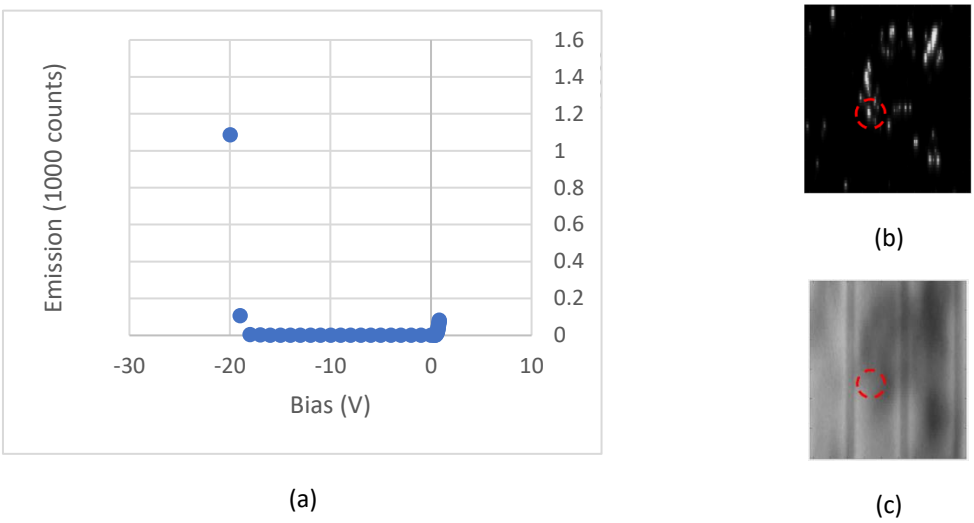

Figure 4-11 Position 4 (a) emission-voltage curve, (b) ReBEL image at -20 V, (c) EL image at 0.8 V

4.2.6. Series Resistance Map

Figure 4-12 shows the series resistance map generated from voltage dependent EL, by the method developed by Hinken et al [30]. Feature (1) is the busbar, the calculated resistance is noisy over the busbar; this is due to the fact that the applied technique is not applicable to the busbar data. Similarly, the technique does not apply to the data from the fingers (2). The micro-crack (3) either shows an increased series resistance or the crack is described by a different model than the one applied in the technique - it is assumed that the ideality of each diode is 1. The region indicated (4) contains crystal structure defects as indicated above in the EL intensity image, the region also appears to have an overall higher series resistance. The series resistance between the fingers (5) also varies. The series resistance goes from its lowest right next to the finger to its highest in the middles between the fingers. The regions similar to (6), show a higher series resistance to that of the remainder of the cell. The series resistance in these regions appears extremely noisy, the EL signal from the same regions (as seen in Figure 4-6) are lower than the surrounding areas. It is possible that a greater portion of recombination in these regions is occurring due to defect states and therefore fall outside of the sensitivity of the Si CCD used to acquire the images. Therefore, the emission detected will not be useful in the determination of the series resistance due to lack of information of recombination through defect mechanisms.

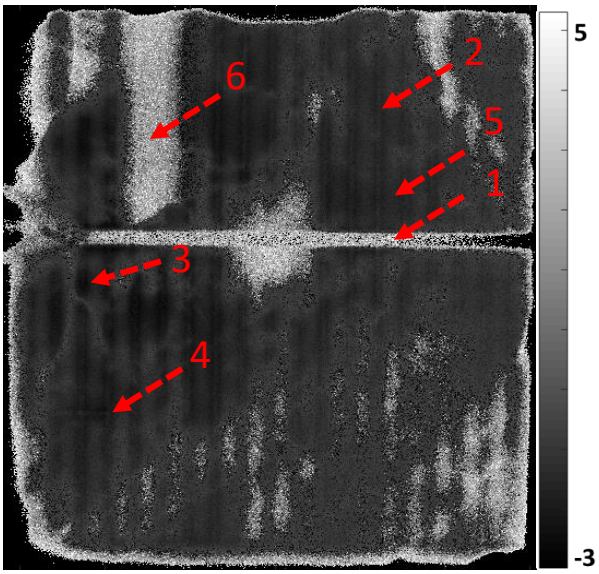

Figure 4-12: Series resistance map of the first sample (arbitrary logarithmic units).

4.2.7. Breakdown Voltage Map

For Figure 4-13 it was assumed that any count greater than 100 counts was well above the noise of the background and is therefore the start of reverse bias breakdown. Using the voltage dependent ReBEL data, it is possible to map the breakdown voltage of the different breakdown sites of the cell. Figure 4-13 shows a map of the breakdown voltage of the cell; comparing this to Figure 4-7 (a), (b) and (c), it can be seen that there is a large number of breakdown sites of low breakdown emission intensity (low breakdown current). There appears to be low current breakdown emission across the busbar. Upon further analysis, it was observed that the busbar was pitted. Allowing for breakdown emission to be visible from the area.

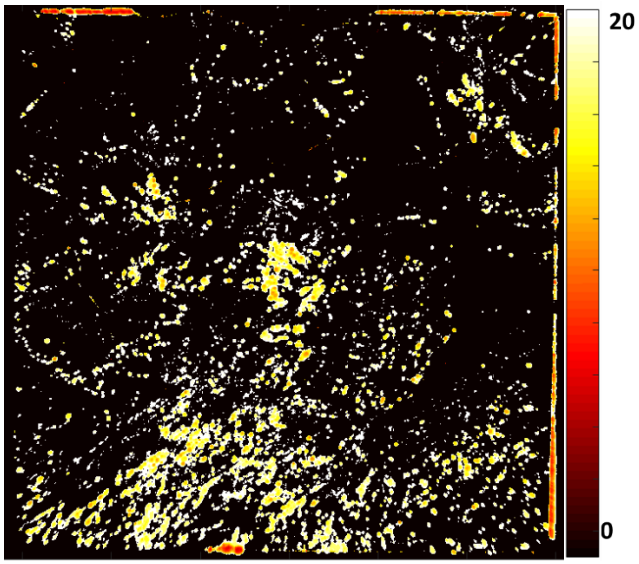

Figure 4-13: Breakdown voltage map (-V).

Figure 4-14 is a microscope image of the pits formed in the busbar - indicated by red circles. The pits can allow for the escape of the breakdown emission through the busbar. Figure 4-15 (a) is a microscope image of a particular edge pit on the busbar that is indicated in Figure 4-15 (b).

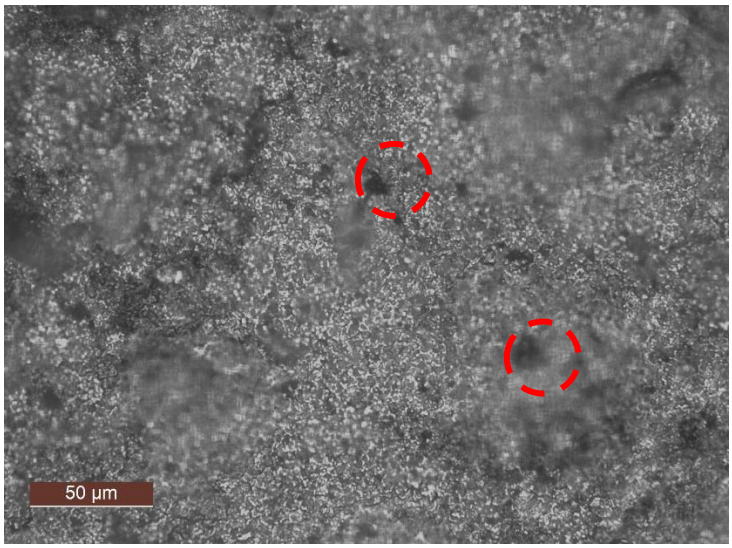

Figure 4-14: Sites of pitting on the busbar of Sample 1.

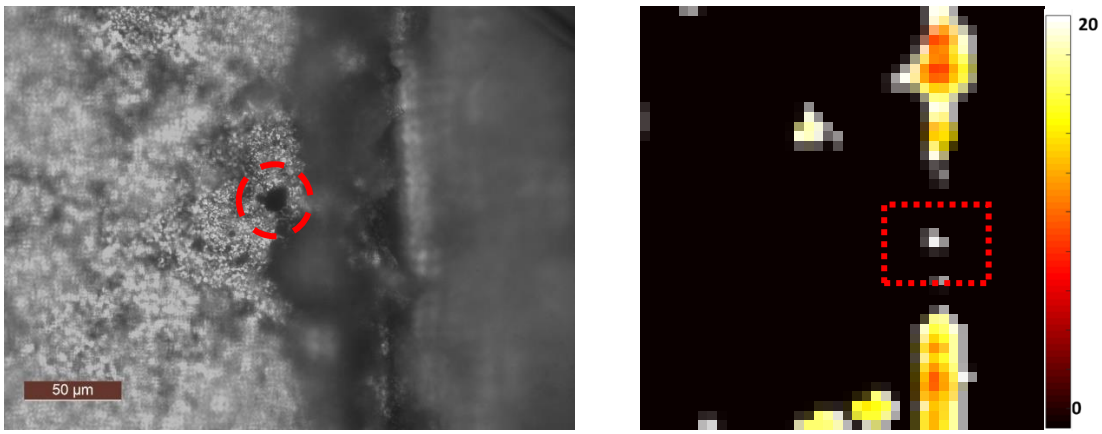

(a) (b)

Figure 4-15: (a) Large pit in busbar corresponding to breakdown site, (b) breakdown voltage map of the breakdown site.

Figure 4-16 is a microscope image indicating the damage associated with the scribing process on the edge of Sample 1. The process induced low voltage emitting breakdown sites along the damaged edge. The process likely induced local defect states and/or the local conversion of crystalline Si to amorphous Si [25].

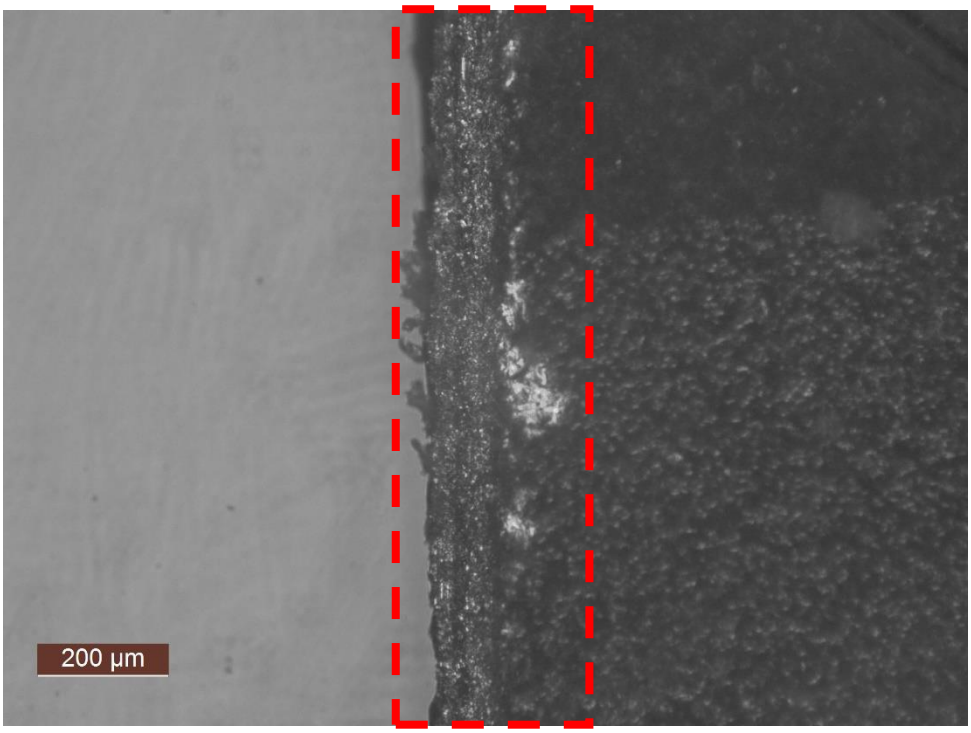

Figure 4-16: Scribed section of cell, indicating material damage

4.2.8. Comparisons of the results of Sample 1

4.2.8.1. LBIC I_{SC} map compared to the forward EL

Figure 4-17 shows the comparison between the (a) forward bias EL image at 0.8 V and the (b) LBIC I_{SC} map. Feature (1) is an example of a micro-crack that reduces both band-to-band radiative recombination and photo-current collection efficiency. Feature (2) is an example of low angle grain boundaries, limiting band-to-band radiative recombination. The decrease in photo-current collection efficiency is likely due to decrease in the generated current or current lost due to shunting through the gettered defect states. Feature (3) is a possible example of near-sub-surface grain boundary which limits radiative recombination through non-radiative recombination or shunts. As the red laser penetrates deep into the material; the short circuit map cannot distinguish grain boundaries approximately parallel to the cell surface. In future work, using multiple wavelengths with varying penetration depths will be used to determine the exact nature of such defects. Feature (4) is an example of the back contact, it limited band-to-band radiative recombination; however, it has not limited the short circuit current of the sample. Similarly, in future works, multiple wavelengths will be used to determine the exact collection efficiency properties of such defects. Wavelength dependent EL will also be used to determine the emission spectral responses of defects such as (3) and (4), which will lead to improved characterisation of such defects.

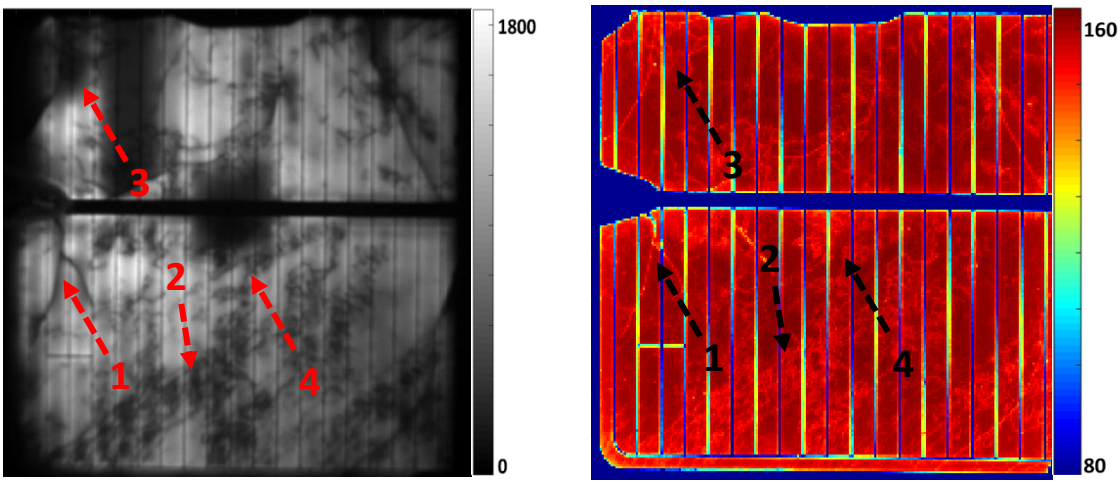

(a) (b)

Figure 4-17: Comparison of (a) EL image at 0.8 V (counts), (b) I_{SC} map (µA).

4.2.8.2. Forward EL compared to series resistance map

Figure 4-18 shows the comparison between the (a) forward bias EL at 0.8 V and the (b) series resistance map. Feature (1) is a micro-crack which shows a decreased band-to-band radiative recombination due to the increase in the series resistance to the emitter in the region. Otherwise, the decrease in band-to-band radiative recombination is due to the increase of alternate recombination mechanisms (non-radiative or defect related recombination) which would then imply that the increased calculated series resistance is simply an artefact of the applied technique. Features (2), (3) and (4) show low band-to-band radiative recombination and correspond to a noisy region with increased series resistance; this could similarly be an artefact related to the technique. Feature 5 is an example of a decrease in EL signal as the distance from the finger increases - this is due to the increase of effective series resistance.

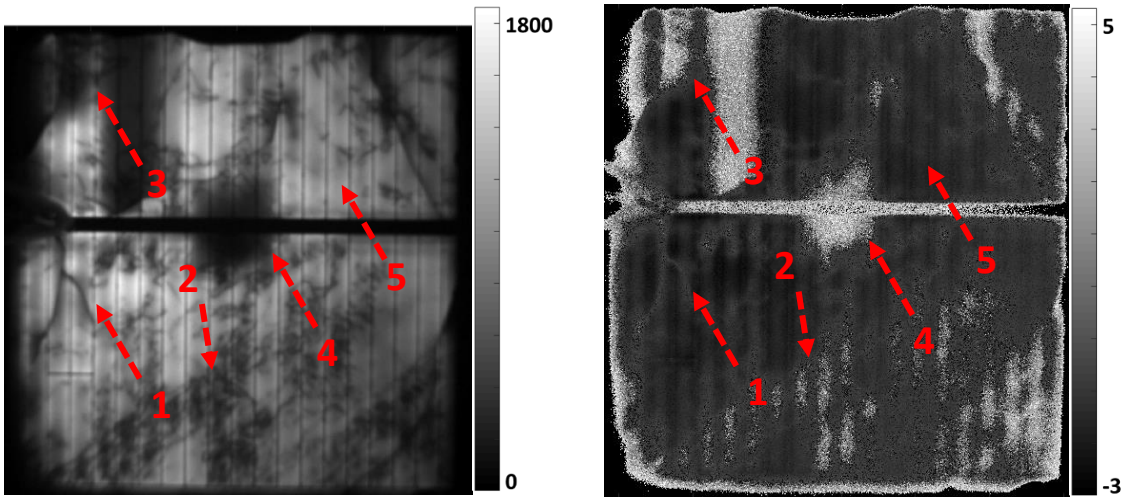

(a) (b)

Figure 4-18: Comparison of (a) EL image at 0.8 V (counts), (b) series resistance map (arbitrary logarithmic units).

4.2.8.3. Comparison of LBIC I_{SC}, photograph, breakdown voltage map and forward EL

Figure 4-19 shows a comparison between the various features present in the (a) LBIC I_{SC} map, (b) photograph with the breakdown voltage as an overlay and (c) the forward bias EL image at 0.8 V. The colour scale is that of the corresponding figures above. In Figure 4-19 (b), breakdown with low breakdown voltage is noticeable in regions (1), (2) and (3). These correspond to the edges scribed to cut the cell. The corresponding regions in the EL image show decreased band-to-band radiative recombination. This is either due to the smearing of the metal of the contacts into the material of the device or the scribing process changed the crystalline structure in the localised region into amorphous Si. For either possibility, gap states will be introduced into the local band structure, this can lead to the formation of an ohmic shunt through trap assisted tunnelling (as shown in Figure 2-5). ReBEL emission will then be related to intra-band thermalisation. In region (4), the feature visible is indicated to have a low breakdown voltage. The location on the device, shape and the low breakdown voltage of the feature implies that it could be an MIS (metal insulator semiconductor) junction formed on the surface by the presence of an Al precipitate [22], techniques such as energy dispersive spectroscopy (EDS) would be required to confirm this. The feature visible in region 5, is positioned directly over one of the square back contacts. The decreased signal is indicative of decreased band-to-band radiative recombination. The region also contains features in the I_{sc} that shows decreased efficiency at gettered defects at grain boundaries. The breakdown voltage overlay indicates voltages that correspond to type II breakdown. This breakdown type is associated with IFE (internal field emission) [26] or the thermionic emission from a Schottky shunt from $FeSi_2$ needles [25].

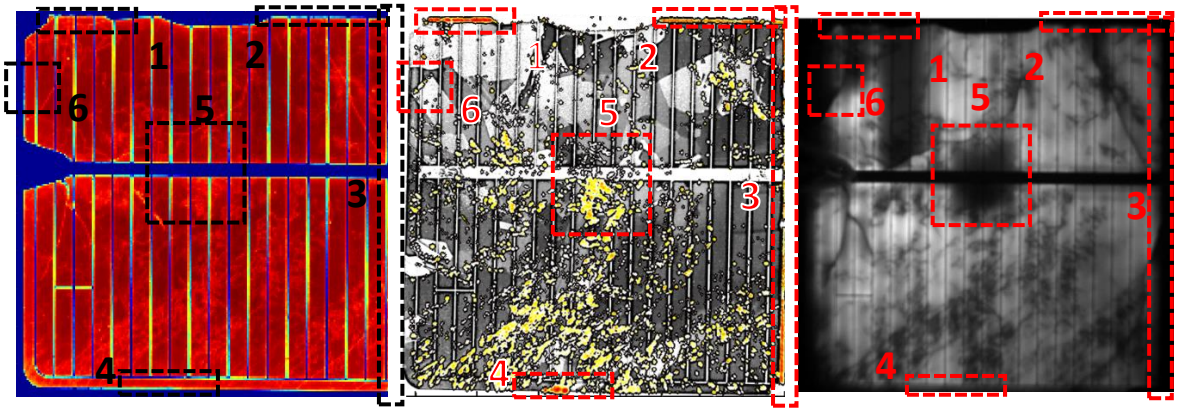

(a) (b) (c)

Figure 4-19: (a) LBIC I_{sc} map, (b) photograph with breakdown voltage map overlay, (c) forward bias EL image at 0.8 V, colour scheme is that of the above samples.

4.2.9. Potential induced shunt

Figure 4-20 shows a comparison of forward bias EL (a) pre-induced shunt and (b) post-induced shunt and the corresponding I-V curves – (c) and (d). Overall, the induced shunt did not affect the visible features in EL image. However, the EL intensity is drastically decreased. This is due to the preferential pathway for the current. This is confirmed by comparing the I-V curve (c) pre-induced shunt and (d) post-induced shunt. The post-induced shunt I-V curve highlights the preferential current flow through the induced shunt. Table 4-2 summarises the optimised parameters of the scribed sample post-induced shunt. This analysis was done to highlight the severity of the induced shunt. The mean shunt value (see Table 4-1) went from 1.835 kΩ to 1.284 Ω. The standard deviation of the shunt value went from greater than 10000% down to less than 0.8%. That is, the shunt term became a significant term within the model.

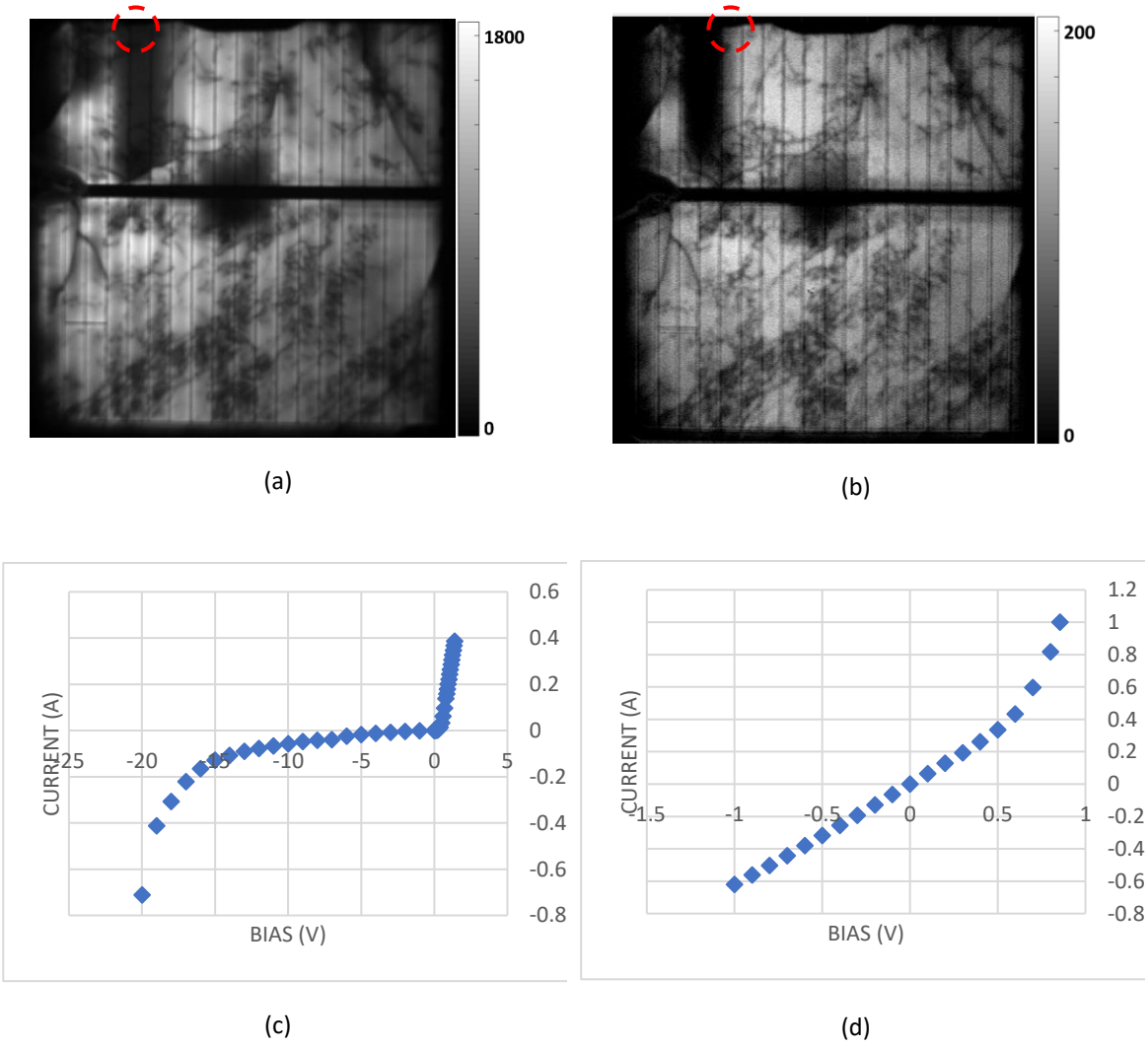

Figure 4-20: (a) Pre-induced shunt forward bias EL at 0.8 V (counts), (b) post-induced shunt forward bias EL at 0.8 V (counts), (c) pre-induced shunt I-V curve, (d) post-induced shunt I-V curve.

Table 4-2: Statistical analysis of optimised parameters of the scribed sample post-induced shunt.

Parameter	**Mean**	**Standard Deviation**	**Relative Standard Deviation**
I_{01} (A)	4.054×10^{-7}	4.976×10^{-14}	1.227×10^{-7}
I_{02} (A)	4.987×10^{-7}	4.378×10^{-14}	0.779×10^{-8}
n_1	1.776	0.024	1.351×10^{-2}
n_2	3.579	0.886	0.248
R_{SE} (Ω)	0.233	0.011	0.047
R_{SH} (Ω)	1.284	1.010×10^{-2}	0.008

Figure 4-21 shows a comparison between the IR thermal image of the shunted region of the sample at (a) at -1V and (b) at 1 V. The thermal response is linear in nature, indicating the shunt is ohmic in

nature. This linear response in the post-induced shunt I-V curve confirms this. The shunt was formed at -24 V and its position is under a finger.

(a)

(b)

Figure 4-21: IR thermal image of the shunted region of the sample at (a) at -1V and (b) at 1 V.

4.2.10. Summary of Sample 1 Results

The results obtained for Sample 1 contains defects and properties that illustrate the strengths and failings of the various techniques employed. As the sample is m-c Si, grain boundaries can be noted in techniques such as LBIC and EL imaging. The gettered defects cause shunting and defect levels decreasing efficiency and band-to-band recombination. The reverse current noted in the dark I-V curve was explained by the various breakdown types distributed across the sample as noted in the ReBEL intensity images. The scribing process induced defects/converted the crystalline Si into amorphous Si along scribe lines which can be noted in the reverse portion dark I-V curve as well as the breakdown related results. Before the induced shunt, the standard deviation of the shunt resistance term indicates that the shunt current did not affect the performance of the cell. It also indicated that thr scribing process did not induce ohmic shunts along the edge; it in fact induced the defects related to low reverse bias breakdown. The induced breakdown sites are likely due to the smearing of the metal and other contaminants into the material. The high potential used in the experimental process (-24 V) induced a shunt into the device. The IR thermal images indicated that a single shunt was induced and that it was ohmic in nature.

4.3. Results of Sample 2

4.3.1. Dark I-V curve

Figure 4-22 shows the dark I-V curve of Sample 2 in forward bias together with the modelled data using the GAPO. The dark I-V data used in the plot is that of the validation set. The overall fit is depicted by the red curve and labelled Model in the graph. The current contribution of two different diode terms of the model are also shown and labelled Diode 1 and 2. The third contribution shown is that due to the shunt current. The line representing the data is difficult to distinguish from the line indicating the overall model, this indicates a good fit. In the range of (-1 V, 0.4 V) it is difficult to differentiate between the lines representing the Shunt, overall model and data. However, upon close inspection it is possible to distinguish between the Shunt line and the Data line in the range of (-1 V, -0.8 V), and that is a result of a non-linear reverse current through breakdown mechanisms. Table 4-3 is a summarised list of the various parameters of the applied model obtained in the optimization process. The variation in the parameters of the second diode has a greater relative standard deviation when compared to the remainder of the parameters, implying that the term is the least significant in the model. The significance of each term can be inferred from the relative standard deviation of the parameters that govern it as the greater the deviation implies that the model is less sensitive to the parameter value. This is possible due to the fact that each independent run of the GA is a good fit.

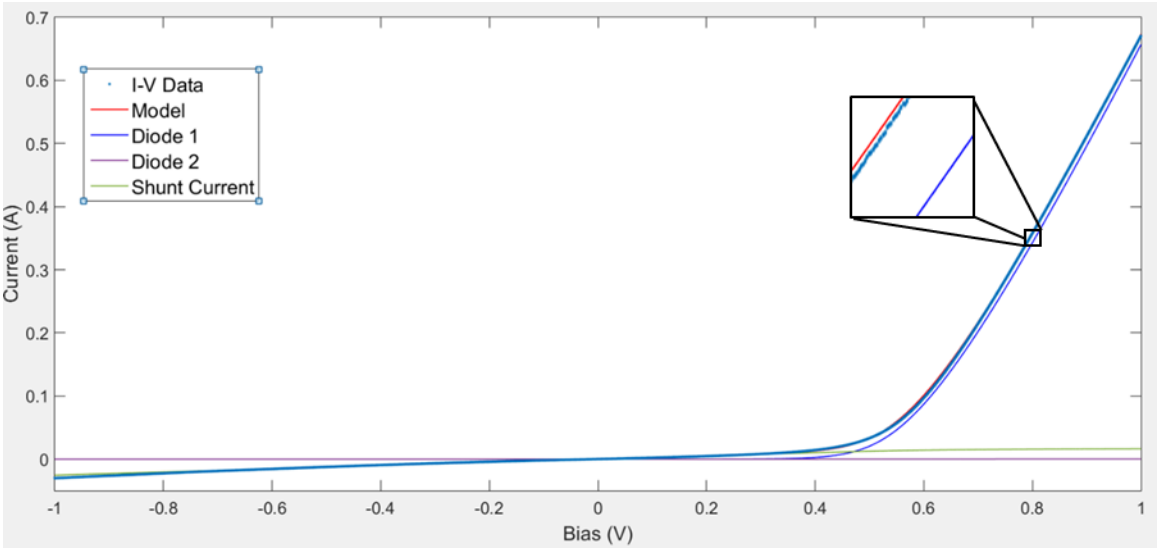

Figure 4-22: I-V response of an 8.0cm x 2.5cm laser cut m-c Si solar cell. Optimised model compared to the measured I-V data as well as the contributions made by Diode 1, Diode 2 and the Shunt are shown.

Table 4-3: Statistical analysis of extracted parameters of the laser cut sample.

Parameter	Mean	Standard Deviation	Relative Standard Deviation
I_{01} (A)	2.920×10^{-7}	9.005×10^{-8}	3.084×10^{-1}
I_{02} (A)	4.670×10^{-6}	2.324×10^{-6}	4.976×10^{-1}
n_1	1.836	0.048	2.614×10^{-2}
n_2	6.625	1.115	1.683×10^{-1}
R_{SE} (Ω)	0.148	0.001	6.757×10^{-3}
R_{SH} (Ω)	3.848×10^{1}	3.040	7.900×10^{-2}

The main contribution of current can be noted in Figure 4-22 to be as a result of the shunt from -1 V to approximately 0.425V. This is confirmed by the low shunt resistance value shown in Table 4-3. The cause of the low shunt value is possibly damage caused in the laser cutting process of the PV cell. For the remainder of the I-V response in Figure 4-22, the main current contribution is due to diode 1. The ideality factor is between 1 and 2, this implies that the main current contribution is due to a diode that follows the SRH model for recombination. The remainder of the current response is due to the second diode with ideality factor much greater than that predicted by the SRH model (ideality greater than 2). Therefore, this diode accounts for defect related mechanisms, the origin thereof is likely due to the defects related to the laser cutting process and edge related defects [18].

Figure 4-23 is the result of applying the optimised model parameters on the extended dark I-V data of the sample. The figure compares the data to the overall model applied, as well as the current contribution of the various terms of the model (equation 4-1).

Figure 4-23 highlights the inadequacy of the application of the optimised values from the forward bias to reverse bias. The shunt, while making a large contribution to the reverse current, cannot adequately describe the reverse current. The breakdown related results below will give an indication of the spatial position of the current flow as well as the magnitude of the current within the laser cut sample. The modelling of the reverse I-V curve was not studied further.

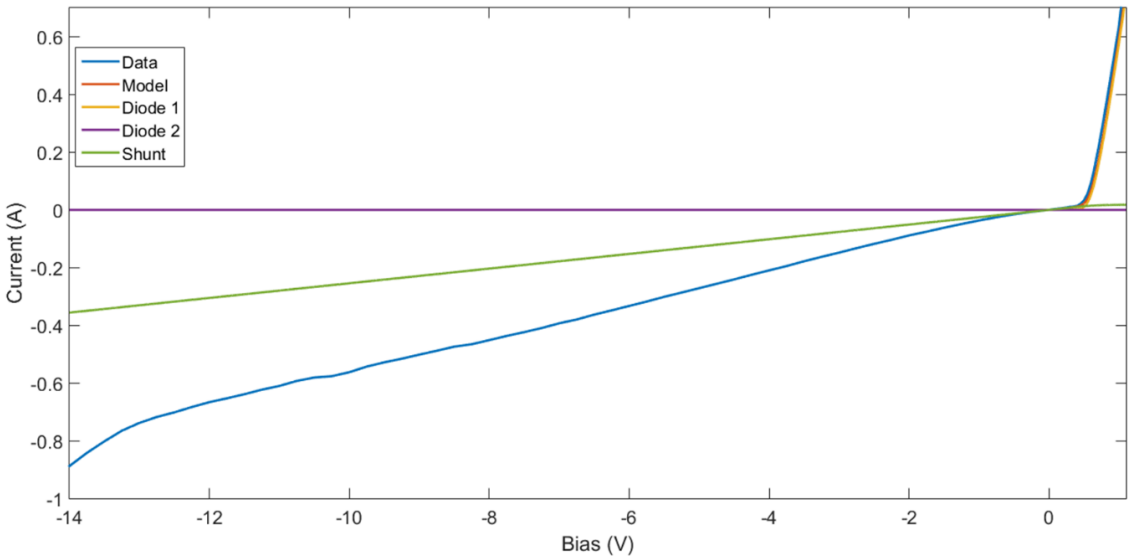

Figure 4-23: The extended I-V curve of the laser cut sample, with the corresponding contributions made by the applied model.

4.3.2. LBIC map

Figure 4-24 (a) shows the map of the V_{OC} sample and (b) shows the map of the I_{SC}. In both maps it is possible to distinguish (1) the busbar, (2) the "fingers", (3) poor junction quality at the edges- possible induced shunt, (4) shunts, (5) reduced current collection through preferential flow through laser induced shunts and damage to the junction - discussed below, and (6) various other crystal structure defects such as grain boundaries, etc.

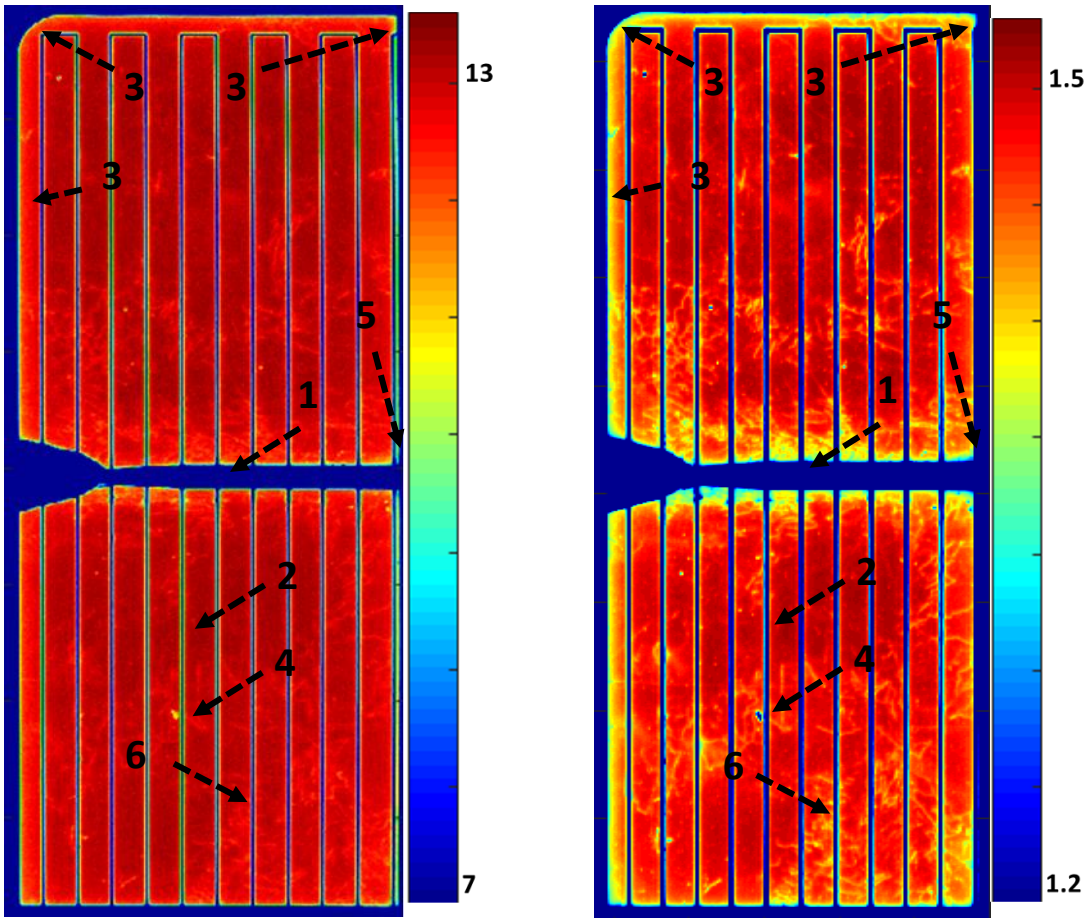

(a) (b)

Figure 4-24: (a) V_{OC} map (mV), (b) I_{SC} map (mA).

4.3.3. Forward EL image

Figure 4-25 shows the forward bias (1.1 V) EL intensity image of the second sample. In the image it is possible to distinguish (1) the busbar, (2) the "fingers", (3) reduced recombination through preferential flow through laser induced shunt and damage to the junction - discussed below, (4) back-contact, (5) poor junction quality at the edges - possible induced shunt, and (6) various other crystal structure related features.

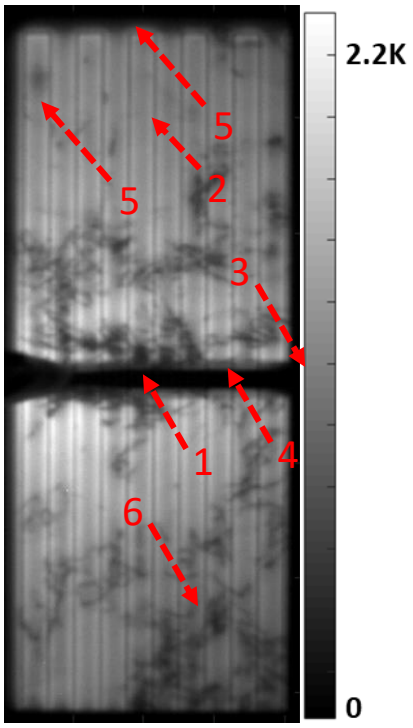

Figure 4-25: Forward bias EL intensity image at 1.1 V (counts).

4.3.4. ReBEL EL image

Figure 4-26 shows the ReBEL intensity images of Sample 2 at (a) -5 V, (b) -10V and (c) -14V. Various breakdown sites are visible in the images. Features (1) and (2) are pre-breakdown sites as they are visible at -5 V, they are related to the laser cutting process across a finger. The localised heating of the device due to the laser cutting could have induced local defect states through the diffusion of metal in the material or the conversion of the crystalline Si to amorphous Si. Features (3), (4), (5) are breakdown sites visible at -14 V implying that they are either related to IFE through band-to-band tunnelling or AB. Feature (4) is located near the busbar and is located at grain boundaries, the feature is discussed below regarding the emission-voltage of a particular pixel within that feature. Feature (5) as discussed below, the result of the emission-voltage response implies that the emission is due to AB.

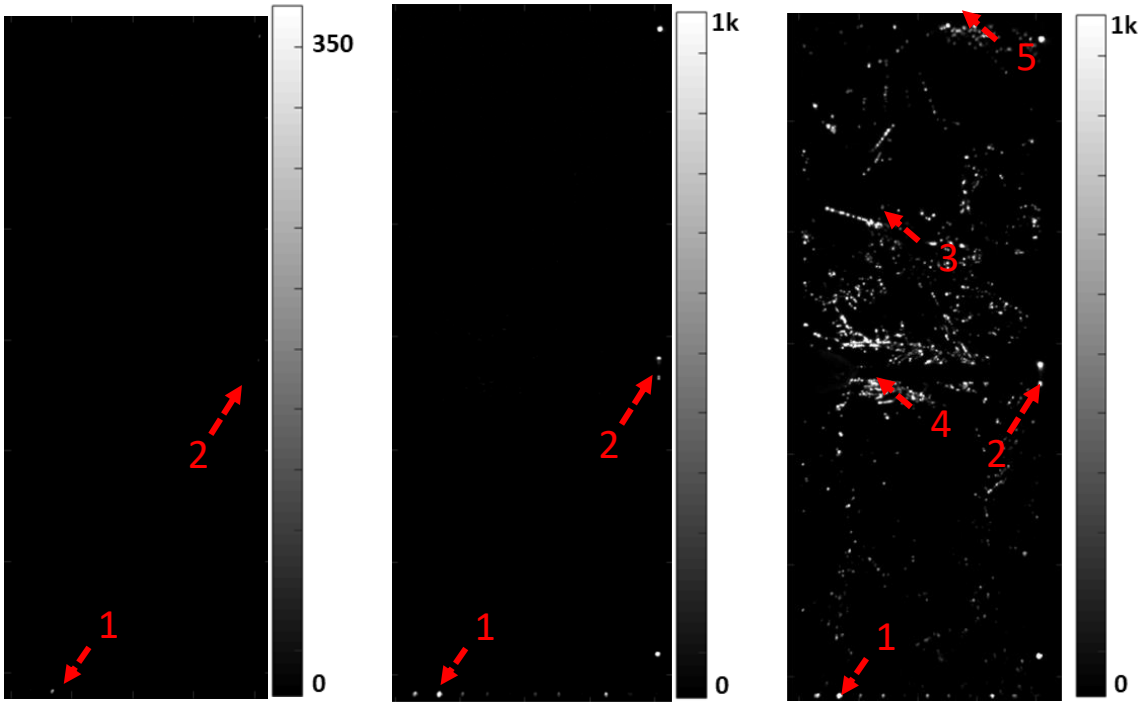

(a) (b) (c)

Figure 4-26: ReBEL intensity images (counts) at (a) -5 V, (b) -10 V, (c) -14 V.

4.3.5. Emission-voltage curves of interesting features

The numbering of the positions in this section is the same as above. The breakdown is highly localised; the emission-voltage curves of 'pixel' diodes numbered above is shown below. It is assumed that the emission response is a direct indication of the localised current through the breakdown site. Therefore, the emission-voltage curve is indicative of the current-voltage response. The quantum efficiency of the optics and sensor are not considered; however, as it is only used as an indicative measure; therefore, the assumption is sensible. The emission-voltage curves which show an emission response from below -8 V show an anomalous drop in emission intensity. This anomaly is likely due to the EL image obtained at -9 V. Therefore, these outliers can be disregarded.

Figure 4-27 (a) shows the emission-voltage curve of position 1. The emission of this "pixel" diode is detectable near -4 V which is typical of a pre-breakdown site. At -10 V the emission-voltage curve begins to flatten off with small anomalous peaks superimposed on the curve. These peaks have not been investigated fully. A plausible explanation of the flattening curve is the saturation of the mechanisms that cause light emission. Figure 4-27 (b) shows the corresponding ReBEL image at -5 V, this indicates the shape and position of the breakdown site. Figure 4-27 (c) shows the corresponding EL image at 1.1 V. No detectable feature is noticeable. This breakdown site is likely due to the laser induced extended defects or the conversion of crystalline Si to amorphous Si rather

than the pre-breakdown mechanism proposed by Lausch et al [21]. Light emission is likely caused by radiative intra-band thermalisation of hot carriers at the extended defects [23], [25].

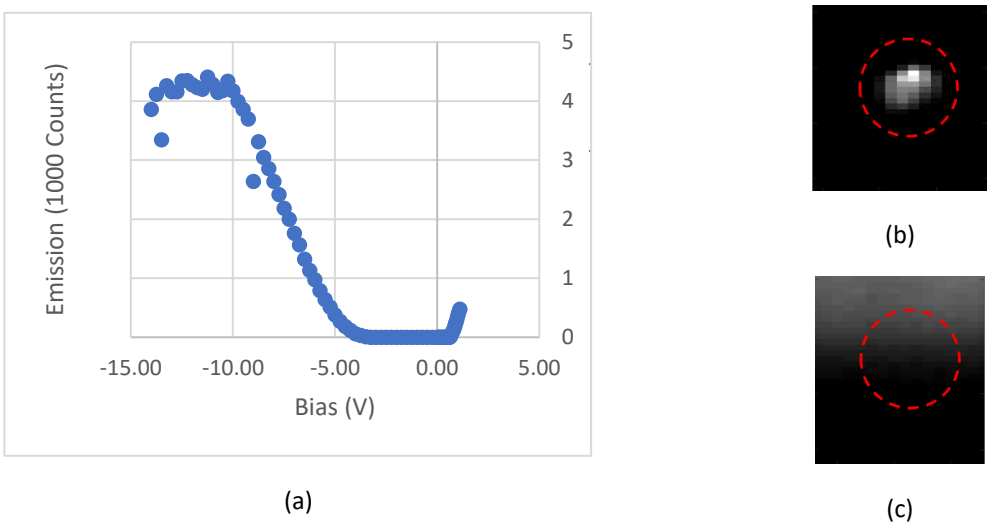

Figure 4-27: Position 1 (a) emission-voltage curve, (b) ReBEL image at -5 V, (c) EL image at 1.1 V.

Figure 4-28 (a) shows the emission-voltage curve of position 2. The emission of the "pixel" diode is detectable at -5 V which is typical of a pre-breakdown site. Figure 4-28 (b) shows the corresponding ReBEL image at -10 V showing the shape and position of the breakdown site. Figure 4-28 (c) shows the corresponding EL image at 1.1 V. No detectable feature is noticeable. This breakdown site is related to the laser cutting process. This breakdown site is likely due to the laser induced extended defects or the conversion of crystalline Si to amorphous Si rather than the pre-breakdown mechanism proposed by Lausch et al [21]. Light emission is likely caused by radiative intra-band thermalisation of hot carriers at the extended defects [23], [25].

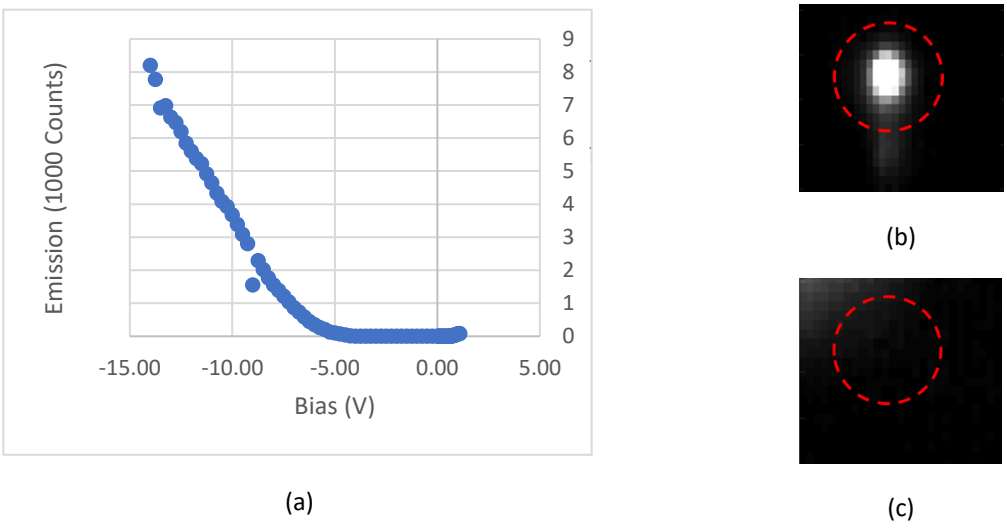

Figure 4-28: Position 2 (a) emission-voltage curve of, (b) ReBEL image at -10 V, (c) EL image at 1.1 V.

Figure 4-29 (a) shows the emission-voltage curve of position 3, indicating a soft breakdown curve. This breakdown site forms part of a linear feature on the cell. The emission of this “pixel” diode is detectable at -11 V which is typical of type II breakdown [21]. Figure 4-29 (b) shows the corresponding ReBEL image at -14 V showing the shape and position of the breakdown site. Figure 4-29 (c) shows the corresponding EL image at 1.1 V, the image indicates a crystal defect. This is typically related to $FeSi_2$ needles [25].

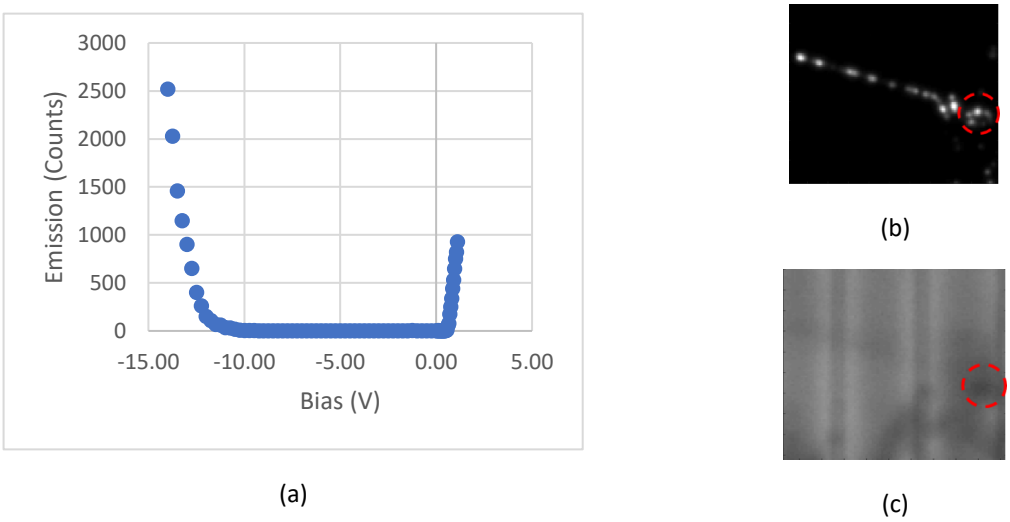

Figure 4-29: Position 3 (a) emission-voltage curve of, (b) ReBEL image at -14 V, (c) EL image at 1.1 V.

Figure 4-30 (a) shows the emission-voltage curve of position 4 on the second sample, indicating a soft breakdown curve. The emission of this “pixel” diode is detectable at -10.25 V which is typical of type II breakdown [21]. Figure 4-30 (b) shows the corresponding ReBEL image at -14 V, this indicates the shape and position of the breakdown site. Figure 4-30 (c) shows the corresponding EL image at 1.1 V. Figure 4-24 and Figure 4-25 show that this feature is close to a busbar and grain boundaries. It is therefore possible that this feature is related to IFE through band-to-band tunnelling or IFE through trap assisted tunnelling, the case depending on the presence $FeSi_2$ needles or not [25].

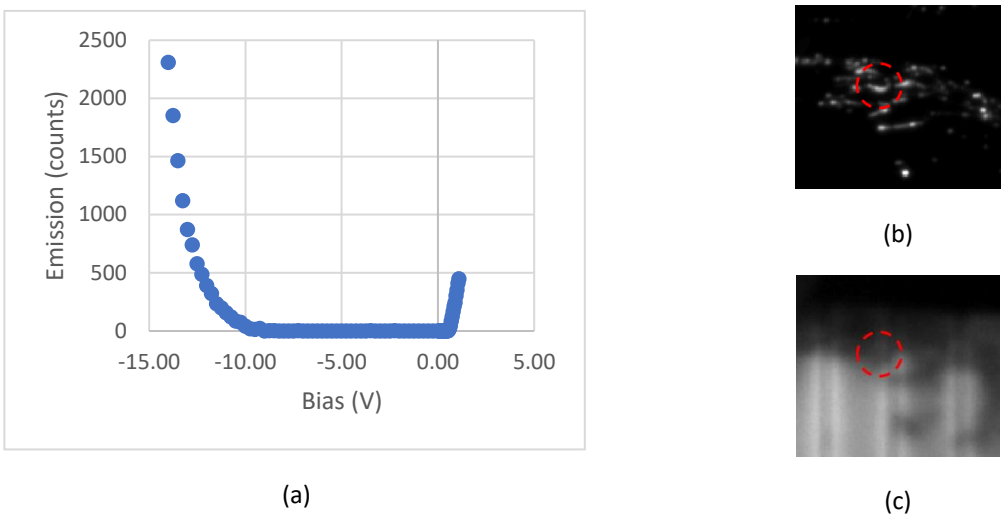

Figure 4-30: Position 4 (a) emission-voltage curve, (b) ReBEL image at -14 V, (c) EL image at 1.1 V.

Figure 4-31 (a) shows the emission-voltage curve of position 5, indicating a hard breakdown curve. The emission of this "pixel" diode is detectable at -12 V which is typical of type II or type III breakdown [21]. Figure 4-31 (b) shows the corresponding ReBEL image at -14 V, this indicates the shape and position of the breakdown site. Figure 4-31 (c) shows the corresponding EL image at 1.1 V. The hard breakdown curve and the fact that the emission is limited by series resistance (as indicated by the linear response after the breakdown) indicates that avalanche breakdown is occurring [21].

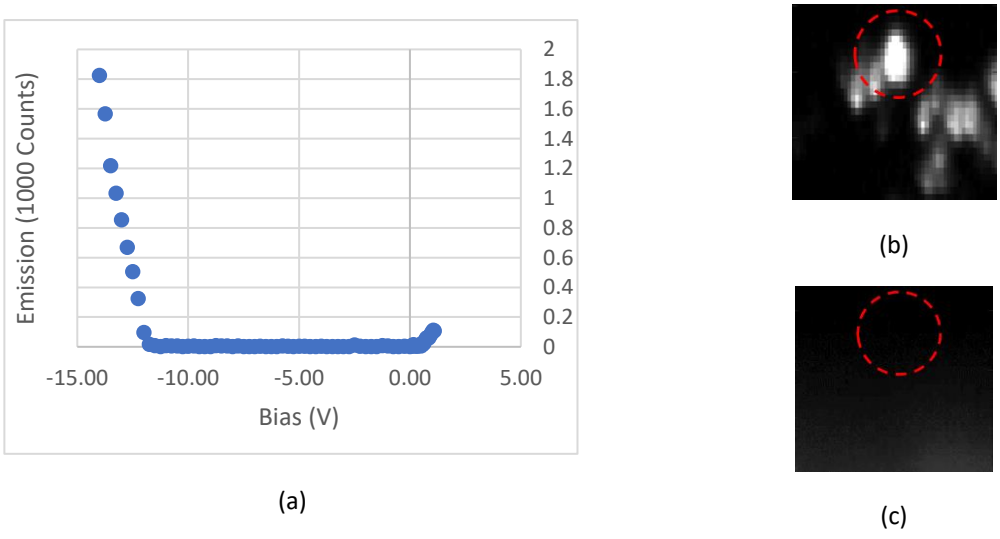

Figure 4-31: Position 5 (a) emission-voltage curve of, (b) ReBEL image at -14 V, (c) EL image at 1.1 V.

4.3.6. Series Resistance Map

Figure 4-32 shows the series resistance map generated from voltage dependent EL, by the method developed by Hinken et al [30]. Feature (1) is the busbar, the calculated resistance is noisy over the busbar; this is due to the fact that the applied technique is not applicable to the busbar data. Similarly, the technique does not apply to the data from the fingers (2). The region indicated (3)

contains crystal structure defects as indicated above in the EL intensity image, the region also appears to have an overall higher series resistance. The series resistance between the fingers (4) shows varying series resistance. The series resistance goes from its lowest right next to the finger to its highest in the middles between the fingers. The regions similar to (5), show a higher series resistance to that of the remainder of the cell. The series resistance in these regions appears extremely noisy, the EL signal from the same regions (as seen in the EL intensity image above) are lower than the surrounding areas. It is possible that a greater portion of recombination in these regions is occurring due to defect states and therefore fall outside of the sensitivity of the Si CCD used to acquire the images. Therefore, the emission detected will not be useful in the determination of the series resistance due to lack of information of recombination through defect mechanisms.

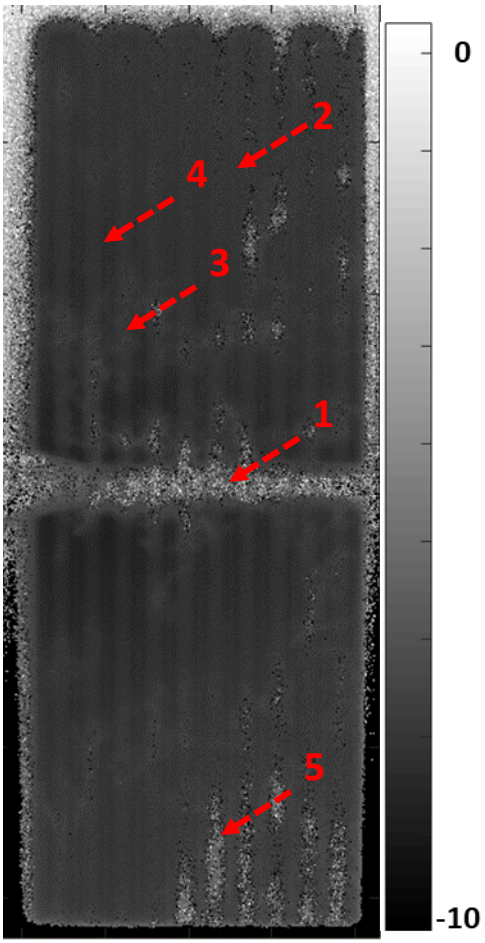

Figure 4-32: Series resistance map of sample (arbitrary logarithmic units).

4.3.7. Breakdown Voltage Map

For Figure 4-33, it is assumed that any count greater than 100 counts is well above the noise of the background and is therefore the start of reverse bias breakdown. Using the voltage dependent EL data, it is possible to map the breakdown voltage of the different breakdown sites of the cell. Figure 4-33 shows a map of the breakdown voltage of the cell; comparing this to Figure 4-26 (a), (b) and (c), it can be seen that there is a large number of breakdown sites of low breakdown emission intensity (low breakdown current).

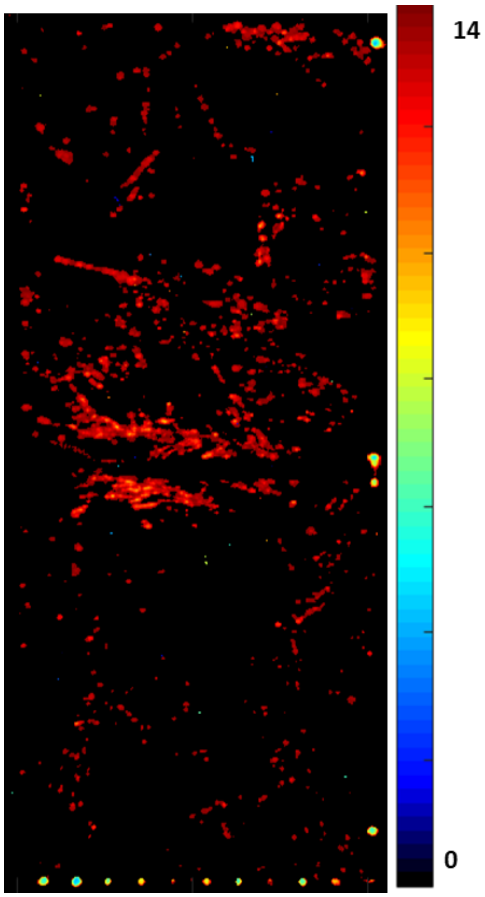

Figure 4-33: Breakdown voltage map of Sample 2 (-V).

Figure 4-34 (a) is a microscope image of the cell indicating material damage associated with the laser cutting process. Figure 4-34 (b) is the corresponding breakdown voltage map. Therefore, the breakdown of this site can either be related to the diffusion of contact metal into the material, junction damage or the conversion to amorphous Si due to the heating of the laser cutting process [25].

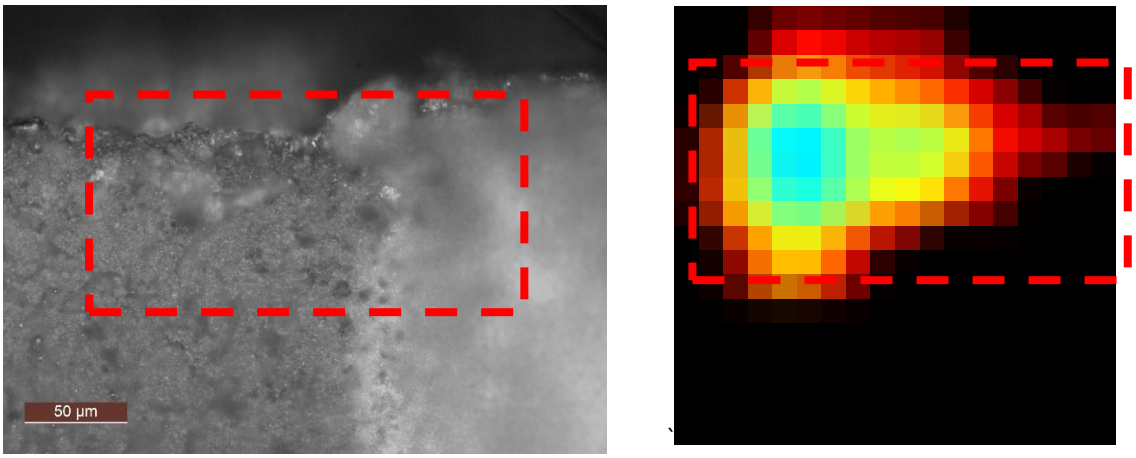

(a) (b)

Figure 4-34: (a) Microscope image of material damage near busbar, (b) breakdown voltage map

4.3.8. Infrared Thermography

Figure 4-35 shows the IR thermal image of Sample 2 at (a) -5 V, (b) -10 V and (c) -14 V. The thermal images indicate sites of high reverse current. Features (1) and (2) are related to the laser cut edges of the sample. The laser cutting process as discussed above, damaged the junction as well as possibly induced extended defects into the device. The process introduced breakdown sites as well as shunts. Feature (3) is either related to an edge shunt or breakdown. Feature (4) is on a manufactured corner of the sample; therefore, it is related to an edge shunt of some kind. Voltage dependent lock-in thermography would be required to determine the exact nature of the shunt. Thermal diffusion limits the detection of specific features within results shown in Figure 4-35.

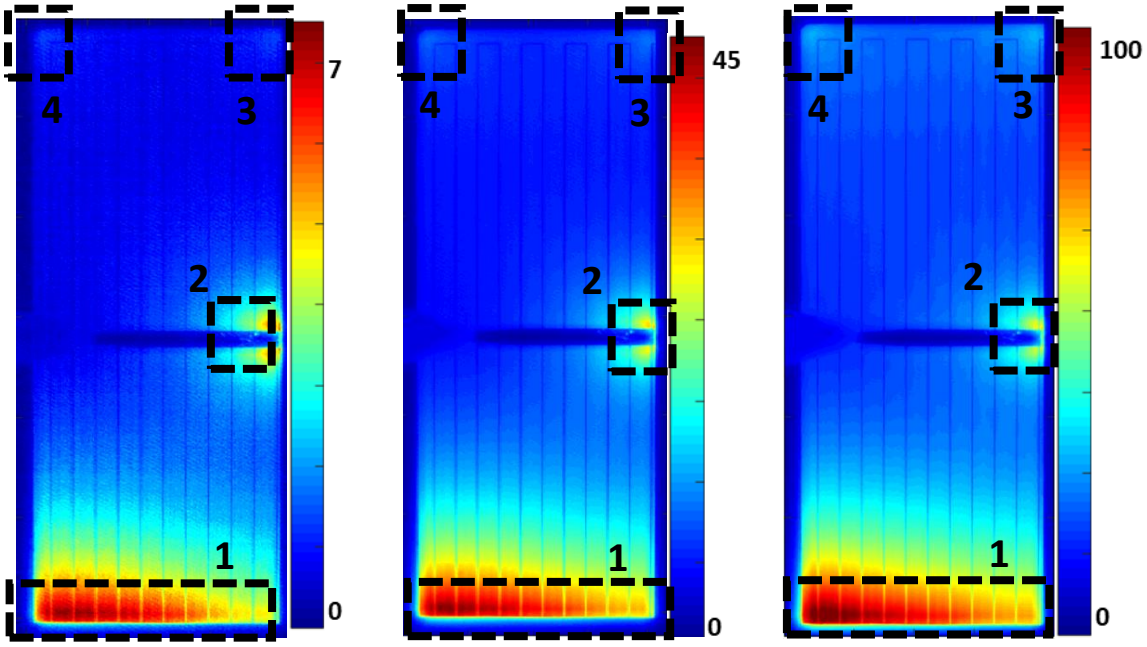

(a) (b) (c)

Figure 4-35: Reverse bias IR thermal images (arbitrary units) at (a) -5 V, (b) -10 V, (c) -14 V.

4.3.9. Comparisons of the results of Sample 2

4.3.9.1. Comparison of LBIC measurements and forward EL image

Figure 4-36 shows the comparison between the (a) forward bias EL image at 1.1 V and the (b) LBIC I_{SC} map. Feature 1 is an example of poor (b) collection efficiency and poor (a) band-to-band radiative recombination. The decrease in both recombination and efficiency can be related to either decrease in the quality of crystal quality or formation of shunts through the diffusion of metal ions into the grain boundaries from the contacts. From the results above, as well as the results in Figure 4-36, feature (2) appears to be related to a laser cutting process induced shunt. The decreased recombination and decreased efficiency at the feature is related to the local preferential flow through the shunt. This is corroborated by the thermal response of the region. Features (3) are indicated by a decrease in (a) band-to-band radiative recombination as well as the decrease in (b) measured photo-current. This is related to the location of these features: the edges of the device, likely, the localised shunting of the current due to an incompletely opened emitter, or a high ideality factor diode ("diode-like" shunt) or a high density of defect states at the edge [18] [25]. Feature (4) shows (b) a localised drop in photo-current collection efficiency likely due to the preferential flow through a shunt; the feature is related to (a) a crystal structure defect. Feature (5) has a decreased band-to-band radiative recombination and decreased photo-current collection efficiency. This is likely related to the diffusion of metal impurities from the front contacts in the laser cutting process or local conversion from crystalline Si to amorphous Si [23]. These defects can form defect bands (related to breakdown) or a continuum of defects states causing ohmic shunting in the region [18].

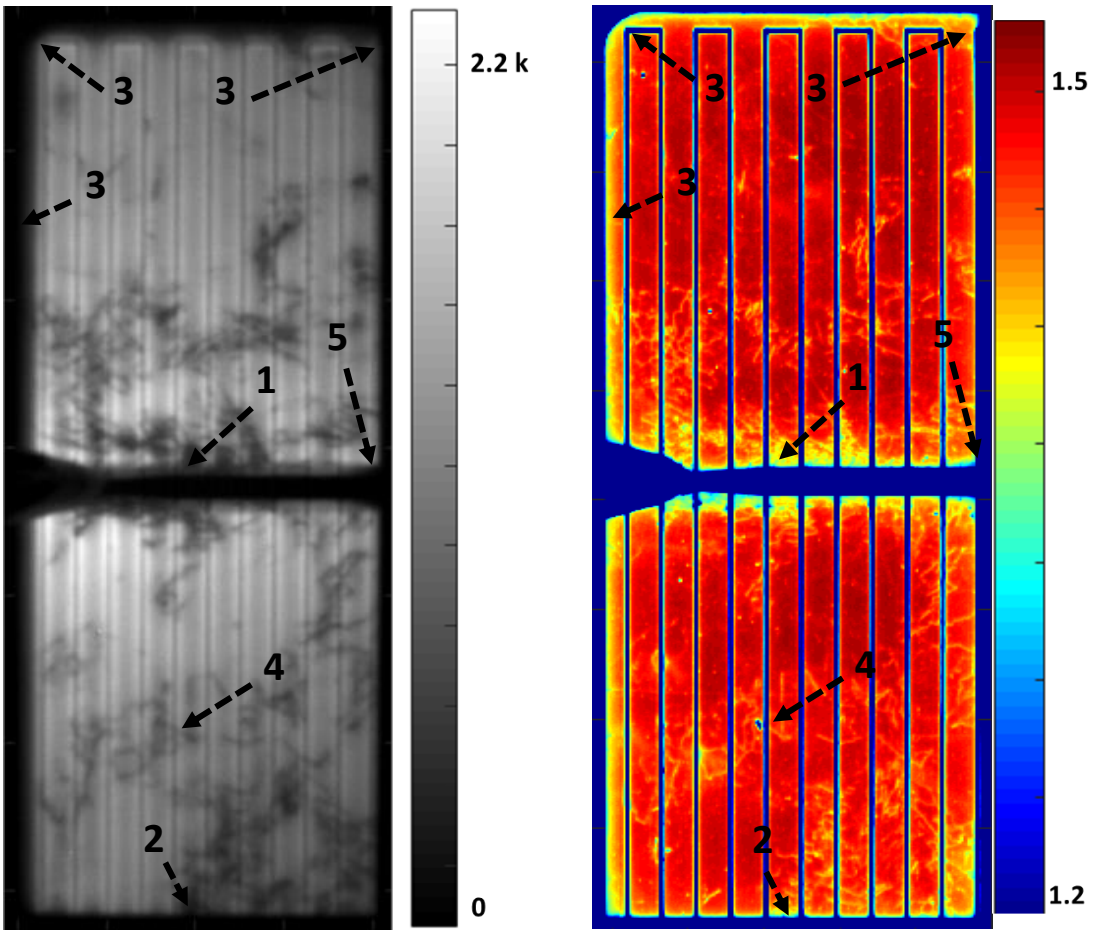

(a) (b)

Figure 4-36: (a) Forward bias EL image at 1.1V (counts), (b) I_{SC} map (mA).

4.3.9.2. Comparison of forward EL and series resistance map

Figure 4-37 shows the comparison between the (a) forward bias EL at 1.1 V and the (b) series resistance map through the voltage dependent EL method. Feature (1) is the busbar, the (b) calculated resistance is noisy over the busbar; this is due to the fact that the applied technique is not applicable to the busbar data. Similarly, the technique does not apply to the data from the fingers (2). The region indicated (3) contains crystal structure defects as indicated (a) EL intensity image, the region also appears to have an overall higher series resistance. Otherwise, the decrease in band-to-band radiative recombination is due to the increase of alternate recombination mechanisms (non-radiative or defect related recombination); implying that the increased calculated series resistance is simply an artefact of the applied technique. The series resistance between the fingers (4) shows increasing (b) from next to the finger to between the fingers. This can be correlated with the decrease in luminescence (a). This increase in resistance is due to an increased current path. The regions similar to (5), show a higher (b) series resistance compared to that of the remainder of the cell. The series resistance in these regions appear extremely noisy, the (a) EL signal from the same regions is lower than the surrounding areas. It is possible that a greater

portion of recombination in these regions is occurring due to defect states and therefore fall outside of the spectral response of the Si CCD used to acquire the images. The lack of detection of defect related emission in these areas affects the determination of the series resistance.

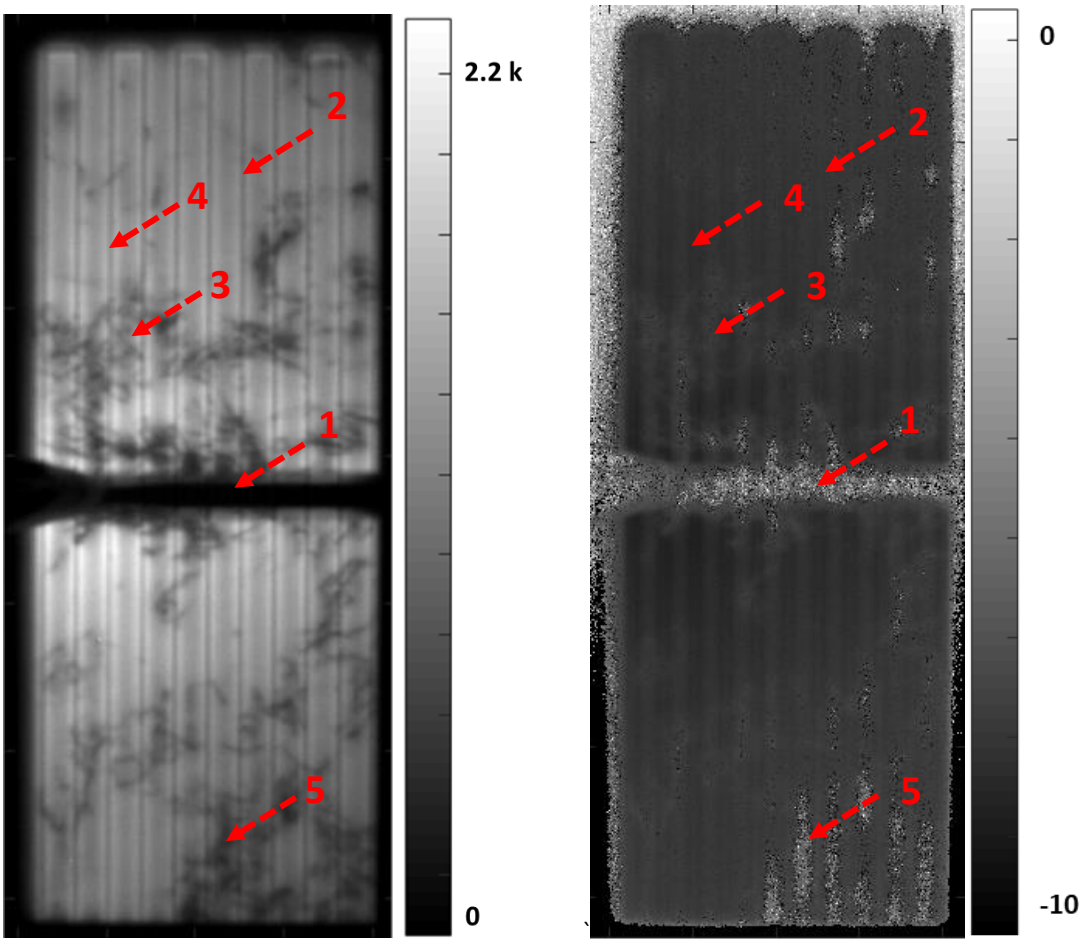

(a) (b)

Figure 4-37: (a) EL at 1.1 V (counts), (b) Series resistance map (arbitrary logarithmic units).

4.3.9.3. IR Thermography compared to ReBEL image

Figure 4-38 shows the comparison between the (a) ReBEL image at -14 V and the (b) IR thermal image at -14 V. Feature (1) is related to the laser cut portion of the sample near the contact fingers and Feature (2) is related to the laser cut portion of the sample near the busbar. They can be related to multiple breakdown sites and localised heating. As the entire region is showing heating, it is likely that diffused metal ions or local conversion from crystalline Si to amorphous Si has resulted in multiple local shunts that are visible in thermal images (Figure 4-35) at low voltages. The breakdown sites do contribute to the heating; however, the low onset voltage for heating as well as the magnitude of heating implies the presence of both shunting and reverse bias breakdown or non-radiative breakdown. However, this could be explained by the ohmic shunting caused by extended defects, where the light emission could be related to the thermalisation of intra-band hot electrons.

Feature (3) shows a (b) minor thermal response from as low as -5 V (Figure 4-35). It also shows (a) breakdown occurs at -5 V (Figure 4-33). The low thermal response and breakdown emission indicates that the defect is in fact a local breakdown site and is not related to shunting. This feature is related to the laser cutting of a single finger and is therefore related to either defects related to diffused metallic impurities or the formation of other extended defects (presence of local amorphous Si). Feature (4) shows (b) minor localised heating and no detected (a) local breakdown. Unless the breakdown luminescence falls outside of the sensitivity of the Si CCD, the feature is related to an edge shunt. Voltage dependent lock-in thermography would be required to determine the exact nature of the shunt.

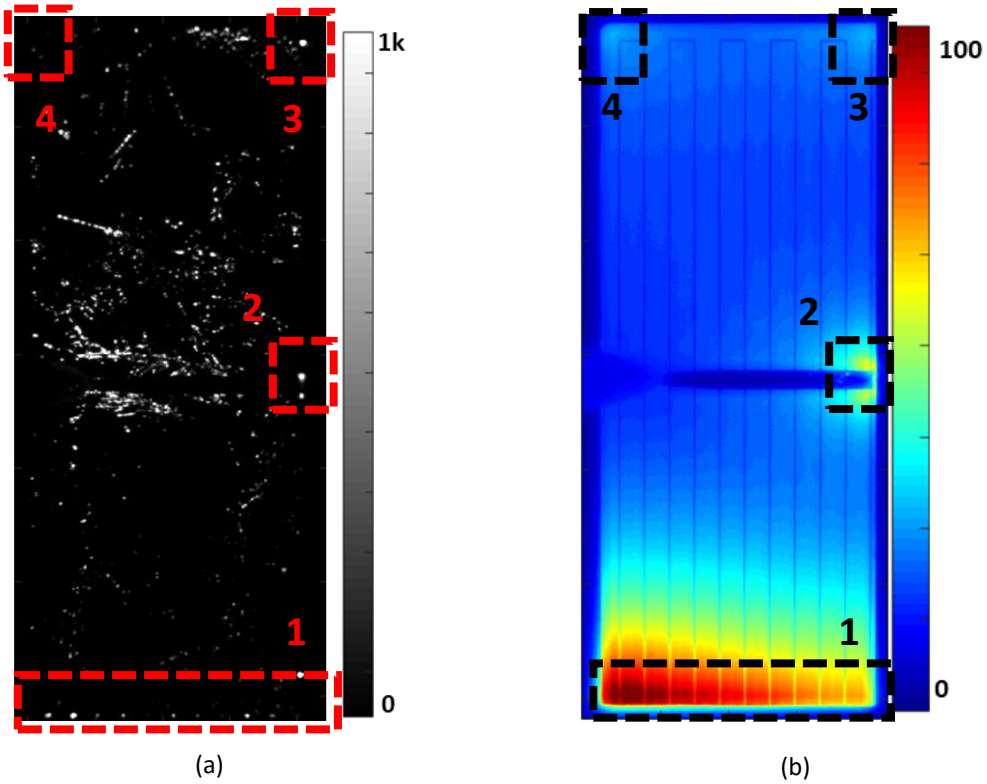

Figure 4-38: (a) ReBEL at -14 V (counts), (b) reverse bias IR thermal image at -14 V (K).

4.3.9.4. Comparison of forward EL, LBIC and breakdown voltage map

Figure 4-39 shows a comparison between the various features present in the (a) LBIC I_{SC} map, (b) photograph with the breakdown voltage as an overlay and (c) the forward bias EL image at 1.1 V. The colour scale is that of the corresponding figures above. In Figure 4-39 (b), breakdown with low breakdown voltage (in the vicinity of -5 V) is noticeable in regions (1), (2) and (4). These correspond to the laser cut front contacts of the cell. The corresponding regions in the EL image show decreased band-to-band radiative recombination. This is likely due to local conversion of crystalline Si to amorphous Si or the diffusion of the metal ions of the contacts into the material of the device. This would induce defects states into the band structure. Region (4) shows a low breakdown voltage in

the overlay (b). It is apparent in the (c) EL image that with the decreased band-to-band radiative recombination and shape that the region contains crystal structure defects. Therefore, it is likely that the feature is related to IFE or thermionic emission. The features apparent in (c) regions 5 and 6 are due to a high density of grain boundaries which often contain gettered impurities. The decreased signal is indicative of decreased band-to-band radiative recombination. The features correspond with breakdown sites in the (b) breakdown voltage overlay and possibly can be related to $FeSi_2$ needles that can form in grain boundaries [25]. The features show a decreased current generation. Regions (7) and (8) in the breakdown voltage overlay contain linear breakdown features. Both features are apparent in the (c) EL image; however, do not correspond to noticeable decrease in current in (a) the I_{sc} map. The breakdown voltage overlay indicates breakdown voltages in the region of type II breakdown. This breakdown type is associated with IFE or thermionic emission. The breakdown in regions (7) and (8) is likely related to the gettered defects in a grain boundary that does not penetrate deep into the material therefore, not limiting the photo-current response.

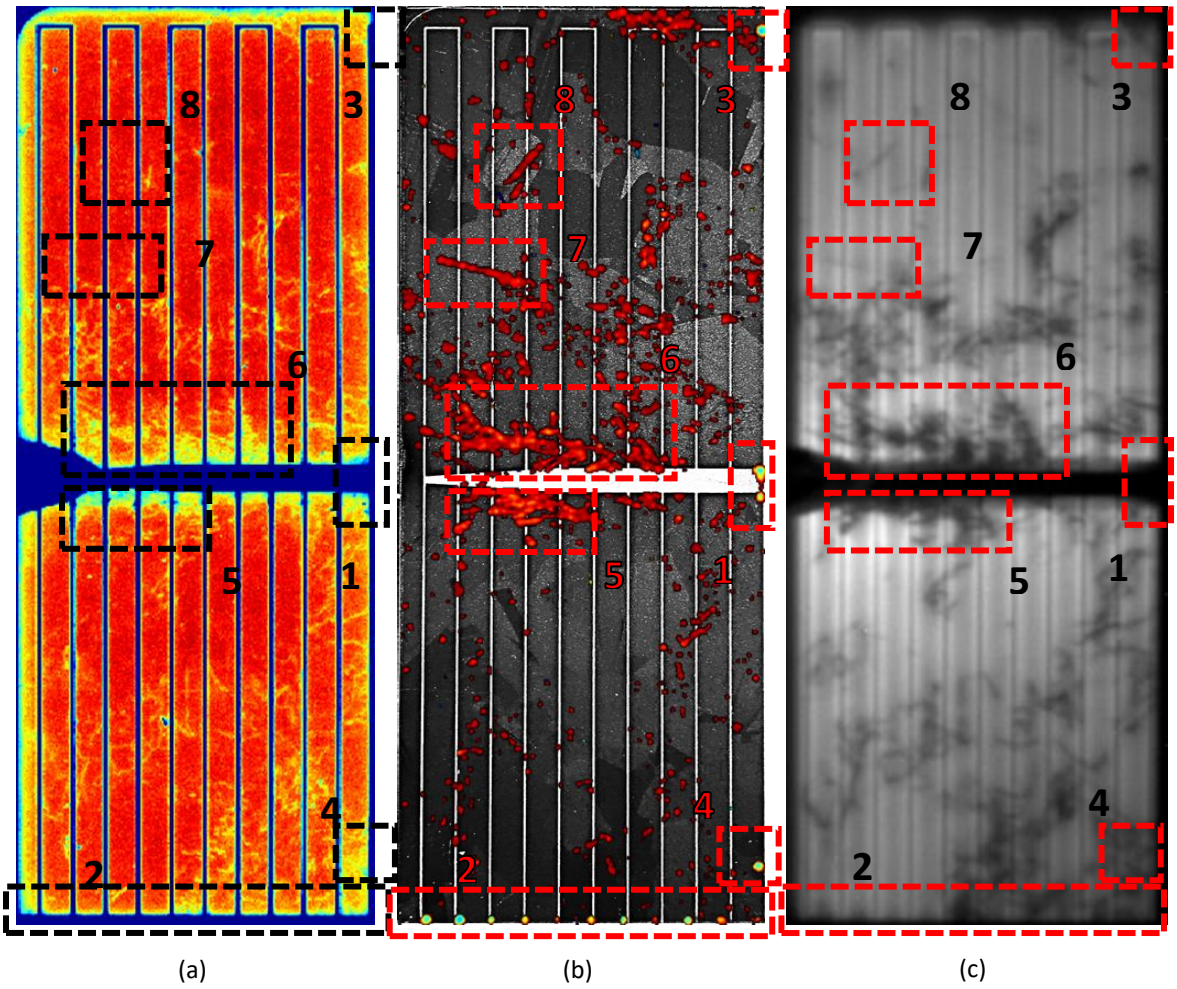

Figure 4-39: (a) LBIC I_{SC} map, (b) photograph with the breakdown voltage as an overlay and (c) the forward bias EL image at 1.1 V, (same colour scheme as above).

4.3.10. Summary of Sample 2 Results

The results obtained for Sample 2 has shown defects and properties that illustrate the strengths and failings of the various techniques employed. As the sample is m-c Si, grain boundaries can be noted in techniques such as LBIC and EL imaging. The gettered defects cause shunting and defect levels decreasing efficiency and band-to-band recombination. The reverse current noted in the dark I-V curve was explained by the various breakdown types distributed across the sample as noted in the ReBEL intensity images and the IR thermal images. The laser cutting process induced defects into the sample as noted in the reverse portion dark I-V curve as well as the breakdown related results. It can be noted when comparing the photograph of the cell and the voltage breakdown map that the laser cutting process induces defects that are related to low voltage breakdown.

4.4. Summary of Results

LBIC measurements were shown to identify photo-induced current limiting defects. The technique successfully identified localised shunts, crystal grain boundaries and micro-cracking. The poor device quality at manufactured edges from improper isolation was also identified as edge shunting [18]. The laser cut edges also show non-ideal characteristics due to the localised heating and subsequent damage due to the cutting process. Forward bias EL (including the voltage dependent approach) was used to identify regions of high effective series resistance, micro-cracking and crystal grain boundaries. ReBEL and breakdown voltage mapping was used to identify and characterise various breakdown sites on both samples. Both diamond scribing and laser cutting were shown to have induced defects related to reverse bias emission. This emission is likely related to the pre-breakdown emission of intra-band thermalisation of hot electrons at extended defects. In Sample 1, IR thermography was used to identify and confirm the ohmic nature of the induced shunt. In Sample 2, IR thermography was used to identify localised heating in the reverse bias.

The results obtained for both Sample 1 and Sample 2 were adequate examples of the techniques applied in this dissertation. High voltage Si modules are currently under study as a possible replacement of conventional Si modules due to the decrease in resistive losses [53]. Therefore, as conventional 6” x 6” cells are cut to smaller sizes to increase the number of cells in a module obtain higher module voltages, the characterisation techniques applied here would benefit the optimisation of the cutting procedures. Isolation of laser cut or diamond scribed edges could limit the effect of local damage.

5. Conclusions

The first objective of this study was to design and construct a system that could be used for the advanced characterisation and identification of defects and their location within photovoltaic (PV) cells. This system was designed to include Light Beam Induced Current (LBIC) measurements, Electroluminescent (EL) intensity imaging and Infrared (IR) thermography. This objective was successfully achieved as indicated by the results discussed in Chapter 4. The system is capable of performing LBIC measurements, EL intensity imaging, dark IR thermography and dark I-V measurements.

The second objective of this study was the implementation of the above-mentioned techniques to identify and characterise performance, and/or device longevity limiting defects. The objective was successfully achieved. Various defects were identified with the techniques utilised in this study. By comparing the results obtained, the different characteristics/effects of the defects were obtained and thoroughly analysed.

In this study, a Genetic Algorithm for Parameter Optimisation (GAPO) was developed in MATLAB. The program was applied for the extraction of parameters from the two-diode model of dark current-voltage (I-V) data of PV cells. This satisfies the third and final objective of this study. The algorithm was able to identify the various contributions to the overall current of each sample based upon the parameters extracted. It identified the current contribution of the shunt, the SRH model for recombination and the defect related currents such as edge currents, diode-like shunts, etc. Genetic Algorithms (GAs) are relatively computationally expensive; however, the GAPO was shown to be effective at extracting the parameters. Multiple runs of the GAPO on the same data allowed for the determination of the standard deviation of the parameters. The algorithm also identified the parameters in the model that had the least impact on the data, from the relative standard deviation of each parameter.

Sample 1 was diamond scribed 55 mm x 55 mm multi-crystalline (m-c) Si PV cell. Sample 1 was successfully analysed using the above-mentioned techniques. The current contribution of the ohmic shunt was shown to be negligible – before a shunt was induced through high reverse bias (-24 V). Voltage dependent Reverse Bias EL (ReBEL) allowed for the generation of a breakdown voltage map for radiative breakdown mechanisms. This led to the conclusion that the scribing process can induce low voltage breakdown emission sites. The ReBEL images also confirmed the presence of other breakdown mechanisms. Therefore, if such a cell was present in a module under partial shading, the cell could experience significant breakdown current. The localised heating could decrease the longevity of the device or the encapsulant layer. A strong ohmic shunt (very low shunt

resistance) was induced when the cell was reverse biased at approximately -24 V. This was confirmed using IR thermography and GAPO on the I-V data of the cell.

Sample 2, a laser cut 80 mm x 25 mm m-c Si PV cell, was successfully analysed. At both low reverse and forward bias, the ohmic shunt current was shown to have a significant effect. The forward bias ohmic shunt current contribution was determined using the GAPO on the measured I-V data. The breakdown voltage map for radiative breakdown mechanisms led to the conclusion that the laser cutting process can induce low voltage breakdown emission sites. The ReBEL images also confirmed the presence of other breakdown mechanisms. Therefore, if such a cell was present in a module under partial shading, the cell could experience significant breakdown current. The localised heating could decrease the longevity of the device or the encapsulant layer. This was confirmed using reverse bias IR thermography.

The results obtained for both Sample 1 and Sample 2 demonstrate the techniques applied in this dissertation. High voltage Si modules are currently being considered as a possible replacement of conventional Si modules due to the decrease in resistive losses. Therefore, as conventional 6” x 6” cells are cut to smaller sizes to increase the number of cells in a module obtain higher module voltages, the characterisation techniques applied here would benefit the optimisation of the cutting procedures. Isolation of laser cut or diamond scribed edges could also limit the effect of local damage.

The IR thermography performed in this study was done under steady-state conditions. Heat diffusion decreases the ability of steady-state IR thermography; therefore, in future studies, Lock-in Thermography (LIT) under both dark and light conditions will be utilised so as to minimise thermal spreading. The application of voltage dependent LIT will also be used to further characterise shunts and breakdown sites of PV cells. In future work, EL using an InGaAs CCD camera will be utilised in the identification of defect band related EL imaging. Similar results will be obtained of voltage dependent Photoluminescence (PL) imaging. This will be used in conjunction with I-V data and band-to-band EL imaging to determine local parameters of a PV cell. In future work, a voltage dependent LBIC will be applied to conduct local light I-V parameter extraction as well as the inclusion of a reflection map to determine whether a specific feature is related to a reflection event or not. The GAPO was not applied to the light I-V data and local I-V data obtained through LBIC. However, in future work on similar algorithms, GAPO will be extended to light I-V data of cells, local I-V data, EL/PL imaging, and LIT of cells and to the parameter extraction of models applied to PV modules.

References

[1] Boyle, G. (2012). Renewable Energy: Power for a Sustainable Future. Oxford: Oxford University Press.

[2] Smith, W. (1873). The action of light on selenium. Journal of the Society of Telegraph Engineers, 2(4), pp.31-33.

[3] Solargis.com. (2017). [online] Available at: http://solargis.com/assets/graphic/free-map/DNI/Solargis-World-DNI-solar-resource-map-en.png [Accessed 22 Jun. 2017].

[4] Bellini, E. (2017). South Africa's PV capacity reaches 1.47 GW, new PV installations for 2016 total 509 MW. [online] pv magazine International. Available at: https://www.pv-magazine.com/2017/03/17/south-africas-pv-capacity-reaches-1-47-gw-new-pv-installations-for-2016-total-509-mw/ [Accessed 22 Jun. 2017].

[5] IEA PVPS Trends 2016 in Photovoltaic Applications. (2016). 21st ed.

[6] IRENA (2016), Solar PV in Africa: Costs and Markets

[7] Sustainable.co.za. (2017). Solar Panels for Sale | Competitive Solar Panel Prices - Sustainable.co.za. [online] Available at: http://www.sustainable.co.za/solar-power/solar-panels.html?limit=all [Accessed 6 Oct. 2017].

[8] Crozier, J. (2012), Characterization of cell mismatch in photovoltaic modules using electroluminescence and associated electro-optic techniques, MSc thesis, Nelson Mandela Metropolitan University.

[9] Zhang, B., Yang, C., Liu, W. and Liu, A. (2012). Origin of breakdown mechanism in multicrystalline silicon solar cells. Applied Physics Letters, 101(9), 093903.

[10] Breitenstein, O., Rakotoniaina, J.P., Kaes, M., Seren, S., Pernau, T., Hahn, G., Warta, W., and Isenberg, J. Lock-In Thermography - A Universal Tool for Local Analysis of Solar Cells, Proceedings of 20th European Photovoltaic Solar Energy Conference, (2005), p. 590-593

[11] Bauer, J., Wagner, J., Lotnyk, A., Blumtritt, H., Lim, B., Schmidt, J. and Breitenstein, O. (2009). Hot spots in multicrystalline silicon solar cells: avalanche breakdown due to etch pits. Physica Status Solidi (RRL) - Rapid Research Letters, 3(2-3), pp.40-42.

[12] Bezuidenhout, L., (2015), On the characterization of photovoltaic device parameters using light beam induced current measurements, MSc thesis, Nelson Mandela Metropolitan University.

[13] Sze, S. (2001). Semiconductor Devices Physics and Technology. 2nd ed. New York: John Wiley & Sons, Inc.

[14] Overstraeten, R. and Mertens, R. (1986). Physics, technology and use of photovoltaics. Bristol: Adam Hilger Ltd.

[15] Ashcroft, N. and Mermin, N. (1988). Solid state physics. Fort Worth: Saunders College.

[16] Nelson, J. (2003). The physics of solar cells. London: Imperial College Press.

[17] Breitenstein, O., Rakotoniaina, J., Al Rifai, M. and Werner, M. (2004). Shunt types in crystalline silicon solar cells. Progress in Photovoltaics: Research and Applications, 12(7), pp.529-538.

[18] O. Breitenstein, P. Altermatt, K. Ramspeck, M.A. Green, Jianhua Zhao, A.Schenk, Interpretation of the commonly observed I–V characteristics of c-Si cells having ideality factor larger than two, in: IEEE Proceedings of the Fourth World Photovoltaic Solar Energy Conference, 2006. 879

[19] Breitenstein, O., Bauer, J. and Rakotoniaina, J. (2007). Material-induced shunts in multicrystalline silicon solar cells. Semiconductors, 41(4), pp.440-443.

[20] Alonso-García, M., Ruiz, J. and Chenlo, F. (2006). Experimental study of mismatch and shading effects in the – characteristic of a photovoltaic module. Solar Energy Materials and Solar Cells, 90(3), pp.329-340.

[21] Breitenstein, O., Bauer, J., Bothe, K., Kwapil, W., Lausch, D., Rau, U., Schmidt, J., Schneemann, M., Schubert, M., Wagner, J. and Warta, W. (2011). Understanding junction breakdown in multicrystalline solar cells. J. of Appl. Phys., 109(7), p.071101.

[22] Lausch, D., Petter, K., Bakowskie, R., Czekalla, C., Lenzner, J., von Wenckstern, H. and Grundmann, M. (2010). Identification of pre-breakdown mechanism of silicon solar cells at low reverse voltages. Appl. Phys. Letters, 97(7), p.073506.

[23] Breitenstein, O. (2017). Your article in Physica B. [email].

[24] Gundel, P., Kwapil, W., Schubert, M., Seifert, H. and Warta, W. (2010). Approach to the physical origin of breakdown in silicon solar cells by optical spectroscopy. Journal of Applied Physics, 108(12).

[25] Breitenstein, O. (2013). Understanding the current-voltage characteristics of industrial crystalline silicon solar cells by considering inhomogeneous current distributions. Opto-Electronics Review, 21(3).

[26] Bothe, K., Ramspeck, K., Hinken, D., Schinke, C., Schmidt, J., Herlufsen, S., Brendel, R., Bauer, J., Wagner, J., Zakharov, N. and Breitenstein, O. (2009). Luminescence emission from forward- and reverse-biased multicrystalline silicon solar cells. Journal of Applied Physics, 106(10), 104510.

[27] Breitenstein, O., Bauer, J., Lotnyk, A. and Wagner, J. (2009). Defect induced non-ideal dark – characteristics of solar cells. Superlattices and Microstructures, 45(4-5), pp.182-189.

[28] Bauer, J., Lausch, D., Blumtritt, H., Zakharov, N. and Breitenstein, O. (2012). Avalanche breakdown in multicrystalline solar cells due to preferred phosphorous diffusion at extended defects. Progress in Photovoltaics: Research and Applications, 21(7), pp.1444-1453.

[29] Crozier, J.L., van Dyk, E.E., Vorster, F.J.V. Identifying Voltage Dependant Features In Photovoltaic Modules Using Electroluminescence Imaging. In EU PVSEC. Netherlands, Amsterdam, 22 - 26 September 2014. p3288-3291.

[30] Hinken, D., Ramspeck, K., Bothe, K., Fischer, B. and Brendel, R. (2007). Series resistance imaging of solar cells by voltage dependent electroluminescence. Applied Physics Letters, 91(18), p.182104.

[31] Fuyuki, T., Kitiyanan, A. (2009). Photographic diagnosis of crystalline silicon solar cells utilizing Electroluminescence, Applied Physics A. 963, 189-196

[32] Fuyuki, T., Kondo, H., Kaji, Y., Ogane, A., and Takahashi, Y. (2007). Analytic findings in the electroluminescence characterization of crystalline silicon solar cells, Journal of Applied Physics 101, 023711

[33] Kőntges, M., Kunze, I., Kajari-Schrőder, S., Breitenmoser, X., Bjørneklett, B. (2011). The risk of power loss in crystalline silicon based photovoltaic modules due to micro-cracks, Solar Energy Materials & Solar Cells 95 1131–113

[34] Burden, R. 2000. Numerical Analysis. 7 Edition. Brooks Cole.

[35] Serway, R. (2007). Physics for scientists and engineers. Pacific Grove: Brooks/Cole. Orlov, V. and Yakimov, E. (2016). Extended defect study in Si: EBIC versus LBIC. Superlattices and Microstructures, 99, pp.202-207.

[36] Jervase, J., Bourdoucen, H. and Al-Lawati, A. (2001). Solar cell parameter extraction using genetic algorithms. Measurement Science and Technology, 12(11), pp.1922-1925.

[37] Engelbrecht, A. (2008). Computational intelligence: An introduction. Boca Raton, Florida: CRC Press.

[38] Ming Leung, K. (2003). GENETIC ALGORITHMS. [online] Available at: http://cis.poly.edu/~mleung/CS4744/f04/ch06/GA3.pdf [Accessed 24 Jun. 2017].

[39] Baluja, S. and Caruana, R. (1995). Removing the genetics from the standard genetic algorithm. In Machine Learning: Proceedings of the Twelfth International Conference (pp. 38-46).

[40] Črepinšek, M., Liu, S. and Mernik, M. (2013). Exploration and exploitation in evolutionary algorithms. ACM Computing Surveys, 45(3), pp.1-33.

[41] Vafaee, F., Turan, G., Nelson, P. and Berger-Wolf, T. (2014). Balancing the Exploration and Exploitation in an Adaptive Diversity Guided Genetic Algorithm. In: 2014 IEEE Congress on Evolutionary Computation (CEC). [online] IEEE, pp.2570-2577.

[42] Product Overview. [pdf] Radolfzell: Sensovation. Available at: http://www.sensovation.com/bausteine.net/f/10339/web_SensoCamA4single.pdf?fd=2 [Accessed 28 Jul. 2017].

[43] Zeiss.com. ZEISS Distagon T* 2.8/25 |. [online] Available at: https://www.zeiss.com/camera-lenses/us/photography/products/classic-lenses/distagon-2825.html [Accessed 28 Jul. 2017].

[44] Coating Curve. (2009). [pdf] Available at: https://www.edmundoptics.com/optics/optical-filters/longpass-edge-filters/850nm-25mm-dia.-high-performance-longpass-filter/#specs [Accessed 28 Jul. 2017].

[45] Optris.com. (2017). optris PI 640 The smallest measuring VGA thermal imager worldwide. [online] Available at: http://www.optris.com/thermal-imager-optris-pi-640 [Accessed 2 Aug. 2017].

[46] 2450 SourceMeter® SMU Instrument Datasheet. [pdf] Available at: http://www.tek.com/sites/tek.com/files/media/media/resources/2450-Datasheet_1KW-60904-0.pdf [Accessed 2 Aug. 2017].

[47] Cube Laser Diode System. [pdf]. Available at: https://cohrcdn.azureedge.net/assets/pdf/COHR_CUBE_DS_0316_3.pdf [Accessed 2 Aug. 2017].

[48] Thorlabs. GVS002 - 2D Galvo System. [pdf], Silver-Coated Mirrors. [online] Available at: https://www.thorlabs.com/thorproduct.cfm?partnumber=GVS002 [Accessed 4 Aug. 2017].

[49] Thorlabs.com. F-Theta Scan Lenses. [online] Available at: https://www.thorlabs.com/newgrouppage9.cfm?objectgroup_id=6430 [Accessed 4 Aug. 2017].

[50] Compact USB Power Meter with Silicon Photodiode Detector. (2015). [pdf] Available at: https://www.thorlabs.com/newgrouppage9.cfm?objectgroup_id=9005 [Accessed 4 Sep. 2017].

[51] Device Specifications NI 6356. (n.d.). [pdf] Available at: http://www.ni.com/pdf/manuals/374452c.pdf [Accessed 4 Aug. 2017].

[52] Low-Noise Current Preamplifier, SR570 — DC to 1 MHz current preamplifier. (n.d.). [pdf] Available at: http://www.thinksrs.com/downloads/PDFs/Catalog/SR570c.pdf [Accessed 4 Aug. 2017]

[53] Summhammer, J. and Halavani, Z. (2016). Cell interconnection without glueing or soldering for crystalline Si photovoltaic modules. EPJ Photovoltaics, 7, p.75401.